

2008

Quadrupole Magnetic Field-Flow Fractionation; a Novel Technique for the Characterization of Magnetic Particles

Francesca Carpino
Cleveland State University

Follow this and additional works at: <https://engagedscholarship.csuohio.edu/etdarchive>

 Part of the [Chemistry Commons](#)

How does access to this work benefit you? Let us know!

Recommended Citation

Carpino, Francesca, "Quadrupole Magnetic Field-Flow Fractionation; a Novel Technique for the Characterization of Magnetic Particles" (2008). *ETD Archive*. 51.

<https://engagedscholarship.csuohio.edu/etdarchive/51>

This Dissertation is brought to you for free and open access by EngagedScholarship@CSU. It has been accepted for inclusion in ETD Archive by an authorized administrator of EngagedScholarship@CSU. For more information, please contact library.es@csuohio.edu.

QUADRUPOLE MAGNETIC FIELD-FLOW FRACTIONATION: A NOVEL
TECHNIQUE FOR THE CHARACTERIZATION OF MAGNETIC PARTICLES

FRANCESCA CARPINO

'Laurea' degree in Chemistry
Università degli Studi di Bologna, Italy

June, 2002

submitted in partial fulfillment of requirements for the degree
DOCTOR OF PHILOSOPHY IN CLINICAL AND BIOANALYTICAL CHEMISTRY

at the
CLEVELAND STATE UNIVERSITY

March, 2008

This dissertation has been approved for
the Department of CHEMISTRY and
the College of Graduate Studies by

Dissertation Committee Chairperson, Dr. P. Stephen Williams
Department of Biomedical Engineering, Cleveland Clinic

Committee Member, Dr. Aaron Fleischman
Department of Biomedical Engineering, Cleveland Clinic

Committee Member, Dr. John F. Turner
Department of Chemistry, Cleveland State University

Committee Member, Dr. Yan Xu
Department of Chemistry, Cleveland State University

Committee Member, Dr. Maciej Zborowski
Department of Biomedical Engineering, Cleveland Clinic

ACKNOWLEDGEMENTS

Many people have contributed in different ways to this thesis work. I am deeply grateful to all of them.

In particular I would like to thank my supervisors: Dr. P. Stephen Williams, for his patience and support, a tutor always present in moments of need and an erudite guide throughout the entire course of this research study, and Dr. Maciej Zborowski, for his support, knowledge, and for giving me the opportunity to work in his lab.

Many thanks to Lee Moore for his helpful and his excellent work on designing the quadrupole electromagnet.

My gratitude goes also to Dr. Pierluigi Reschiglian who ultimately was responsible for my decision to embark on a Ph.D. in the United States.

I would like to thank Dr. Jurg Roher, Dr. Arfaan Rampersaud, Kristie Melnik, and Professor Shlomo Margel for kindly supplying the samples of magnetic nanoparticles, and Dr. Graciela Oстера for supplying the blood samples.

Thanks to Anna Dubnisheva and Weiwei Hu for the SEM and DLS analysis of the magnetic nanoparticles.

Thanks to James Proudfit for his machining expertise of both the electromagnet components and the helical channel, and to Steffen Steinert for his preliminary measurements of the quadrupole electromagnet.

Finally, thanks go to my parents for their love and support, to my brothers and my dearest friends always present to support me and cheer me up: Giananadrea, Giulio, Maddalena, Ignazio & Rossana, Leonardo, Cristiana & Nicola, Carmel, Deborah, Maria Carla, Stefania, Alessandro, Enzo, and Laura.

QUADRUPOLE MAGNETIC FIELD-FLOW FRACTIONATION: A NOVEL
TECHNIQUE FOR THE CHARACTERIZATION OF MAGNETIC PARTICLES

FRANCESCA CARPINO

ABSTRACT

In the last few decades, the development and use of nanotechnology has become of increasing importance. Magnetic nanoparticles, because of their unique properties, have been employed in many different areas of application. They are generally made of a core of magnetic material coated with some other material to stabilize them and to help disperse them in suspension. The unique feature of magnetic nanoparticles is their response to a magnetic field. They are generally superparamagnetic, in which case they become magnetized only in a magnetic field and lose their magnetization when the field is removed. It is this feature that makes them so useful for drug targeting, hyperthermia and bioseparation. For many of these applications, the synthesis of uniformly sized magnetic nanoparticles is of key importance because their magnetic properties depend strongly on their dimensions. Because of the difficulty of synthesizing monodisperse particulate materials, a technique capable of characterizing the magnetic properties of polydisperse samples is of great importance.

Quadrupole magnetic field-flow fractionation (MgFFF) is a technique capable of fractionating magnetic particles based on their content of magnetite or other magnetic material. In MgFFF, the interplay of hydrodynamic and magnetic forces separates the particles as they are carried along a separation channel. Since the magnetic field and the

gradient in magnetic field acting on the particles during their migration are known, it is possible to calculate the quantity of magnetic material in the particles according to their time of emergence at the channel outlet. Knowing the magnetic properties of the core material, MgFFF can be used to determine both the size distribution and the mean size of the magnetic cores of polydisperse samples. When magnetic material is distributed throughout the volume of the particles, the derived data corresponds to a distribution in equivalent spherical diameters of magnetic material in the particles. MgFFF is unique in its ability to characterize the distribution in magnetic properties of a particulate sample. This knowledge is not only of importance to the optimization and quality control of particle preparation. It is also of great importance in modeling magnetic cell separation, drug targeting, hyperthermia, and other areas of application.

TABLE OF CONTENTS

ACKNOWLEDGEMENTS.....	iii
ABSTRACT.....	iv
LIST OF TABLES.....	x
LIST OF FIGURES.....	xi
CHAPTER	
I. INTRODUCTION TO FIELD-FLOW FRACTIONATION (FFF).....	1
1.1 Field-Flow Fractionation Techniques.....	1
1.2 Mechanism of FFF.....	4
1.2.1 Retention parameter.....	7
1.2.2 Selectivity and resolution.....	10
1.2.3 Advantages of FFF.....	11
II. MAGNETISM AND MAGNETIC MATERIALS.....	12
2.1 The magnetic field.....	12
2.2 Basic magnetic quantities.....	12
2.2.1 The magnetic induction.....	12
2.2.2 The magnetic dipole.....	15
2.2.3 Magnetization.....	16
2.2.4 Relation between H, M, and B.....	17
2.3 Classification of materials by magnetic properties.....	17
2.4 Bulk magnetic properties and their measurement.....	21
2.4.1 Magnetic anisotropy.....	21
2.4.2 Hysteresis.....	22

2.4.3	Hysteresis effects on the magnetization.....	24
2.5	Magnetic particles and their applications.....	25
2.5.1	Particle magnetism.....	26
2.5.2	Superparamagnetism.....	27
2.5.3	Biomedical applications of magnetic nanoparticles.....	28
2.5.4	Characterization techniques for particles.....	29
III.	QUADRUPOLE MAGNETIC FIELD-FLOW FRACTIONATION.....	31
3.1	Introduction to MgFFF.....	31
3.1.1	Theory of MgFFF.....	32
3.1.2	Interaction of particles with fields.....	35
3.1.3	Magnetic force on particles.....	35
3.1.4	Magnetophoretic mobility.....	39
3.2	Cell Tracking Velocimetry (CTV).....	40
3.3	Earlier implementations of magnetic FFF.....	41
IV.	DEVELOPMENT OF THE SYSTEM.....	46
4.1	Description of the system.....	46
4.1.1	The quadrupole field.....	46
4.1.2	The helical channel.....	50
4.2	Assembly of the quadrupole electromagnet and evaluation of its magnetic field.....	52
4.2.1	Temperature effects.....	53
4.2.2	Experimental Procedure.....	55
4.2.3	Materials and Methods.....	58

4.2.3.1	Coil design.....	60
4.2.3.2	Hall-effect probe principle of operation.....	62
4.2.4	Results.....	64
4.2.5	Adjustment of electrical coil resistance.....	65
4.2.6	Simultaneous demagnetization of the four coils.....	67
4.2.7	Determination of the working reference curve for a single coil.....	68
4.2.8	Coil heating.....	69
4.2.9	Error analysis.....	70
4.3	New method for the determination of minor hysteresis curves....	72
4.4	MgFFF Instrumentation set-up.....	77
4.5	Mobile phase properties and preparation.....	78
4.6	Sample preparation.....	79
4.7	Experimental procedure.....	79
V. PRELIMINARY STUDIES.....		83
5.1	Steric/hyperlayer fractionation of polystyrene/magnetite microspheres by MgFFF.....	83
5.2	Magnetic Field-Flow Fractionation of erythrocytes.....	88
5.2.1	Method of operation.....	91
VI. DEVELOPMENT OF PROGRAMMED FIELD.....		89
6.1	Introduction.....	95
6.2	Power programmed field decay.....	96
6.3	Data analysis for the determination of size distributions.....	98

6.4	Required settings for the field-decay during MgFFF experiments.....	99
VII.	RESULTS AND CONCLUSIONS.....	101
7.1	Magnetic Field-Flow Fractionation of dextran coated magnetite nanoparticles.....	101
7.2	MgFFF analysis of maghemite nanoparticles.....	113
7.3	MgFFF analysis of CNW nanoparticles.....	114
7.4	Comparison of the three samples.....	116
7.5	Importance of the coating in the magnetic nanoparticles.....	117
7.6	Conclusions.....	120
	REFERENCES.....	121

LIST OF TABLES

Table	Page
I. Force and retention parameter equations for different forms of FFF. (G = centrifugal acceleration; V_c = volumetric rate of crossflow; D_T =thermal diffusion coefficient; d_s = diameter of the particle; η = fluid viscosity; μ = electrophoretic mobility; E = electric field).....	10
II. Unit systems used in magnetism and relationships between some parameters.....	14
III. Classification of materials based on their magnetic behavior.....	20
IV. Equation parameters for different ranges of current.....	76

LIST OF FIGURES

Figure 1.1	Schematic diagram of the field-flow fractionation (FFF) channel. A and B are the analyte components.....	2
Figure 1.2	Fields of application of the FFF techniques. In the x axis is shown the logarithmic scale of molecular weights.....	4
Figure 1.3	The MgFFF retention mechanism is different for nanoparticles and microparticles. a) Shows a schematic of the channel section where nanoparticles are subject to diffusion and elute according to the normal mode mechanism. b) Shows a schematic of the channel section where microparticles elute in the steric/hyperlayer mode because the diffusivity is negligible.....	7
Figure 2.1	Magnetic field generated by a long conductor carrying electric current.....	13
Figure 2.2	A bar magnet in an external field B experiences a torque tending to align it parallel to the field direction.....	16
Figure 2.3	Crystal structure of single crystal of iron. The crystal structure can be magnetized easily in the [100] direction, but has a hard direction of magnetization in the [111] direction.....	22
Figure 2.4	Typical hysteresis loop for a ferromagnetic material.....	23
Figure 3.1	MgFFF instrumentation setup.....	32
Figure 3.2	Schematic of a section of the channel thickness illustrating the retention mechanism.....	33
Figure 4.1	The quadrupole magnetic field. The helical channel occupies a thin annular space between the inner and outer radii, r_i and r_o , respectively. The thickness of the annulus is exaggerated in the figure for clarity.....	47
Figure 4.2	Top view of a cross section of the quadrupole magnet B1. It has been employed for the analysis of red blood cells. It generates a magnetic field of 1.42T at the radial distance of the pole tips.....	49
Figure 4.3	Top view of a cross section of the quadrupole magnet B2. It has been employed for the analysis of magnetic microspheres. It generates a magnetic field of 0.071T at the pole tips.....	49
Figure 4.4	The helical channel geometry machined into the surface of the polymer cylinder. The original surface of the cylinder is shown in gray with the	

machined area white in order to highlight the spiral path of the channel. The inlet and outlet ports are shown as small circles at the ends of the channel...52

Figure 4.5	Longitudinal section of the 250 μm thick helical channel inserted into the stainless steel cylinder. The inlet and outlet ports are shown as small circles at the ends of the channel.....	52
Figure 4.6	Hysteresis curve showing dependence of the field strength B on the applied current I	56
Figure 4.7	Schematic of the demagnetization procedure (from point b to point e) and the minor hysteresis curves for different values of maximum current. The curves lead to different values of remnant fields (points I, II, III, and IV in the diagram).....	58
Figure 4.8	Schematic of the quadrupole electromagnet cross section. The low-carbon steel pole pieces and yoke are shown in pale gray, and the copper coils in darker gray. The stainless steel tube that encloses the MgFFF helical channel fits snugly between the four pole tips at the aperture, with a nominal tolerance of 0.005”.....	60
Figure 4.9	Assembled electromagnet.....	60
Figure 4.10	Simulated magnetic field density vectors of the quadrupole electromagnet and polarization of the coils (provided by Lee R. Moore)...	62
Figure 4.11	Schematic of Hall-effect probe at the surface of a pole tip.....	64
Figure 4.12	Required demagnetization currents for different maximum magnetization currents in one coil.....	65
Figure 4.13	Magnetization of coils with 4 individual demagnetisation currents.....	66
Figure 4.14	Magnetization curves with individual I_{demag} after correcting resistance of coil 1.....	67
Figure 4.15	Mean field intensity for the four pole pieces and standard deviation for the 2 magnetization steps.....	69
Figure 4.16	Deviation from the mean B for 4 coils for decreasing B from 0.71T to 0T.....	71
Figure 4.17	Improved method for producing predictable B versus I profile.....	73
Figure 4.18	Average values for the four coils of B versus I for the range of current (5.0-0.0) A. The points were interpolated using equation (4.25).....	74

Figure 4.19	Hysteresis loop. The minor hysteresis curve used for the experiments starting at 0.25 A is shown in red color. The corresponding value of magnetic field is ~56 mT and the remnant field value is ~ 3.0 mT.....	75
Figure 4.20	Relationship between the field measured at pole tip 2 and the field measured between poles 2-3.....	77
Figure 4.21	Schematic of the MgFFF system during the sample loading and elution operating mode. The carrier fluid goes from the pump through the separation channel and to the detector via the diagonal switching valve....	82
Figure 4.22	Schematic of the MgFFF system during the stop-flow operating mode. The carrier fluid is directed from the pump to the waste via the diagonal switching valve. In this case the flow into the system is stopped and the sample injected into the channel is allowed to relax.....	82
Figure 5.1	Size distribution data of bare polystyrene microspheres obtained using Coulter Multisizer Z-2.....	84
Figure 5.2	SEM images of a) bare monodisperse polystyrene (PS) microspheres; b) PS microspheres with magnetite coating; c) PS microspheres with magnetite and silica coating. The final diameter of the microspheres is $2.7 \pm 0.04 \mu\text{m}$	85
Figure 5.3	Composite magnetophoretic mobility histogram of the three size-monodisperse magnetic microspheres (MMC4, MMC3, MMC2) measured by Cell Tracking Velocimetry (CTV).....	87
Figure 5.4	MgFFF elution profile of a mixture of three samples of magnetic microspheres (MMC4, MMC3, MMC2) having different magnetophoretic mobility. The fractionation is obtained by applying an increase in carrier flow rate with time (from 0.9 ml/min to 10 ml/min) at a constant magnetic field strength of 0.071 Tesla.....	88
Figure 5.5	Magnetophoretic mobility histograms of oxygenated and methemoglobinated RBCs. Note the higher mobility values for the methemoglobin-rich RBCs compared to the oxygenated RBCs.....	94
Figure 5.6	Steric/hyperlayer mode of elution of erythrocytes by MgFFF. The first peak in each fractogram corresponds to the void time (defined as the time that non-retained species spend in the system); the second peak corresponds to the eluted cell sample. Sample volume: 20 μl ; sample concentration $<10^6$ cells/20 μl ; elution flow rate 2.0 ml/min; stop flow time: 50 min in A and 20 min in B. A. Oxygenated erythrocytes. B. Methemoglobin-rich erythrocytes.	

	Note the shift to longer retention time of the eluted sample peak 2 in B relative to A, indicating retention of the methemoglobin-rich erythrocytes in the magnetic field.....	94
Figure 6.1	Field-decay curve for power programming.....	97
Figure 6.2	Calculated current decays over time relative to different program parameters.....	100
Figure 6.3	Theoretical values of field decays obtained using the same initial current of 5 A held constant for 8 minutes. Note how the shape of the decays over time changes with the changing of the program parameters t_1 , t_a , and p	100
Figure 7.1	SEM images of nanoparticles from lot 80. a) Image of a cluster of nanoparticles. They probably aggregated during drying for SEM sample preparation. b) Image of a single nanoparticle of about 200 nm diameter. Courtesy of Anna Dubnisheva, Dept. of Biomedical Engineering, Cleveland Clinic.....	102
Figure 7.2	Size distribution data of dextran coated magnetite nanoparticles (lot80) obtained by quasi-elastic light scattering analysis. Measurements carried out by Weiwei Hu of the Department of Chemical and Biomolecular Engineering at Ohio State University.....	103
Figure 7.3	MgFFF elution profiles of sample 80 obtained at constant field strengths: a) 53 mT, b) 40 mT, c) 20 mT, d) 7 mT. In each case, the field strength falls to zero when the channel is removed from the magnet.....	104
Figure 7.4	Superimposed fractograms (detector response as a function of elution time) obtained for lots 40–43 and 80 of Skold magnetic nanoparticles. Lot 80 is less retained than lot 40–43 and the particles therefore contain less magnetite. The dashed curve shows the programmed field decay at the channel accumulation wall (right hand axis). The field strength is held constant at 56.5 mT for 2 min, and decays to 3.3 mT over a period of 7 min. Fluid flow rate was 2.0 ml/min for both samples.....	106
Figure 7.5	MgFFF elution curves for various lots of Skold Technology magnetic nanoparticles obtained under identical conditions. a) two elution curves for lot 80, b) elution curves for lots 80 and 78, c) elution curves for lots 80 and 50-56, d) elution curves for lots 80 and 83.....	107
Figure 7.6	Elution profile for sample of Skold nanoparticles (lot 80) and the field decay curve (referring to the right hand axis).....	108

Figure 7.7	Magnetization curve showing the data for superparamagnetic magnetite nanoparticles. The points were digitized from a published plot [115], and fitted to the empirical equation 7.1.....	109
Figure 7.8	Number distribution for calculated equivalent spherical core diameters. A number of different decay programs were evaluated for best sample fractionation.....	110
Figure 7.9	a) Elution profiles of dextran coated magnetite nanoparticles, lot 80, under different experimental conditions. b) Reproducible determination of distribution in particle magnetite content (equivalent spherical diameter of magnetite core) for elution under the different experimental conditions. Note that although the shape of the elution profile depends on the experimental conditions (such as initial field strength, field decay rate, elution flow rate) the calculate size of the magnetic cores is quite consistent. The differences in the region over 0.5 μm are attributable to baseline drift (no corrections were applied).....	112
Figure 7.10	Elution profile for sample of maghemite nanoparticles and the field decay curve (referring to the right hand axis).....	113
Figure 7.11	Number distribution for calculated equivalent spherical core diameter of the maghemite nanoparticles.....	114
Figure 7.12	Size distribution data of dextran coated magnetite nanoparticles (provided by CNW) obtained by dynamic light scattering analysis. Measurements carried out by Malvern Instruments.....	115
Figure 7.13	Elution profile of sample 628DH_Aq (Fe-hexanoic acid nanoparticles coated with dextran). The magnetic field decay profile is shown by the red line.....	116
Figure 7.14	Size distribution profile of sample 628DH_Aq (Fe-hexanoic acid nanoparticles coated with dextran).....	116
Figure 7.15	Size distribution profiles of sample CNW (Fe-hexanoic acid nanoparticles coated with dextran), blue line; sample MM (dextran coated maghemite nanoparticles), red line; and iron oxide dextran-coated nanoparticles from Skold technologies (BD Biosciences, Pharmingen), green line.....	117
Figure 7.16	Elution profiles for sample BD-CCF-8 (dextran coated magnetic nanoparticles) and sample BD-CCF-9 (bare core material). The experimental conditions (elution flow rate and field decay program) are the same for both analyses. The magnetic field decay profile is shown by the red line.....	119

CHAPTER I

INTRODUCTION TO FIELD-FLOW FRACTIONATION (FFF)

1.1 Field-Flow Fractionation Techniques

The field-flow fractionation (FFF) techniques are analytical scale separation and characterization methods for macromolecules and particles (ranging from 0.01 to 100 μm in diameter). They are extremely versatile and have been utilized for biopolymers, emulsions, many types of colloids, charged particles, and other types of particles from a wide variety of sources. Analytes may be in either organic or aqueous suspensions. The separation mechanism was conceived by J. C. Giddings in 1966 [1]. They are elution techniques similar to chromatography in which components of a sample mixture elute from the system at different times. Whereas chromatography exploits differences in partition between the mobile and stationary phases to separate sample components as they are carried along a column, FFF separation is achieved within the mobile phase alone. Retention in FFF is obtained by the combined action of the flow of mobile phase inside a thin open channel and an external field acting perpendicularly to the flow. The observed retention time t_r is related to various physicochemical properties of the retained

species such as mass, size, density, charge, or diffusivity. The measurement of t_r values can therefore yield these properties for each fractionated component. As in chromatography, a detector may be placed at the channel outlet to register the elution of the sample components from the channel at different times. If this characterization is not sufficient, fractions can be collected and further examined by microscopy, light scattering, elemental analysis, and subsequent FFF analyses.

Channel structure and geometry is critical to FFF performance. The shape of the cross section determines the flow profile and often the field direction, separation speed, and sample capacity. Most channels used for FFF are thin ribbonlike structures. This configuration is showed in Figure 1.1.

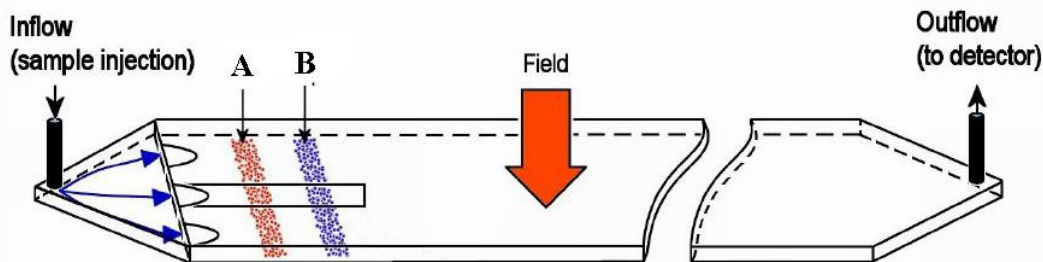


Figure 1.1. Schematic diagram of the field-flow fractionation (FFF) channel. A and B are the analyte components.

The nature of the applied field determines the sample property that is characterized. This leads to different techniques and sub-techniques such as gravitational FFF (GrFFF), sedimentation FFF (SdFFF), flow FFF (FIFFF), thermal FFF (ThFFF), electrical FFF (EIFFF), and magnetic FFF (MgFFF). In GrFFF and SdFFF the gravitational and centrifugal fields retain particles in the channel according to their buoyant mass, $V_p\Delta\rho$, where V_p is the particle volume and $\Delta\rho$ is the density difference

between the particles and the carrier fluid. In FIFFF the field is provided by a second independent flowstream (called the crossflow stream) that permeates through the channel walls and across the channel at right angles to the primary channel flow stream. The diffusivity of the suspended particle or solute is the separating factor. In ThFFF a temperature gradient is established between two parallel conductive metal bars, and species are separated based on the principle of thermal diffusion. In EIFFF the electrical field separates particles according to their electrical charge. In MgFFF the magnetic field separates magnetic particles based on their content of magnetite or other magnetic material. Field-flow fractionation has developed into this versatile family of techniques that exploits a variety of field types to characterize different particle properties [2]. In Figure 1.2 is shown an overview of some of the applications of the FFF techniques.

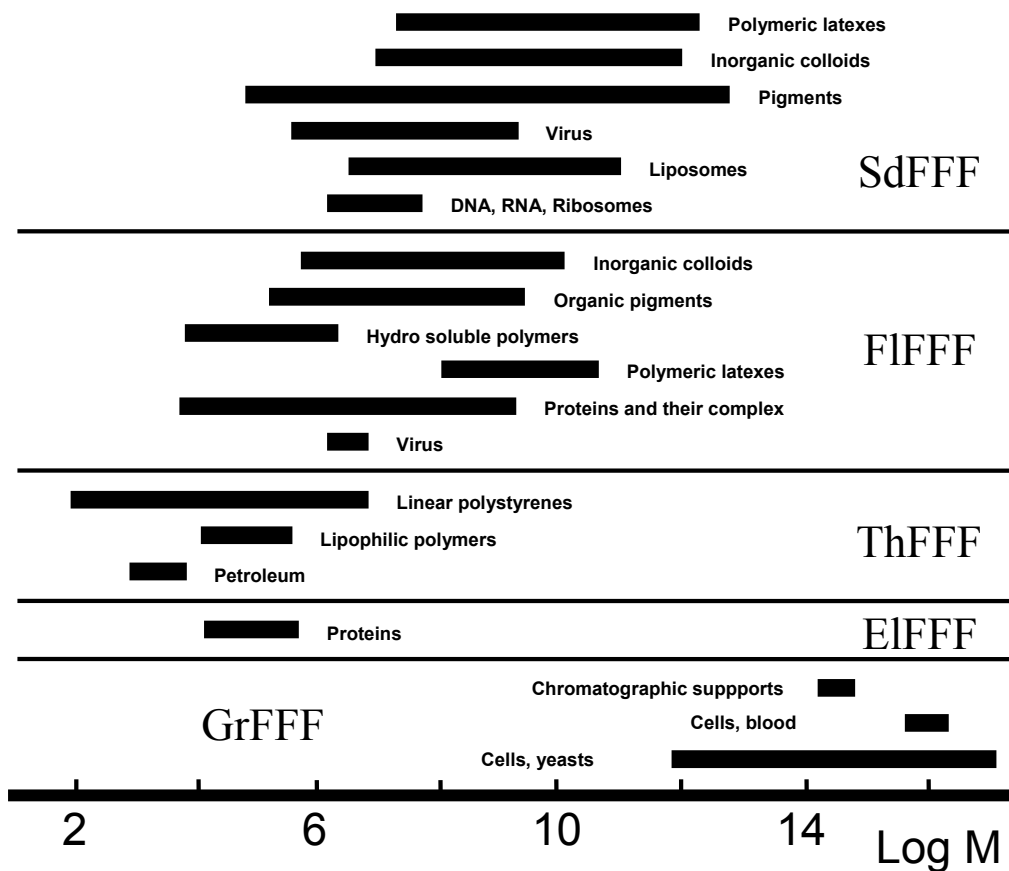


Figure. 1.2. Fields of application of the FFF techniques. In the x axis is shown the logarithmic scale of molecular weights [3].

1.2 Mechanism of FFF

The FFF mechanism is illustrated in Figure 1.3. The separation device takes the form of a thin (50- to 500- μm) parallel-walled channel across the thickness of which a field or field gradient is applied. Due to viscous drag the mobile phase velocity profile inside the channel is parabolic, or near-parabolic, with highest fluid velocity close to the channel center and zero velocity at the walls. The field or field gradient acts to drive susceptible sample components into equilibrium distributions close to one wall, the so-called accumulation wall, and, therefore, into relatively slowly moving fluid streamlines.

In FFF several specific separation mechanisms arise depending on factors controlling particle distributions. There are two principal modes of operation for FFF: the so-called normal mode and the steric mode. Most polymers and submicrometer particles are separated by the mechanism known as the normal mode. In this mode the applied field drives the particles in the FFF channel toward the accumulation wall, and the concentration gradient set up by this field-driven motion is opposed by diffusion. When these two processes balance, particle concentration approaches an exponential function of elevation x above the accumulation wall:

$$c = c_0 \exp(-x/\ell) \quad (1.1)$$

where ℓ is the mean elevation of the particle population in the channel. Separation between two populations of particles occurs if their values of ℓ differ. The ℓ for each component is equal to

$$\ell = D/|U| \quad (1.2)$$

Where D is the diffusion coefficient and U is the field induced velocity toward the accumulation wall. ℓ depends also on the force F exerted by the field on a single particle:

$$\ell = kT/|F| \quad (1.3)$$

where k is the Boltzmann's constant and T is the absolute temperature. The retention time is equal to the ratio between the channel length L and the velocity v of a specific population of particles. Thus,

$$t_r = L/v \quad (1.4)$$

and, it has been shown [4] that

$$\frac{t_r}{t^0} = \frac{w}{6\ell} \left[\coth \frac{w}{2\ell} - \frac{2\ell}{w} \right]^{-1} \quad (1.5)$$

where t^0 is the void time (the elution time of non retained material) and w is the channel thickness. When ℓ is written in terms of F , then:

$$\frac{t_r}{t^0} = \frac{|F|w}{6kT} \left(\coth \frac{|F|w}{2kT} - \frac{2kT}{|F|w} \right)^{-1} \quad (1.6)$$

When $w \gg \ell$, $\frac{t_r}{t^0}$ is approximated by:

$$\frac{t_r}{t^0} = \frac{w}{6\ell} = \frac{|F|w}{6kT} \quad (1.7)$$

The magnitude of F depends on particle properties, field strength, and type of field. It usually increases with particle diameter d (or molecular weight M).

The steric/hyperlayer mode applies to larger particles (~ 0.5 - $200 \mu\text{m}$).

Hydrodynamic lift forces tend to push components away from the accumulation wall [5], and these forces increase with fluid flow rate. At the same time, the field acts on the particles pushing them toward the accumulation wall, focusing them into a thin so-called hyperlayer. Because hydrodynamic forces increase strongly with particle size (to the power of 3 to 4), larger particles tend to be focused at higher velocity streamlines and elute earlier than smaller particles.

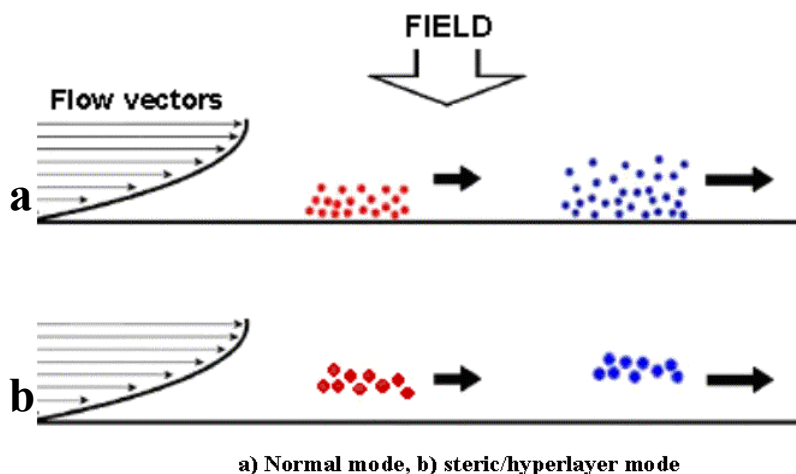


Figure 1.3. The MgFFF retention mechanism is different for nanoparticles and microparticles. a) Shows a schematic of the channel section where nanoparticles are subject to diffusion and elute according to the normal mode mechanism. b) Shows a schematic of the channel section where microparticles elute in the steric/hyperlayer mode because the diffusivity is negligible.

For the analysis of a sample it is common practice to stop the fluid flow immediately after sample introduction to the channel to allow the sample components to approach their steady state distributions next to the accumulation wall. The flow is then resumed to carry out the separation.

1.2.1 Retention parameter

Retention in FFF can be described by the dimensionless parameter λ . The force F exerted on a sample by the external field is related to λ by

$$\lambda = \frac{kT}{|F|w} = \frac{\ell}{w} \quad (1.8)$$

λ is therefore equal to the ratio of thermal energy kT to the energy required to drive a particle across the channel thickness against the applied field $|F|w$. λ is always positive and indicates the degree of zone compression. The larger the force on the analyte, the

more compressed will be the zone at the accumulation wall. The retention parameter defines the distance between the accumulation wall and the center of gravity of the analyte zone relative to the channel thickness. It is related to characteristics of the sample that define its interaction with the force field, and it is related to the experimentally measured retention ratio R , which can be expressed as

$$R = \frac{t^0}{t_r} \quad (1.9)$$

where t^0 and t_r are the retention times associated with the peak maxima of unretained and retained peaks, respectively. The retention ratio is the factor that describes the retardation of an analyte relative to the mean fluid velocity caused by its compression by the field. R usually has values between 0 and 1, but in the steric/hyperlayer mode of operation R can be as large as 1.5 if particles are driven to the center of the channel.

The velocity profile of the fluid flow inside a channel of rectangular cross section of high aspect ratio can be expressed by the parabolic equation

$$v(x) = 6\langle v \rangle \frac{x}{w} \left(1 - \frac{x}{w} \right) \quad (1.10)$$

where $v(x)$ is the linear velocity of the flow at distance x from the accumulation wall and $\langle v \rangle$ is the average flow velocity. The average velocity of the analyte zone is defined by the distribution of analyte across the velocity profile of the carrier liquid:

$$v_{zone} = \frac{\int_0^w c(x)v(x)dx}{\int_0^w c(x)dx} \quad (1.11)$$

The retention ratio can also be expressed as

$$R = \frac{v_{zone}}{\langle v \rangle} \quad (1.12)$$

By substitution of equation (1.10) and (1.11) in equation (1.12) and combining with equation (1.1), we obtain:

$$R = 6\lambda \left[\coth \frac{1}{2\lambda} - 2\lambda \right] \quad (1.13)$$

which is equivalent to equations (1.5) and (1.6).

This is the general expression for normal mode retention in the FFF techniques. We notice a direct relationship between R and the retention parameter λ that is directly related to the physicochemical properties of the analytes.

Equation 1.13 may be approximated for small λ by the equations

$$R = 6\lambda - 12\lambda^2 \quad (1.14)$$

and

$$R = 6\lambda \quad (1.15)$$

Equation (1.14) is accurate to within 2% when $\lambda < 0.2$; equation (1.15) is accurate to within 5% when $\lambda < 0.02$.

Narrow size distribution standard polystyrene latex beads have been repeatedly analyzed by various FFF subtechniques to examine the performance of FFF instruments or to verify theoretical principles. Table I shows the equations for the retention parameter (λ) and field-induced force (F) for each of the principal FFF sub-techniques.

Table I. Force and retention parameter equations for different forms of FFF. (G= centrifugal acceleration; V_c = volumetric rate of crossflow; D_T =thermal diffusion coefficient; d_s = diameter of the particle; η = fluid viscosity; μ = electrophoretic mobility; E= electric field).

FFF subtechnique	Field-induced force (F)	Retention parameter (λ)
Sedimentation	$F_S = \frac{1}{6} \pi d_s^3 \Delta \rho G$	$\lambda_S = \frac{6kT}{\pi \Delta \rho G w d_s^3}$
Flow	$F_F = \frac{3\pi \eta d_s V_C w}{V^0}$	$\lambda_F = \frac{kTV^0}{3\pi \eta d_s w^2 V_C}$
Thermal	$F_T = \frac{3\pi \eta d_s D_T \Delta T}{w}$	$\lambda_T = \frac{kT}{3\pi \eta d_s D_T \Delta T}$
Electrical	$F_E = 3\pi \eta d_s \mu E$	$\lambda_E = \frac{kT}{3\pi \eta d_s \mu E w}$

1.2.2 Selectivity and resolution

Selectivity is the measure of the capability of a technique to separate two components. It can be defined in terms of mass or size, or any other selective property.

The size-based selectivity is defined as

$$S_d = \left| \frac{d(\log t_r)}{d(\log d)} \right| \quad (1.16)$$

where t_r is the particle retention time and d is the particle diameter.

High selectivity is a fundamental characteristic that makes FFF a valuable tool for separation and characterization because it means that there is a significant change in elution time with a small change in particle size. Hence, if zone broadening is small, high selectivity means high resolution. The resolution (R_S) is a measure of separation between two zones:

$$R_s = \frac{\Delta z}{2(\sigma_1 + \sigma_2)} = \frac{\Delta z}{4\bar{\sigma}} \quad (1.17)$$

where Δz is the gap between the centers of gravity of neighboring zones and σ is the standard deviation of the zones. The subscripts on σ refers to components 1 and 2, and $\bar{\sigma}$ refers to an average value for the two zones. Both Δz and σ are formally defined in terms of distance between and across the analyte zones, but because they appear as a ratio they may also be considered as the corresponding quantities in units of retention time.

$$R_s = \frac{\Delta t_r}{4\bar{\sigma}_t} \quad (1.18)$$

where Δt_r is the difference in retention time of the two components and $\bar{\sigma}_t$ is the average standard deviation of the two component zones in units of time.

1.2.3 Advantages of FFF

The advantages of the FFF methods are many. The separation speed, for example, can vary from a few minutes to several hours, depending on the sample and the technique. A small amount of material is required to perform an analysis. The volume injected typically varies from 2 to 20 μl of a 0.01-1% (w/v) solution or suspension. And the sample may be either dissolved or suspended in the carrier liquid. If careful attention is paid to avoid adsorption to the channel walls, the entire sample can be recovered and fractions can be collected for additional methods of analysis. A measured parameter or distribution can be confirmed using a different set of operating conditions, such as a different field strength, by using a different field type or sample amount, or by using a reinjection technique. The various FFF subtechniques permit analysis of macromolecules with molecular weights ranging from 10^3 to 10^{18} $\text{g}\cdot\text{mol}^{-1}$, or particle sizes ranging from 0.001 to 100 μm .

CHAPTER II

MAGNETISM AND MAGNETIC MATERIALS

2.1 The magnetic field

The Danish physicist and chemist Hans Christian Oersted was the first to discover that an electrical current flowing in a conductor can produce a magnetic field [6]. We now know that a magnetic field is produced by an electrical charge in motion. A magnetic field is also produced by a permanent magnet. In this case there is not a conventional electric current but the orbital motions or spins of the electrons (so called ‘Amperian currents’) present within the permanent magnetic material, leading to a magnetization within the material and to a magnetic field outside.

2.2 Basic magnetic quantities

2.2.1 The magnetic induction

The Biot-Savart law (1820) is one of the fundamental laws of electromagnetism and it can be used to determine the magnetic field \mathbf{H} generated by an electrical current

$$\delta\mathbf{H} = \frac{1}{4\pi r^2} I \delta\mathbf{l} \times \mathbf{u}, \quad (2.1)$$

where I is the current flowing in an elemental length δl of a conductor, r is the radial distance, \mathbf{u} is a unit vector along the radial direction and $\delta \mathbf{H}$ is the contribution to the magnetic field at r due to the current element $I\delta l$. See Figure 2.1.

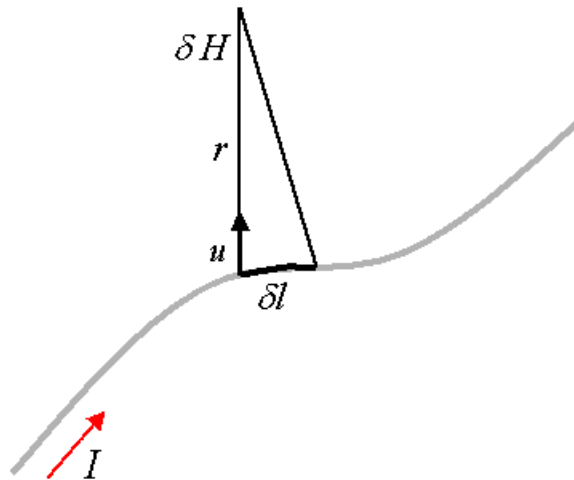


Figure 2.1. Magnetic field generated by a long conductor carrying electric current.

We can then say that a magnetic field strength of 1 ampere per meter is produced at the center of a single circular coil of conductor of diameter 1 meter when it carries a current of 1 ampere. The current passing around the loop of a conductor generates a magnetic flux Φ that is measured in units of webers. We can consider the magnetic flux to be caused by the presence of a magnetic field in a medium and the amount of flux generated by a given field strength depends on the properties of the medium. When a magnetic field \mathbf{H} is generated in a material by an applied current, the response of the material is its magnetic induction \mathbf{B} , sometimes called the flux density (measured in weber per square meter, equivalent to tesla, T).

$$\mathbf{B} = \frac{\Phi}{A} \quad (2.2)$$

In a vacuum \mathbf{B} is related to \mathbf{H} by

$$\mathbf{B} = \mu_0 \mathbf{H} \quad (2.3)$$

where μ_0 is the magnetic permeability of free space. When the magnetic field passes through some material, equation 2.3 is modified to

$$\mathbf{B} = \mu_0 (1 + \chi) \mathbf{H} \quad (2.4)$$

where χ is the magnetic susceptibility, a property of the material. Thus, $1 + \chi$ expresses the proportionality of \mathbf{B} and \mathbf{H} . We define $\mu_r = 1 + \chi$, where μ_r is the relative magnetic permeability of the material and is not necessarily constant. Either μ_r or χ can be used to characterize a material. In paramagnetic and diamagnetic materials μ_r is constant for a wide range of values of \mathbf{H} . In ferromagnets μ_r varies with \mathbf{H} . The unit systems used to measure the various magnetic quantities are shown in table II. S.I. units are used in this presentation.

Table II. Unit systems used in magnetism and relationships between some parameters

Quantity	EMU (Gaussian)	S.I. Units	Conversion factors (EMU to S.I.)
Applied field \mathbf{H}	Oersted (Oe)	A m ⁻¹	10 ³ /4 π
Magnetic induction \mathbf{B}	Gauss (G)	Tesla (T)	10 ⁻⁴
Magnetization \mathbf{M}	emu cm ⁻³	A m ⁻¹	10 ³
Magnetic flux Φ	Maxwell	Weber (Wb)	10 ⁻⁸
Magnetic moment \mathbf{m}	emu	A m ²	4 π 10 ⁻¹⁰
Permeability μ	Dimensionless	Henry/meter (H m ⁻¹)	4 π 10 ⁻⁷
Susceptibility χ	emu cm ⁻³ Oe ⁻¹	Dimensionless	4 π

To summarize, we can say that a field \mathbf{H} , measured in ampere per meter, generates a magnetic induction \mathbf{B} , measured in tesla, in a material (substance) with a permeability $\mu (= \mu_0 \mu_r)$ measured in henries per meter.

2.2.2 The magnetic dipole

A magnetic moment \mathbf{m} is associated with the elementary unit of magnetism. In the magnetic dipole the magnetic moment is equal to the product of the pole strength p measured in ampere meters and the separation between the poles l measured in meters so that

$$\mathbf{m} = \mathbf{p}l \quad (2.5)$$

\mathbf{p} can be defined as

$$\mathbf{p} = \Phi / \mu_0 \quad (2.6)$$

where Φ is the magnetic flux and μ_0 is the permeability of free space. So that the magnetic moment can be expressed as

$$\mathbf{m} = \Phi l / \mu_0 \quad (2.7)$$

The torque on a magnetic dipole of moment \mathbf{m} in a magnetic induction \mathbf{B} is

$$\boldsymbol{\tau} = \mathbf{m} \times \mathbf{B} \quad (2.8)$$

Therefore the magnetic moment can be defined as

$$\tau_{\max} = \mathbf{m} \cdot \mathbf{B} \quad (2.9)$$

where τ_{\max} is the maximum torque on a magnetic dipole. This means that the magnetic induction \mathbf{B} tries to align the dipole so that the moment \mathbf{m} lies parallel to the induction as shown in Figure 2.2.

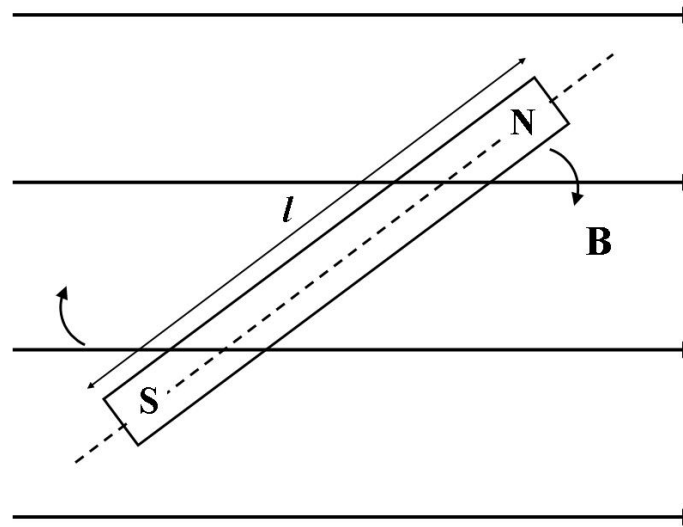


Figure 2.2. A bar magnet in an external field \mathbf{B} experiences a torque tending to align it parallel to the field direction.

2.2.3 Magnetization

The magnetization of a homogeneous material can be defined as the magnetic moment per unit volume of the material.

$$\mathbf{M} = \mathbf{m} / V \quad (2.10)$$

From the relationship given between magnetic moment and flux we can write

$$\mathbf{M} = \frac{\Phi}{\mu_0 A} \quad (2.11)$$

(where A is the cross sectional area of the material)

then,

$$\mathbf{M} = \frac{\mathbf{B}}{\mu_0} \quad (2.12)$$

2.2.4 Relation between \mathbf{H} , \mathbf{M} and \mathbf{B}

When there are no conventional external electric currents present to generate an external magnetic field, the contribution to the magnetic induction \mathbf{B} is from the magnetization \mathbf{M} of a material:

$$\mathbf{B} = \mu_0 \mathbf{M} \quad (2.13)$$

To summarize we can say that the magnetic induction \mathbf{B} is made of two contributions: one is from the magnetic field \mathbf{H} generated by electrical currents outside of the material, $\mu_0 \mathbf{H}$, and the other is from the magnetization generated by the spin and orbital angular momentum of electrons within the material. So that we can write the magnetic induction as the vector sum:

$$\mathbf{B} = \mu_0 (\mathbf{H} + \mathbf{M}) \quad (2.14)$$

2.3 Classification of materials by magnetic properties

Each substance is magnetized in a magnetic field based on its magnetic susceptibility (χ) which is substance-specific and determines the magnitude of magnetization \mathbf{M} (magnetic moment per unit volume) by a superimposed magnetic field \mathbf{H} , such that

$$\mathbf{M} = \chi \mathbf{H}. \quad (2.15)$$

The magnetic susceptibility χ can be considered the most important magnetic property of a material. It depends on the chemical composition, state, and density of the material. The various types of magnetic materials are traditionally classified according to their bulk susceptibility. The most common group is comprised of materials for which χ is small and negative $\chi \approx -10^{-5}$ (in the S.I. system of units). These materials are called diamagnetic. Their atoms have no net magnetic moment when there is no applied field. If

a field (\mathbf{H}) is applied, the electron spins produce a weak magnetization (\mathbf{M}) that opposes the applied magnetic field. For these materials it has been found that the magnetic susceptibility is independent of temperature. Most elements in the periodic table are diamagnetic; examples are copper, silver, gold, bismuth and beryllium. A second group of materials for which χ is small and positive and typically $\chi \approx 10^{-3}$ - 10^{-5} are the paramagnets. The magnetization of a paramagnet is weak but aligned parallel with the direction of the magnetic field. When such a substance is placed in a magnetic field, its atoms are subject to a torque that tends to align them with the field, but thermal agitation tends to destroy the alignment. The susceptibility of paramagnetic materials is therefore found to be dependent on temperature. The French physicist Pierre Curie was the first to discover that the susceptibility varies inversely with temperature and follows equation

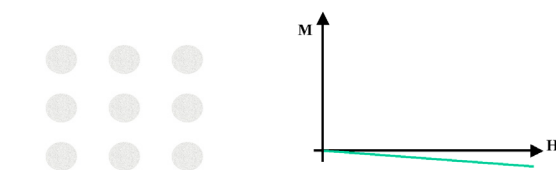
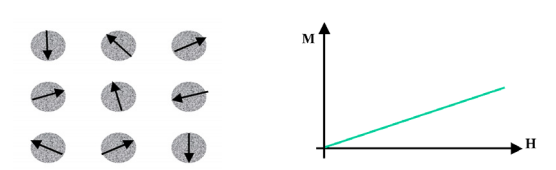
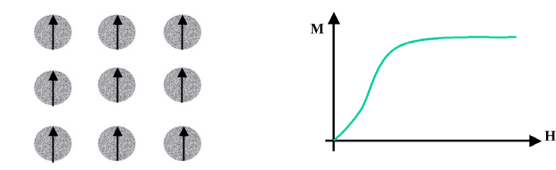
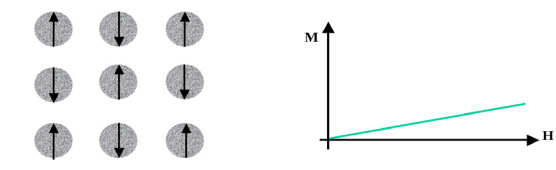
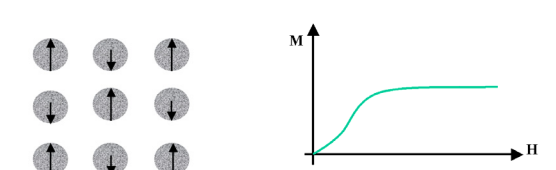
$$\chi = \frac{C}{T} \quad (2.16)$$

called the Curie law [7]. Where C is a constant known as the Curie constant. Examples of paramagnetic elements are aluminum, platinum and manganese.

The most important class of magnetic materials is the ferromagnets for which the susceptibility is positive, and usually has values $\chi \approx 50$ to 10 000. Examples of these materials are iron, cobalt and nickel and some rare earth metals (gadolinium, neodymium) and their alloys. The important characteristics of a ferromagnetic material are dependence of susceptibility on the field strength and on the previous magnetic history (hysteresis), approach of the magnetization to a finite limit (the saturation magnetization) as the field strength is indefinitely increased, the presence of small magnetized regions (magnetic domains) containing many atoms and having magnetic moments comparable with the saturation magnetization of the material even when the

material is unmagnetized (spontaneous magnetization). All ferromagnets have a maximum temperature (the Curie temperature) where the ferromagnetic property disappears as a result of thermal agitation and the material becomes paramagnetic. In some materials the atomic forces align neighboring atomic magnetic moments anti-parallel; this phenomenon is known as antiferromagnetism. Like ferromagnetic materials these materials become paramagnetic above a transition temperature, known as the Néel temperature. The theory developed by Néel [8] is based on the idea that the exchange forces will maintain neighboring atoms anti-parallel when the temperature is low enough. Ferrimagnetic materials are, in general, oxides of iron combined with one or more of the transition metals such as manganese, nickel or zinc. The five main classes of materials and the criteria by which they are distinguished from each other are summarized in table III.

Table III. Classification of materials based on their magnetic behavior.

Class	Magnetic behavior	Examples
Diamagnetic	 <p>Atoms have no permanent dipole moments.</p>	Inert gases; metals such as Cu, Hg, Bi; many ions; most diatomic molecules (H_2 , N_2); water.
Paramagnetic	 <p>Atoms have randomly oriented permanent dipole moments.</p>	Some metals (Cr, Mn); diatomic gases (O_2 , NO)
Ferromagnetic	 <p>Atoms have parallel-aligned permanent dipole moments.</p>	Transition metals Fe, Co, Ni; alloys of ferromagnetic elements.
Antiferromagnetic	 <p>Atoms have anti-parallel aligned permanent dipole moments.</p>	Many compounds of transition metals, MnO, CoO, Cr_2O_3 , MnS, $CuCl_2$, NiO.
Ferrimagnetic	 <p>Atoms have unequal permanent dipole moments. The alignment is anti-parallel.</p>	Fe_3O_4 (magnetite); γ - Fe_2O_3 (maghemite); mixed oxides of iron and other elements.

2.4 Bulk magnetic properties and their measurement

Ferromagnetic and ferrimagnetic materials have non-linear initial magnetization curves because the change in the magnetization with the applied field is due to a change in the magnetic domain structure. Weiss first postulated the existence of magnetic domains in magnetic materials in 1907 [9]. The magnetic domain is a region where the atomic magnetic moments are aligned parallel. The magnetic domains of ferromagnets have large numbers of atomic magnetic moments aligned parallel so that the magnetization within the domain is almost saturated. However, the direction of the alignment varies randomly from domain to domain. On the macroscopic scale the bulk magnetization \mathbf{M} is field induced. Thus ferromagnets become magnetized when the magnetic domains within the material are aligned (parallel). One way to obtain the alignment is to place the material in a strong external magnetic field or to pass electrical current through the material. When all the domains are aligned the material is magnetically saturated.

In 1935 Landau and Lifschitz showed that the existence of domains is a consequence of energy minimization [10]. A single domain substance has very high magnetostatic energy. The break up of the single domain into smaller regions (domains) reduces the magnetostatic energy. Hence, the reason why a magnetic material tends to be subdivided into domains is that it will always be in a state in which its energy is a minimum.

2.4.1 Magnetic anisotropy

In the absence of an external field the direction of magnetization of a domain is affected by the crystal structure. In a crystalline magnetic material the magnetic

properties depend on the direction in which they are measured. In fact they vary depending on the crystallographic direction in which the magnetic dipoles are aligned. In figure 2.3 is reported an example of the principal directions of magnetization of a single crystal of iron. In a domain in a crystal of iron not subject to external magnetic field the magnetization is always parallel to one of the crystal axes (the $[100]$ direction).

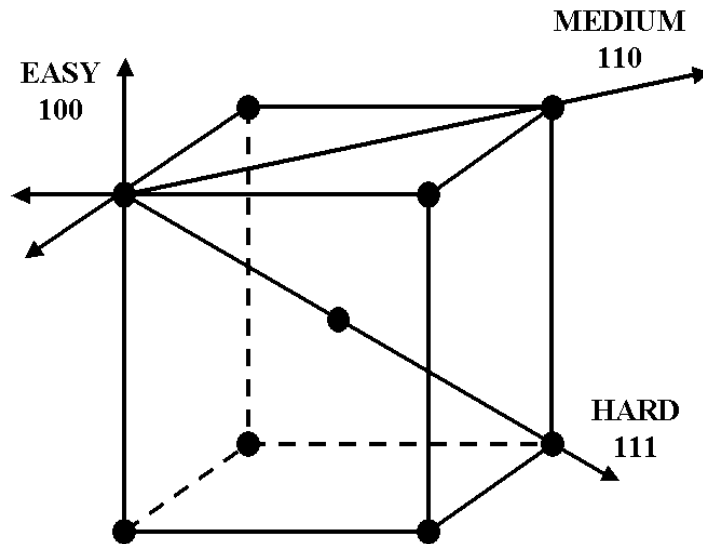


Figure 2.3. Crystal structure of single crystal of iron. The crystal structure can be magnetized easily in the $[100]$ direction, but has a hard direction of magnetization in the $[111]$ direction.

2.4.2 Hysteresis

Most of the important macroscopic magnetic properties of ferromagnets can be represented on a \mathbf{M} vs \mathbf{H} plot or hysteresis loop. A typical hysteresis curve for a ferromagnetic material is shown in Figure 2.4.

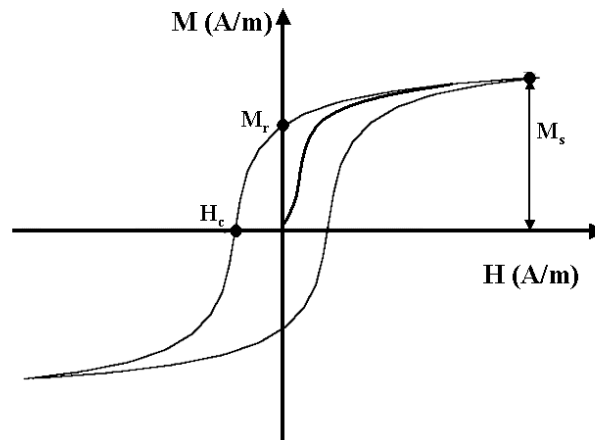


Figure 2.4. Typical hysteresis loop for a ferromagnetic material.

It is possible to define some magnetic properties of the material that can be used to characterize the hysteresis loop. In the first quadrant of the loop is shown the initial magnetization curve indicating the increase in the magnetization \mathbf{M} when a field is applied to an unmagnetized material. The applied field is positive and \mathbf{M} increases until all the domains have aligned with the applied field \mathbf{H} . At this point saturation is reached and \mathbf{M} cannot further increase. If the field is removed ($\mathbf{H}=0$) the domains align with an easy direction of magnetization, resulting in a decrease in the magnetization to the remnant magnetization \mathbf{M}_r . On the hysteresis curve we can then identify the coercive field \mathbf{H}_c that is the reversed field required to bring the magnetization to zero from remanence. The remnant magnetization \mathbf{M}_r is the largest magnetization we can get at zero field, and the saturation magnetization \mathbf{M}_s , is the maximum magnetization of the material in a strong field. The area of the hysteresis loop corresponds to an amount of energy dissipated by the material for each time the loop is completed.

2.4.3 Hysteresis effects on the magnetization

A hysteresis loop is obtained by recording the magnetization and demagnetization process as a \mathbf{B} vs. \mathbf{H} diagram, where \mathbf{B} is the flux density measured adjacent to a pole tip with a Hall-effect probe and extrapolated to its surface. The shape of the hysteresis curve depends on several factors: the chemical composition and microcrystalline structure, the crystalline orientation relative to the applied field direction (magnetocrystalline anisotropy), the sample shape and relation to the applied field direction (shape anisotropy), and the degree of mechanical cold-working as well as annealing. Every magnetic material has its own unique curve. The hysteresis is correlated to the existence of magnetic domains in the material of the pole piece. In a magnetic domain all atomic magnetic moments \mathbf{m} are parallel. In an unmagnetized ferromagnetic material, magnetic moments of the domains are randomly distributed in direction and this gives the highest entropy. The different domains are separated by domain walls, and are internally magnetically saturated. The net magnetization of the material is zero, leading to $B = 0$. When exposed to a weak external field the domains having the largest component of \mathbf{m} along the applied field direction expand their volume due to motion of the domain walls, and the adjacent non-aligned domains shrink. An intense increase of \mathbf{B} is detectable as \mathbf{H} is further increased. When most of the domains complete their wall motion there are still domains with nonzero components at different angles to the external field direction. Rotation of these domains costs more energy than the wall motion. Magnetic saturation of the material is obtained in a single domain situation, when the entropy of the system is the lowest. In such a state the process of wall motion and dipole rotation is completed and all atomic moments are aligned with the field. It is possible to further increase the

magnetic field density \mathbf{B} with increasing the field strength \mathbf{H} , but without any additional contribution from the material moment \mathbf{m} . The magnetization vector rotates back lossless, with no energy dissipation, with the small initial decrease of the external field. As the applied field decreases further the domain walls do not fully recover their original positions. Energy is required to achieve a macroscopically demagnetized state due to the tendency of domain walls to “stick”. This gives rise to hysteresis. Hysteresis loss is greater for “hard” than “soft” magnetic materials. Soft materials with high saturation magnetization and low coercivity are preferred for electromagnets, of which iron or low-carbon steel are suitable for low frequency applications where eddy currents are not a problem.

2.5 Magnetic particles and their applications

In the last few decades magnetic particles have been increasingly used for biomedical and biological applications [11]. The unique feature of magnetic particles is their response to a remote magnetic field, they are attracted to high magnetic flux density and this feature is used for drug targeting and bioseparation including cell sorting [12]. Hysteresis loss in the alternating magnetic field is a very important feature of magnetic particles, because it enables effective thermotherapy (hyperthermia). Of course, magnetic particles themselves generate a magnetic field and influence the local area around them. This feature is exploited in magnetic resonance imaging (MRI) [13]. When reduced to the nanosize scale the magnetic particles show superparamagnetic behavior [14] [15] that enables their stability and dispersion after removal of the magnetic field [16] since they do not retain any magnetization; they show high saturation field, and these features are preferred in biomedical applications.

Many materials for magnetic particles have been investigated. Highly magnetic materials such as cobalt and nickel are toxic, susceptible to oxidation and therefore of little interest [17]. The best candidate among the iron oxides is magnetite Fe_3O_4 since its biocompatibility has already been proven [18]. Magnetite, Fe_3O_4 , is a common magnetic iron oxide that has a cubic inverse spinel structure with oxygen forming a fcc (face-centered-cubic) closed packing and Fe cations occupying interstitial tetrahedral sites and octahedral sites [19]. These magnetic nanoparticles, suitably coated, can be dispersed in suitable solvents and can form homogeneous suspensions called ferrofluids [20]. At room temperature, ferrofluid particles are mobile and superparamagnetic. Below liquid nitrogen temperature, the carrier fluid is frozen and the single-domain particles become immobilized. In the absence of any surface coating the magnetic particles have hydrophobic surfaces. These particles may agglomerate and form large clusters because of hydrophobic interactions, resulting in increased particle size that will therefore show ferromagnetic behavior due to strong magnetic dipole-dipole attractions [21]. In commercially available ferrofluids (employed in biomedicine and bioseparation) the particles are coated with long chain surfactant molecules or with polymers which prevent the formation of agglomerates via the short range Van der Waals interaction [22] [23] [24]. In order to reduce the effect of the longer range magnetic interparticle interactions, ultrafine particles, with diameters of the order of 10 nm are usually used. This ensures that the thermal energy is sufficient to overcome the attractive magnetic force [25].

2.5.1 Particle magnetism

Bulk magnets are made of a large number of magnetic domains that form in order to reduce the energy of the system. Below a critical particle size, domain walls no longer

form due to energy considerations and single domain particles are stable [26]. Frenkel and Dorfman were the first to predict that a magnetic nanoparticle, below a critical size (<15 nm), would consist of a single magnetic domain [27]. The magnetic properties of nanoparticles depend mostly on the anisotropy and saturation magnetization of the material. Below the coercivity maximum the particles remain stable until the effects of temperature destroy the ferromagnetic order. The particles are then superparamagnetic [28]. The superparamagnetic size depends on the magnetocrystalline anisotropy of the material.

2.5.2 Superparamagnetism

Superparamagnetism occurs in ferromagnetic single domain nanoparticles, when the thermal energy is sufficient to change the direction of magnetization of the entire crystallite. Differently from paramagnetic particles, where each domain is independently influenced by an external magnetic field, the magnetic moment of the entire crystallite tends to align with the magnetic field. The energy required to change the direction of magnetization is called anisotropy energy barrier and is equal to

$$E_a = K_u V \quad (2.17)$$

where K_u is the anisotropy energy density and V is the particle volume. If the value of the thermal energy, kT , is comparable to the value of the energy barriers $K_u V$, then there is an increased probability of the magnetization reversing. The frequency, f , of switching from one magnetization state to the other is given by the Arrhenius-Néel equation

$$f = f_0 e^{-\frac{K_u V}{kT}} \quad (2.18)$$

where f_0 is the proportionality constant equal to 10^9 s^{-1} [29].

Néel and Brown [30], [31], [32], [33], [34], showed that for superparamagnetic nanoparticles there is a temperature, known as the blocking temperature T_B , below which ferromagnetic order reappears [35].

2.5.3 Biomedical applications of magnetic nanoparticles

The biomedical applications of magnetic nanoparticles can be classified according to their applications inside (*in vivo*) or outside (*in vitro*) the body. Hyperthermia, drug delivery and MRI are examples of *in vivo* applications [36], [37]. Cell labeling/cell separation, and immunoassay are examples of *in vitro* applications of magnetic nanoparticles [38], [39], [40], [41], [42]. For these applications the particles should be stable units composed of high concentrations of superparamagnetic nanoparticles, monodisperse in size and uniform in magnetic particle concentration [43].

Hyperthermia is a therapeutic procedure used to raise the temperature of a region of the body affected by tumor. It has been found that cancer cells heated at a temperature between 42 °C and 46 °C undergo inactivation [44], [45], whereas the normal cells can survive at higher temperatures. When magnetic particles are subjected to a variable magnetic field, some heat is generated due to magnetic hysteresis loss. The amount of heat generated depends on the nature of the magnetic material and on the magnetic field parameters and on the size and shape of the particle [14], [46], [47]. Thus having uniform particles is essential for a rigorous control of temperature.

Another promising application of magnetic nanoparticles is in drug delivery as carriers of drug for site-specific delivery. The concept was first proposed by Freeman et al [48]. They proposed the possibility of transportation through the vascular system and concentration at a particular site in the body of iron nanoparticles by the application of a

magnetic field. The particles can carry drugs or antibodies that can thus be released to the organs or tissues of interest.

MRI imaging techniques involve the use of magnetic nanoparticles as drugs administered to a patient in order to enhance the image contrast between normal and diseased tissue [49]. Iron oxide nanoparticles have been used as contrast agents to localize tumors and cardiac infarcts, for example, where the magnetic nanoparticles tend to accumulate at higher levels due to the differences in tissue composition and/or endocytotic uptake processes [50].

For *in vivo* applications the magnetic nanoparticles must be made of non-toxic and non-immunogenic material. The particle size has to be small enough to remain in circulation after injection, to pass through the capillary system of organs and tissues avoiding embolisms, and to be expelled easily through the kidneys. They also must have a high magnetization in order to be immobilized and guided to the target area with a magnetic field [51].

2.5.4 Characterization techniques for particles

Various techniques such as X-ray diffraction, electron microscopy, magnetization measurements, neutron diffraction, and light scattering allow the characterization of size and magnetization of the particles [52]. Improvements have been made in recent years in the measurement of magnetic susceptibility using the SQUID (Superconductive Quantum Interference Device) magnetometer, the vibrating sample magnetometer (VSM) [53], [54], [55]. Mössbauer spectroscopy has also become an important method for the determination the magnetic structure of a material [56], [55]. Particle size polydispersity and magnetic anisotropy are the most important particle parameters [57].

Magnetization measurements generally yield a bulk measurement, and no information concerning the distribution in magnetic moment of the particle population is obtained. Magnetic field flow fractionation has the potential of providing this information.

CHAPTER III

QUADRUPOLE MAGNETIC FIELD-FLOW FRACTIONATION

3.1 Introduction to MgFFF

Quadrupole Magnetic Field-Flow Fractionation (MgFFF) is an analytical separation and characterization technique for nano- and micro-size magnetic particles [58]. It is an elution technique, similar to chromatography in operation but not in mechanism. Quadrupole magnetic field-flow fractionation is a technique capable of fractionating magnetic particles based on the strength of their interaction with an applied magnetic field. The technique is therefore insensitive to non magnetic coatings such as dextran and antibodies to cell surface markers. Since the nature of the forces acting on the particles is known and adjustable, it is possible to calculate the magnetic moment from the retention ratio of the particles. Knowing the magnetic properties of the core material, MgFFF can be used to determine the size distribution as well as the mean size of the magnetic cores of particulate samples that are broadly polydisperse in their magnetite content. This type of analysis could be invaluable for quality control purposes in the production of immunospecific magnetic nanoparticles. It may also be used as a

preparative tool to reduce sample polydispersity, although such use is limited due to the small sample size.

The instrumentation, similar to a High Performance Liquid Chromatography (HPLC) system, comprises an HPLC pump (to provide a flow of carrier fluid), a sample injection valve, a separation channel, a quadrupole magnet, an HPLC detector, a Teslameter (to monitor the magnetic field strength), and a computer for data acquisition. The instrumental set up is shown in Figure 3.1.

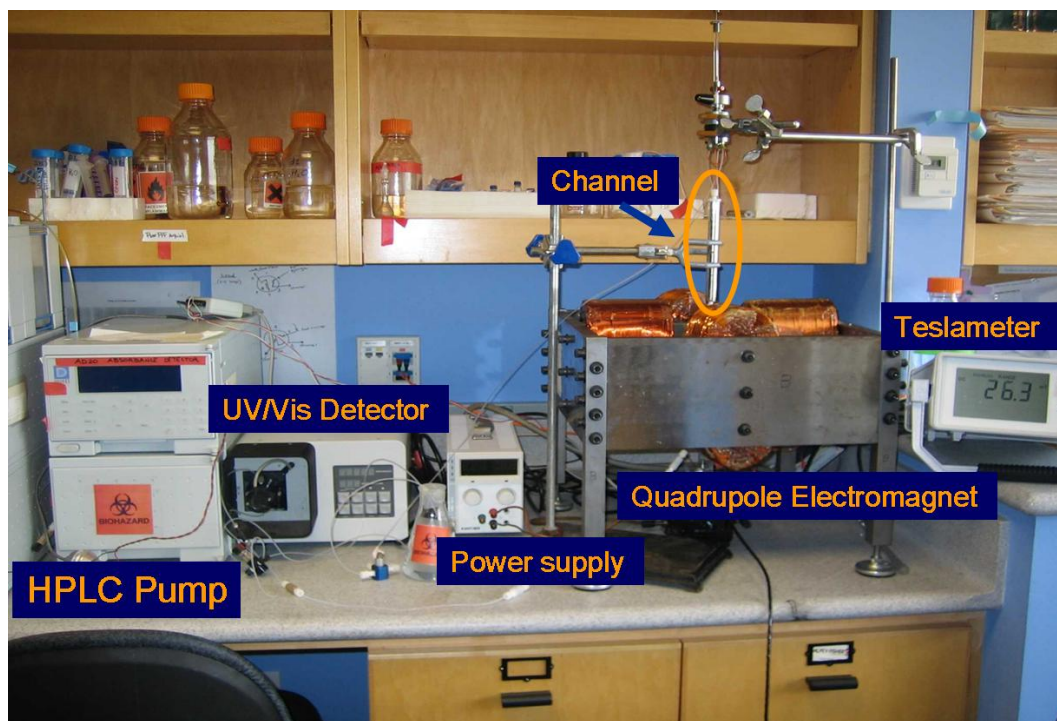


Figure 3.1. MgFFF instrumentation setup.

3.1.1 Theory of MgFFF

The quadrupole magnetic FFF device differs from all previous implementations of magnetic FFF in that it utilizes an axially symmetric magnetic field with the channel occupying a thin annular space within the field.

As already explained in Chapter I, the nanoparticles inside the channel approach a steady state when the field-induced particle migration toward the wall is balanced by a back-diffusion, the result being that the particle concentration decays exponentially from the accumulation wall. The elution time of the particles from the channel is determined by this balance between the field-driven and diffusive transport mechanisms. Particles that interact strongly with the field gradient form thin zones close to the accumulation wall (for example, zone A in Fig. (3.2)). These zones are therefore carried to the channel outlet by relatively slowly moving fluid streamlines. Particles that interact less strongly with the field gradient form thicker, more diffuse zones and are carried by to the channel outlet by faster-moving fluid (for example, zone B in Figure 3.2).

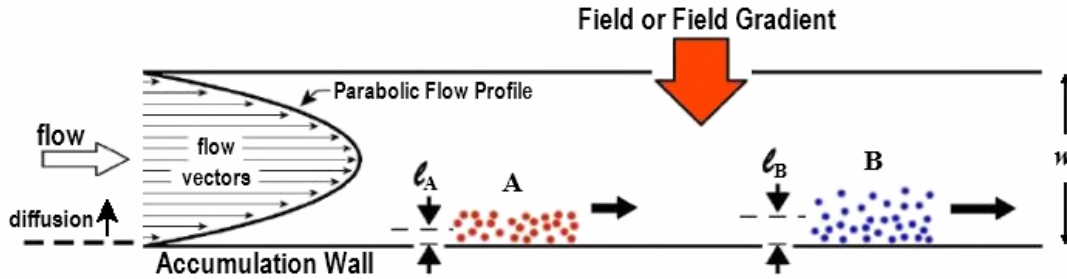


Figure 3.2. Schematic of a section of the channel thickness illustrating the retention mechanism.

The thicknesses ℓ_A and ℓ_B in Figure 3.2 correspond to the mean thicknesses for zone A and B, respectively. Thus, in the case of MgFFF, the higher the magnetite content of the particles, the longer is their retention time inside the channel. The concentration profile across the channel thickness resulting from the balance of field-induced and diffusional transport is given by

$$c = c_0 \exp\left(-\frac{x}{w\lambda}\right) \quad (3.1)$$

in which c_0 is the concentration at the accumulation wall, x is the distance from the accumulation wall, w is the channel thickness, and λ is the so-called retention parameter given by

$$\lambda = \frac{D}{|u_m|w} = \frac{kT}{|F_m|w}, \quad (3.2)$$

where D is the particle diffusion coefficient, u_m is the field-induced velocity of the particle, k is the Boltzmann constant, and T is the absolute temperature. Since the field-induced velocity and the force on a particle are toward the accumulation wall, they have negative values and the absolute values $|u_m|$ and $|F_m|$ are used in equation 3.2. The retention parameter λ is equal to the ratio of the mean zone thickness ℓ to channel thickness w . Note that the value of λ is independent of the overall particle size; it is dependent on the induced force on the particle which is proportional to the mass of magnetic material incorporated in the particle. Assuming that the velocity profile for the thin channel is parabolic, it follows that the retention ratio, or the ratio of elution time of a nonretained material t^0 to a retained material t_r , is given by

$$R = \frac{t^0}{t_r} = 6\lambda \left(\coth\left(\frac{1}{2\lambda}\right) - 2\lambda \right) \approx 6\lambda(1 - 2\lambda). \quad (3.3)$$

The final approximated form on the right-hand side of equation 3.3 is accurate to within 0.37% for $\lambda < 0.15$. With knowledge of the channel volume and the volumetric flow rate of the carrier solution (mobile phase), the nonretained time t^0 may be calculated. This time, also known as the void time, is commonly indicated by a sharp initial peak in the elution profile or fractogram. A retention time may be related to a value of λ according to equation 3.3, and this to a magnetic force on the particles eluting at this time by equation 3.2.

3.1.2 Interaction of particles with fields

In general, particles may be characterized in terms of the strength of their interaction with a field. This relationship may be written in the form

$$\mathbf{F} = \phi \mathbf{S} \quad (3.4)$$

where \mathbf{F} is the force exerted on the particle, \mathbf{S} is a quantitative measure of the field, and ϕ is a so-called particle-field interaction parameter. In the case of a centrifugal field, for example, ϕ represents the particle buoyant mass and \mathbf{S} the acceleration. A similar approach can be employed to describe particle interaction with magnetic fields. Just as buoyant mass may be reduced to a per unit volume quantity $\Delta\rho$, magnetic dipole moment may be reduced to the per unit volume quantity (the particle magnetization \mathbf{M}).

3.1.3 Magnetic force on particles

The magnetic force on a particle in a magnetic field is a function of its magnetization and the gradient in the field strength. The force \mathbf{F}_m on a particle due to its interaction with the magnetic field gradient is given by

$$\mathbf{F}_m = V_m M \nabla B, \quad (3.5)$$

where V_m is the volume of magnetic material in the particle (the coating is assumed to have negligible magnetization), M is the magnetization of this material which aligns with the local field vector, and ∇B is the gradient in magnetic field B which in the quadrupole is directed radially outward from the axis. It follows that the force exerted on paramagnetic or ferromagnetic particles is also directed radially outwards.

In the case of a paramagnetic material, magnetization M varies linearly with magnetic field H , as described by the equation $M = \chi_m H$, in which χ_m is the volumetric magnetic susceptibility of the material and is a constant (typically between 10^{-3} and 10^{-5}). In the

case of a ferromagnetic or superparamagnetic material, magnetization approaches an upper limit called the saturation magnetization \mathbf{M}_s , so that χ_m is not constant. The initial value of χ_m is much greater than 1 for ferromagnetic materials, and typically can have values between 50 and 100,000. Particles may be suspended in a weakly diamagnetic medium such as an aqueous electrolyte solution which has a negative susceptibility of order of 10^{-5} . In this case, for the fluid,

$$\mathbf{H} = \frac{\mathbf{B}}{\mu_0(1 + \chi_f)} \approx \frac{\mathbf{B}}{\mu_0}, \quad (3.6)$$

where χ_f is the volumetric susceptibility of the medium and μ_0 is the magnetic permeability of free space, and we obtain

$$\mathbf{F}_m = \frac{V_m \chi_m}{\mu_0} (\mathbf{B} \cdot \nabla) \mathbf{B} = \frac{V_m \chi_m}{2\mu_0} \nabla (\mathbf{B} \cdot \mathbf{B}) = V_m \chi_m \frac{\nabla B^2}{2\mu_0} \quad (3.7)$$

Here we assumed that the magnetic particles are free to rotate in the magnetic field. The

force is therefore dependent on the product $V_m \chi_m$ of the particle, and $\frac{\nabla B^2}{2\mu_0}$ describing the

magnetic field. In the terminology of FFF, force is given by the product of a particle-field interaction parameter ϕ and a measure of the field strength \mathcal{S} . A direct or indirect measure

of the force on a particle situated in a magnetic field of known $\frac{\nabla B^2}{2\mu_0}$, corresponding to \mathcal{S}_m ,

therefore yields a value for $V_m \chi_m$, which is simply the particle-magnetic field interaction parameter ϕ_m .

Very small particles of ferromagnetic material that are sub single domain in size behave superparamagnetically. They reach a saturation magnetization \mathbf{M}_s that aligns with \mathbf{B} at

relatively modest field strengths. In this case the magnetization is a non linear function of field strength, and the force is given by

$$\mathbf{F} = V_m (\mathbf{M} \cdot \nabla) \mathbf{B} = V_m M \nabla B = \frac{V_m M}{H} \frac{\nabla B^2}{2\mu_0} \quad (3.8)$$

At high field strengths, where magnetization approaches a constant saturation value, the force varies with ∇B rather than with ∇B^2 . Given that our measure of field strength S_m

corresponds to $\frac{\nabla B^2}{2\mu_0}$, then $\phi_m = V_m M_s / H$, and ϕ_m is not constant. In all the systems

considered here, the particulate materials are in a fluid suspension, so that any measure of a force exerted should strictly take into account the magnetic property of the suspending fluid. Magnetic labels are composites of different materials. There must be magnetic and antibody components to the label, but there can be other components too. The magnetic component may be dispersed within another material, or may be distributed on the surface of a polymer bead. There may be a stabilizing coating on the magnetic material to prevent aggregation of the suspended beads or to prevent their chemical breakdown. If the label is to have any utility, the strongly magnetic component will dominate the overall value of ϕ , but the magnetic properties of the other components should also be considered. (All materials have some degree of magnetic susceptibility, and we shall use the term “weakly magnetic” to refer to these other materials.) For a composite particle having a (strongly) paramagnetic component, it may be shown that

$$\mathbf{F}_m = V_p \left(\phi_m \chi_m + \phi_w \chi_w - \chi_f \right) \frac{\nabla B^2}{2\mu_0} = V_p \Delta \chi \frac{\nabla B^2}{2\mu_0} \quad (3.9)$$

where V_p is the volume of the particle, ϕ_m and ϕ_w are the volume fractions of the strongly magnetic and weakly magnetic components, χ_m , χ_w , and χ_f are the susceptibilities of the

strongly and weakly magnetic components and the fluid, respectively, and $\Delta\chi$ is the difference in the overall susceptibility of the particle and the suspending fluid. Note that we gather all weakly magnetic components together in the interest of simplicity, and their net behavior may be paramagnetic or diamagnetic. If both $\phi_w\chi_w$ and χ_f are negligible compared to $\phi_m\chi_m$ then the force equation reduces to

$$F_m = V_p \phi_m \chi_m \frac{\nabla B^2}{2\mu_0} = V_m \chi_m \frac{\nabla B^2}{2\mu_0}, \quad (3.10)$$

(as already shown in equation 3.7), where V_m is the volume of the magnetic component in the particle. If the magnetic component is superparamagnetic, and exhibits non linear dependence of magnetization on field strength, the force is given by

$$F_m = V_p (\phi_m M + \phi_w \chi_w H - \chi_f H) \nabla B = V_m M \nabla B + V_p (\phi_w \chi_w - \chi_f) \frac{\nabla B^2}{2\mu_0} \quad (3.11)$$

Again, if both $\phi_w\chi_w$ and χ_f are negligible then this equation reduces to

$$F_m = V_m M \nabla B \quad (3.12)$$

where again V_m is the volume of the magnetic component in the particle. In both cases, retention time will tend to increase with the volume of magnetic component, or the cube of its effective spherical diameter. If the relationship between magnetization and field strength is known for the core material, then the volume of the core (or the equivalent volume for a dispersed material in the particle) may be obtained via equation 3.12. The elution profile or fractogram (concentration vs. elution time), for a sample may, therefore be transformed into a mass or number distribution of equivalent spherical core diameters. It is common practice in FFF to gradually reduce the field strength during the elution of polydispersed samples [59], [60]. This is known as field programming (to be discussed in Chapter VI). These conditions have the effect of hastening the elution of the more

strongly retained fractions while adequately retaining those fractions that are less influenced by the field at high initial field strength. As the field and field gradient decay, the force on the eluting particles F_m falls and the retention parameter λ and, therefore, the retention ratio R increase. Any arbitrary field and field gradient decay may be accounted for in relating a retention time to the volume of magnetic material per particle by numerically solving the integral equation [61].

$$\int_0^{t_r} R dt - t^0 = 0 \quad (3.13)$$

3.1.4 Magnetophoretic mobility

Magnetophoresis is the process of particle motion in a viscous medium under the influence of a magnetic field. The magnetic particles and the medium are considered responsive to the imposed magnetic field, and the material property that describes the response to the external magnetic field is the relative magnetic permeability, μ_r , and the magnetic susceptibility, χ .

The magnetic particle in the imposed magnetic field behaves as a magnetic dipole. In a uniform magnetic field the net force on the magnetic dipole is zero, and there is no translational motion of the magnetic particle. To cause the translational motion of a magnetic particle, a non-uniform magnetic field is necessary, with both the field magnitude and the field gradient playing a role. The characteristic property of the magnetic particle that causes it to move in a non-uniform magnetic field is defined as its magnetophoretic mobility, m . It is the normalized velocity of the migration of particles in a homogeneous magnetic field, so that

$$m = u_m / S_m = u_m / \nabla \left(\frac{B^2}{2\mu_0} \right).$$

Where S_m is a measure of the magnetic force field strength (magnetic energy gradient), B is the magnetic induction, and μ_0 is the magnetic permeability of free space. The difference in magnetophoretic mobility between different particles establishes a basis for magnetic separation in viscous media. The particle magnetophoretic mobility is an important parameter for rational magnetic separation design.

3.2 Cell Tracking Velocimetry (CTV)

Cell Tracking Velocimetry is an instrument developed in-house that enables the user to measure magnetophoretic mobility (MM) of many individual particles or cells for a sample of suspension (hundreds to thousands) and subsequently to calculate the particle magnetization. The CTV consists of a rectangular borosilicate glass channel inside of a magnet assembly, a microscope with an attached CCD camera and a personal computer with image acquisition and post-processing software. The mean magnetic field in the viewing area is 1.4 T; the mean field gradient is 350 T²/m. For measurement, the channel is filled with a cell or particle suspension. The microscope objective focuses on a region of isodynamic field characterized by a constant energy density gradient ($\nabla B^2/2\mu_0$, where B is the magnetic field intensity and μ_0 is the magnetic permeability of free space) whose non-zero component lies entirely in the focal plane of the microscope. The magnetically susceptible cells and particles migrate with a constant velocity orthogonal to the $B^2=\text{const.}$ contour lines. By adjustment of the contrast between the background and the particle image, and by adjustment of other user-defined parameters (such as aspect ratio, minimum and maximum size of particle image), the particles are tracked across the stack of frames collected by the camera. The camera is operated at 30 Hz and the operator has a control over the frequency of frame acquisition (the skip-frame option). The final CTV-

output, processed by EXCEL software package macros (EXCEL, Microsoft Corp., Redwood, WA) gives graphs and statistics of the MM of the tracked particles. The cell magnetophoretic mobility, MM, is defined as the cell velocity induced by the magnetic field divided by the magnitude of the vector $\nabla B^2/2\mu_0$. A complete description of the method can be found elsewhere [62] [63] [64].

3.3 Earlier implementations of magnetic FFF

There have been previous attempts to implement magnetic FFF, with varying degrees of success. In 1980, Vickrey and Garcia-Ramirez [65] attempted to demonstrate magnetic FFF by coiling a 304 cm Teflon tube of 0.15 cm internal diameter against the windings of a 400 Gauss (0.04T) electromagnet. The coiled tube lay close to the plane of one end of the iron core. Non retention of the Ni-BSA complex sample was observed, which is not surprising given the far from ideal tubular channel geometry [2], the low field strength, and the channel position in a region of low field gradient.

Schunk, Gorse and Burke [66] [67] reported in 1984 the use of a parallel plate channel with a magnetic field provided by an electromagnet. The channel was made of 0.5 in (1.27 cm) and 0.125 in (0.32 cm) thick glass plates separated by a 250 μm spacer. The thinner wall was placed in contact with one end of the iron core of the magnet to maximize field strength and field gradient in the channel. A maximum field strength of about 275 Gauss (0.0275 T) and field gradient of about 21 Gauss/mm (2.1 T/m) were obtainable, with less than 1% variation in field strength along the length of the channel. They were able to separate singlet from doublet 0.8 μm rod shaped iron oxide particles used in the recording industry (i.e., fairly large, high susceptibility particles). Semenov and Kuznetsov [68], in 1986, proposed the use of a ferromagnetic wire at the axis of a

tubular channel placed perpendicular to a magnetic field that magnetized both the wire and the particles to be separated. They presented calculations that suggested retention of both paramagnetic and diamagnetic particles was possible in such a system. The coaxial channel geometry is also far from ideal. The force on retained particles would rapidly increase as the wire is approached, which would tend to induce particle capture. Also, the small surface of the wire would have to serve as the accumulation wall, which would make the system highly susceptible to overloading. In the same year, Semenov [69] proposed a parallel plate channel in which the field would be provided by the induced magnetization of parallel ferromagnetic wires arrayed uniformly in the surface of one of the walls. The wires were to lie in the direction of flow and the field was to be applied across the channel breadth, perpendicular to the wires and the flow direction. He presented a theoretical study of the proposed system and concluded that it would be more efficient than the coaxial system. Such an arrangement would help to alleviate overloading, although the strong spatial variation in force on the particles would remain.

Also in 1986, Mori [70] reported an attempt to demonstrate magnetic FFF using a system very similar to that of Vickrey and Garcia-Ramirez [65]. He used a Teflon tube of 0.5 mm internal diameter and length 270 cm, 210 cm of which was coiled against a pole of a 9000 Gauss (0.9 T) electromagnet. Very slight retardation of Ni^{2+} complexes with BSA, egg albumin, and EDTA was observed. Although Mori used a stronger field strength than in the earlier system [65], and the tube was placed against the pole piece rather than the electrical coil, the field gradient would not have been very high and the tubular channel geometry is not suited to FFF.

From 1994, Ohara and co-workers [71], [72], [73], [74], [75], [76], [77], [78], [79], have pursued an approach to magnetic FFF similar in concept to that proposed by Semenov [69]. The majority [71], [72],[73], [74], [75], [76], [77],[78] of their publications describe theoretical studies and simulations. Tsukamoto et al. [72], considered a set of stacked channels with ferromagnetic wires embedded in the dividing walls. The stacking of channels was to maximize throughput of the system. The wires were assumed to be parallel to one another and in the direction of fluid flow. An external magnetic field was to be applied across the channel thicknesses, perpendicular to the wires and to the fluid flow. It was assumed that wires of 10 μm diameter would be embedded in 10 μm thick walls with 10 μm thick channels between them, and that a 10 T magnetic field would be applied. The feasibility of separating 20 nm particles of uranium from plutonium was examined. It is apparent from this, and from following publications, that the system would suffer from the very localized distribution in concentration close to the wires due to the rapidly increasing field gradient as the wires are approached.

Subsequent papers by Ohara and co-workers [73], [74], [75], [76], [77], [78], [79], consider single channel systems, and refer to the technique as magnetic chromatography, even though no partition between phases is involved. Regularly spaced wires were assumed to be embedded within the two walls of the channel, each wire being matched by another directly across the channel thickness. In 2002, Mitsuhashi et al. [79] reported an experimental implementation. The channel was 45 cm long, 2.7 cm wide and 190 μm thick. Wires were embedded in both channel walls and lay in the direction of fluid flow. They were of rectangular cross section, being 150 μm broad and 30 μm thick. They were embedded into the walls to a depth of 30 μm , so that they were flush with the

wall surfaces, and spaced 150 μm apart. Rather than the wires of one wall being arranged exactly opposite the wires of the other, they were offset by 150 μm so that wires in each wall lay opposite spaces between wires in the other. An external field of 3 T was applied. They were able to show slight retention of some transition metal salts, although band spreading was extremely high.

In 1996, Nomizu et al. [80] introduced a technique they also referred to as magnetic chromatography that used a column packed with 0.7 μm carbon–steel beads and a periodically intermittent magnetic field. This technique has more in common with a form of FFF known as cyclical FFF [81] [82] than chromatography. In cyclical FFF, a major part of the migration along the channel occurs when particles are driven away from the wall by a periodic reversal of the field direction. The particles therefore spend some time entrained in faster streamlines further from the flow boundaries. The distance migrated during a field reversal is proportional to the particle mobility, provided the opposite channel wall is not encountered. Higher mobility particles are therefore predicted to migrate into faster fluid regions and elute before those of lower mobility. (Giddings [81] showed that this is strictly true when the particle excursion is limited to 0.75 of the channel thickness.) Nomizu et al. [80] did not propose a mechanism for their technique, but I can provide the following explanation. When the field is applied, the rate of migration of particles to the packing surface would be proportional to their mobility. Those of higher mobility would be quickly captured and immobilized, while those of lower mobility would be carried further down the column before being captured. With interruption of the field, the migration of particles from the packing surface would be due to the drag of the carrier fluid (aided by a continuous vibration applied to the column),

rather than by the influence of the reversed field used in cyclical FFF. The migration away from the capture surface would be independent of mobility provided remnant magnetization of the packing can be ignored. According to this mechanism, the lower mobility particles would elute before those of higher mobility. Nomizu et al. [83] later presented an open tubular design where the separation tube was placed along the circular edge of an electromagnet pole piece. The mechanism of operation would correspond to that of the packed column system, except that the transport of particles away from the wall on removal of the field would depend on diffusion and hydrodynamic effects. They were able to baseline separate 0.7 μm hematite particles from 0.6 μm magnetite particles, with hematite eluting before magnetite as expected. An improved result was obtained by gradually increasing the zero field periods during elution.

CHAPTER IV

DEVELOPMENT OF THE SYSTEM

4.1 Description of the system

The quadrupole magnetic FFF system being developed in our laboratory will now be described. As mentioned previously, the device differs from all previous implementation of magnetic FFF in that it utilizes an axially symmetric magnetic field with the channel occupying a thin annular space within the field.

4.1.1 The quadrupole field

In the region between the poles of a quadrupole magnet, the field strength B increases in magnitude linearly with radial distance r from the axis according to the equation

$$B = \frac{B_0 r}{r_0} \tag{4.1}$$

where B_0 is the magnitude of the field strength at the radial distance r_0 .

The field gradient is therefore constant throughout this region:

$$|\nabla B| = \frac{B_0}{r_0} \quad (4.2)$$

It follows that the radial force on a paramagnetic particle increases linearly with radial distance from the axis and is ideally independent of angle [84], as shown in fig 4.1.

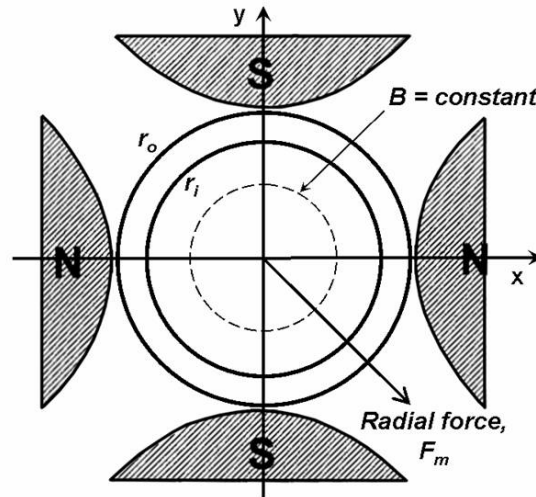


Figure 4.1. The quadrupole magnetic field. The helical channel occupies a thin annular space between the inner and outer radii, r_i and r_o , respectively. The thickness of the annulus is exaggerated in the figure for clarity.

This is quite different to the rapid variation of field gradient found in High Gradient Magnetic Separators (HGMS) which are designed to trap particles. There is, in fact, a relatively small variation in field strength across the channel thickness. This is analogous to asymmetrical FIFFF. In asymmetrical flow FFF [85], the cross channel drag force increases from zero at the depletion wall to a maximum at the accumulation wall. Such a variation does not significantly affect the separation capability of asymmetrical flow FFF compared to the conventional, symmetrical variant. The relatively small variation of force across the thickness of the channel occupying a thin annular space, coaxial with the magnet assembly, can therefore be expected to be of little importance. Furthermore,

particles that are magnetically saturated in the annular region occupied by the channel would experience a constant outward radial force, which is consistent with the ideal FFF model. The magnetic field must be as uniform as possible along the channel length. This is achieved by confining the channel within the quadrupole assembly such that the fringing effects close to the ends of the pole tips are avoided. The channel occupies an annular space between radial distance r_i and r_o , as shown in figure 4.1, thereby avoiding the axial region where field strength is small. The constant field gradient in the quadrupole allows for the maintenance of a steady-state distribution of diffusing magnetic nanoparticles adjacent to a channel wall which is a requirement for elution in the normal mode of FFF. In the earliest experiments performed on magnetic microspheres and red blood cells, two different permanent quadrupole magnets (named B1 and B2) were employed. Figures 4.2 and 4.3 show the design, specific measures and materials employed for their construction. Only the analyses performed on magnetic nanoparticles utilized the quadrupole electromagnet that was developed later.

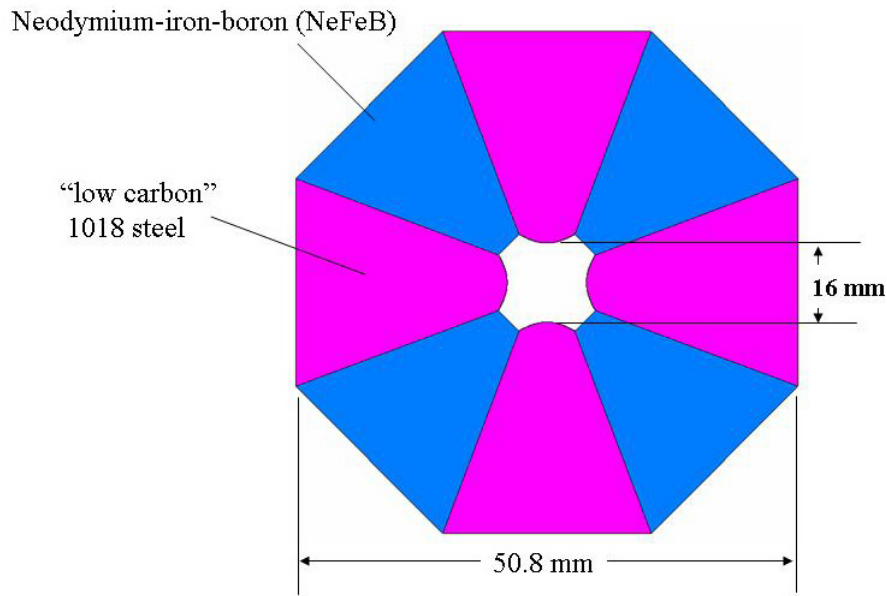


Figure 4.2. Top view of a cross section of the quadrupole magnet B1. It has been employed for the analysis of red blood cells. It generates a magnetic field of 1.42T at the radial distance of the pole tips.

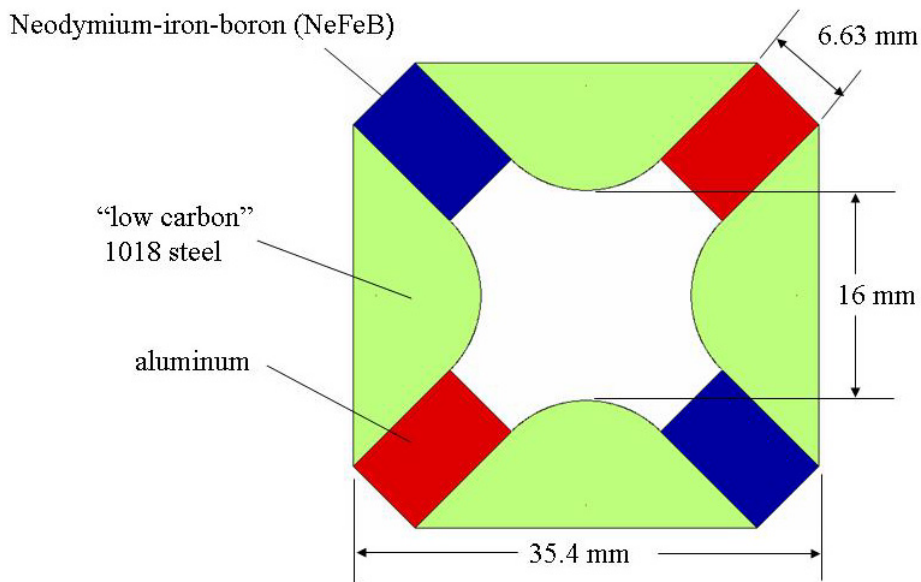


Figure 4.3. Top view of a cross section of the quadrupole magnet B2. It has been employed for the analysis of magnetic microspheres. It generates a magnetic field of 0.071T at the pole tips.

4.1.2 The helical channel

To exploit the axially symmetric quadrupole field gradient, the MgFFF device employs an innovative helical channel design. An early prototype channel was designed to occupy the full annulus between a polymer cylinder and an outer stainless steel tube. The channel ends were sealed and the tube held concentric to the cylinder with rubber o-rings. The carrier fluid and sample were introduced via several inlets around the circumference, and collected via several outlets feeding a single tube to the detector. Such a design has several drawbacks. Uniform carrier fluid flow demands a high degree of uniformity in annular thickness around the circumference and along the length. Any variation in annular thickness around the circumference would offer varying resistance to flow, and hence varying mean flow velocities along the length of the channel. Variation in annular thickness along the channel length, due to the outer tube or inner rod distortion or to non-uniform o-rings, could lead to carrier fluid velocity components around the circumference as fluid finds the path of least resistance. The multiple inlets and outlets would also be liable to partial or even complete blockage by bubbles or sample materials. All of these factors would lead to broadening of the range of elution time for each sample component, and hence a loss of separation efficiency. Most of these drawbacks could be avoided by restricting the channel to a fraction of the annulus. Multiple (say, up to four) channels could even be arranged in parallel, each with a single inlet and outlet. Since multiple channels would be unlikely to be used simultaneously, a better solution was conceived in which a single channel takes a helical path from a single inlet to a single outlet. This could be achieved by cutting a spiral channel into the surface of a hard polymer cylinder (DelrinTM, du Pont) that fits tightly into a stainless steel tube. The tight

fit eliminates the need for rubber o-rings and the problem of deviation from concentricity. The uniformity in channel thickness across its breadth and length is also ensured by the tight fit of the uncut surface of the cylinder within the tube. There are additional advantages to the helical channel design. Small non-uniformities in the magnitude of the magnetic field strength around the circumference are sampled equally by all sample particles as they migrate along the channel. In the case of an annular channel, these non-uniformities would contribute to loss of separation efficiency. The helical channel may also be considerably longer than the quadrupole magnet, and therefore any annular channel, and for fixed field strength and mean fluid velocity, separation efficiency is directly proportional to channel length, with all of the parameters unchanged. Two different channels have been used in our studies. One is 500 μm thick and its geometry is shown in Figure 4.4. The channel was machined by the Cleveland Clinic Foundation Prototype Laboratory to a depth of 500 μm into the surface of a precision-turned Delrin™ (du Pont) cylinder of 0.586 in (1.488 cm) diameter and 6.20 in (15.75 cm) length. An internally polished, 6.10 in (15.49 cm) long, 304 stainless steel tube served as the accumulation wall. This had an outer diameter of 0.625 in (1.588 cm), and wall thickness of 0.020 in (0.051 cm). The channel was assembled by exploiting the difference in coefficients of thermal expansion of the two components with immersion in liquid nitrogen. An excellent channel seal was obtained on return to room temperature. The channel made six complete spirals around the cylinder, had an overall length of 5.50 in (13.97 cm), with 5.00 in (12.70 cm) between inlet and outlet ports. The cutting tool had a diameter of 0.500 in (1.27 cm), resulting in a depletion wall breadth of 0.455 in (1.156 cm) perpendicular to the direction of flow. The channel had an effective length

(along the flow path) of 31.4 cm, and a nominal volume of 1.90 ml. The second channel, shown in Figure 4.5, had a thickness of 250 μm , it made four complete turns around the cylinder, had an overall length of 15.75 cm. The channel had an effective length of 23.5 cm, and a nominal volume of 0.94 ml.

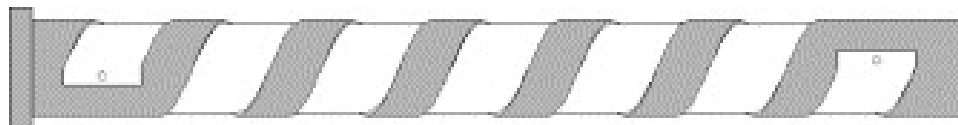


Figure 4.4. The helical channel geometry machined into the surface of the polymer cylinder. The original surface of the cylinder is shown in gray with the machined area white in order to highlight the spiral path of the channel. The inlet and outlet ports are shown as small circles at the ends of the channel.



Figure 4.5. Longitudinal section of the 250 μm thick helical channel inserted into the stainless steel cylinder. The inlet and outlet ports are shown as small circles at the ends of the channel.

4.2 Assembly of the quadrupole electromagnet and the evaluation of its magnetic field

A quadrupole electromagnet was designed and built for use with the helical magnetic field-flow fractionation channel. As previously discussed in Chapter II, ferromagnetic materials such as iron, nickel, cobalt or their compounds can be permanently magnetized by an eternal magnetic field. The magnetization of a

ferromagnetic material depends on the value of the applied field as well as the sample magnetic history. The magnetic field induction is described by

$$\mathbf{B} = \mu_0 \mu_r \mathbf{H} \quad (4.3)$$

$$\mathbf{M} = (\mu_r - 1) \mathbf{H} \quad (4.4)$$

(4.3) and (4.4) combined give the Sommerfeld equation

$$\mathbf{B} = \mu_0 (\mathbf{H} + \mathbf{M}) \quad (4.5)$$

where μ_r and μ_0 are the relative magnetic permeability of the material and the magnetic permeability of free space, respectively. \mathbf{H} is the field strength and \mathbf{M} the magnetization of the material. The magnetization is equal to the magnetic moment per unit volume within the material. In our case the field is created by electric coils. Inside a long solenoid the field strength \mathbf{H} is proportional to the current of magnetization, here called I ,

$$H = \frac{NI}{l} \quad (4.6)$$

where N is the number of turns and l the length of the solenoid. Combining (4.3) and (4.6) leads to calculation of the flux density of the ferrous material inside the solenoid.

4.2.1 Temperature effects

For a fixed current I , the resistance is proportional to the measured voltage, using Ohm's law

$$R = \frac{V}{I} \quad (4.7)$$

where R is the resistance, and V is the voltage. As the four coils are wired in parallel, the DC resistance of each of the four coils should be the same in order to provide a symmetric magnetic field; the resistance depends on the resistivity ρ , the wire cross section area A and the wire length L

$$R = \frac{L \rho}{A} \quad (4.8)$$

The copper resistivity increases with temperature, and use of the electromagnet leads to Joule heating, causing the coil resistance to increase. At constant voltage, the current would decrease and cause a decrease in the magnetic field. In this study, a current-regulated power supply was used, thus the voltage increases with increasing resistance to maintain constant current. A power supply with sufficient voltage headroom was selected based on the anticipated resistance rise. The mean coil temperature can be estimated from the measurement of voltage at constant current, as will be shown in the following derivation. The dependence of the resistivity on temperature is given by:

$$\rho - \rho_{20} = \rho_{20} \alpha (T - 20^\circ C) \quad (4.9)$$

Here the subscript “20” refers to the resistivity at 20°C, a common reference point given in the literature; α is a material property known as the temperature coefficient of resistivity, assumed to be constant if the temperature range is not too large. For the most commonly used conductor, copper, $\alpha = 3.9 \times 10^{-3}/^\circ C$. Combining (4.8 and 4.9) and simplifying leads to:

$$R - R_{20} = \alpha R_{20} (T - 20^\circ C) \quad (4.10)$$

where R_{20} is the resistance at 20°C. With Ohm’s Law, we show the linear relationship between resistance rise and voltage rise at constant current:

$$R - R_{20} = (V - V_{20}) / I \quad (4.11)$$

The mean temperature of the coil is obtained by combining the previous two equations:

$$T = 20^\circ C + \frac{V - V_{20}}{\alpha V_{20}} \quad (4.12)$$

Temperature change is important for several reasons. The magnetization of the iron flux return yoke is a complex function of temperature and field strength. At low H , the induction rises with temperature, but at high H (>1.6 kA/m) the induction decreases with temperature, falling precipitously above 600°C (Metals Handbook, 1998). At the Curie temperature (e.g. for low carbon steel $T_c = 770^{\circ}\text{C}$) the ferromagnetic material of the pole pieces and the yoke loses its ferromagnetic properties and becomes simply paramagnetic. Further, heating of the iron yoke can lead to heat transfer to the FFF channel, leading to temperature-dependent density gradients of the internal fluid, and disturbed flow. Of course, with very large temperature increase there could be phase change. Fortunately, because of the large mass of the electromagnet assembly (on the order of 100 kg), the large surface for convective heat transfer, as well as the experimental conditions typically at low and decreasing currents, the temperature change is often just a few degrees Celsius. In one experiment, when the coils were operated for one hour at full power (5.16A total and 1.29 A/coil), a condition unlikely to be encountered in FFF analysis, a mean temperature rise of about 43 degrees was measured, as described below.

4.2.2 Experimental Procedure

The first step was to develop an experimental procedure that allows the operator to return to a reference point of $B = 0$ when $I = 0$, regardless of previous use of the electromagnet. The second step was to develop a relationship between the power supply current and the field, accurately evaluated and reproducible.

For an un-magnetized system, point (a) in Figure 4.6, an increase of the current I leads to the initial magnetic curve (a-b). Point (b) in the plot represents the maximum field that can be generated by the current provided by the power supply. With the

decreasing of I , the demagnetization curve displays higher field values along (b-c) compared to the magnetization curve (a-b). The magnetization current I is zero at point (c), but there is still a positive magnetic field remaining, the so-called remnant field B_r . Reversing the polarity and raising I decreases the magnetic field below B_r . Point (d) corresponds to the coercivity H_c where the measured field is zero. Here the net magnetic moment of domains aligned with the field equals the net moment of those anti-parallel with the field. From a macroscopic perspective, this demagnetized state is the same as the initial un-magnetized state, but microscopically, these two states are very different. A further increase of I (with the reverse polarity to the initial current) results in a magnetic field that is equal in strength to that of point (b) but opposite in direction (point(e)). If the power supply could generate a large enough current, the ferrous yoke would become saturated, and this would occur at an H value corresponding to the intrinsic coercivity, H_{ci} . A similar point exists on the positive axis.

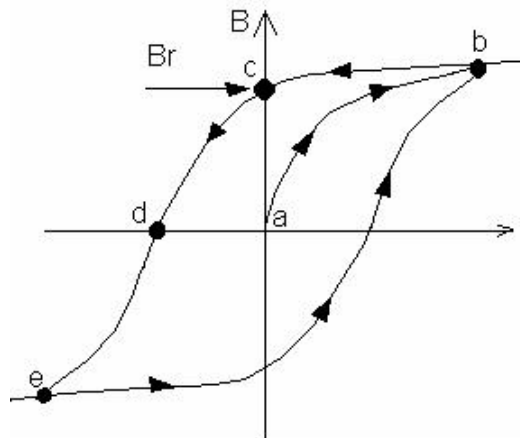


Fig.4.6: Hysteresis curve showing dependence of the field strength B on the applied current I .

An important consequence of the hysteresis on the magnetization is that there is no unique relationship between the magnetization current and the field. However, it is possible to follow a minor hysteresis curve in a reproducible way. A minor hysteresis loop must fall inside the boundaries defined by the major hysteresis loop, (examples are shown in Figure 4.7). Changing the maximum value of the current at which the experiment starts, results in working with a different minor hysteresis curve. As implied above, we must always work on some minor hysteresis loop as the power supply cannot generate enough current to bring the material to saturation. Two methods were used to evaluate $B = f(I)$ for the minor hysteresis curves used for the programmed field decay employed in the MgFFF experiments. The first method, shown in Figure 4.7 and developed by Steffen Steinert, was subsequently improved, as described later in this chapter.

For this initial approach the entire system had to be demagnetized before starting an experiment. The initial magnetization therefore always followed the curve (a-b). The principle of the demagnetization procedure is shown in Figure 4.7. The system is initially set to the maximum value of current (point b) and then returned to zero current. The current polarity is then reversed and set to the value I_{demag} (point e) (calculations are shown in the following sections). The current is then again returned to zero which results in demagnetization of the yoke (point a). The method for running a programmed decay of field is to increase the current to the required initial value, and then decrease the current in a controlled manner as the fractionation takes place, until the current returns to zero and B reaches one of the reduced remnant fields corresponding to one the points I,

II, III, or IV, as shown in Figure 4.7. This means that B versus I data must be collected for each of these minor, first quadrant, hysteresis curves to generate unique $B = f(I)$.

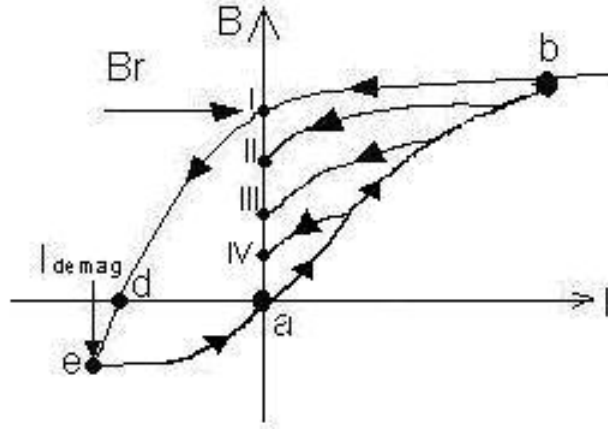


Figure 4.7. Schematic of the demagnetization procedure (from point b to point e) and the minor hysteresis curves for different values of maximum current. The curves lead to different values of remnant fields (points I, II, III, and IV in the diagram).

4.2.3 Materials and Methods

The quadrupole electromagnet was constructed of 6.00 in (15.24 cm) wide, 1.00 in (2.54 cm) and 0.75 inch (1.91 cm) thick, 1018 low-carbon, cold rolled steel plate (Cumberland, Steel Division, Cleveland, OH), machined at the Cleveland Clinic LRI Prototype Laboratory. The cores for the electromagnet coils were 1.00 in (2.54 cm) thick, 6.00 in (15.24 cm) deep, and 6.76 in (17.16 cm) long, tapering inward at 15° on each side toward the pole tips over a length of approximately 1 in (Fig. 4.8). The pole tips were machined to the required hyperbolic function for the 1.60 cm diameter aperture, allowing sufficient clearance for the FFF channel. The function defining the hyperbolic pole tip shape was

$$\frac{x^2}{a^2} + \frac{y^2}{b^2} = 1 \quad (4.13)$$

where constants a and b are evaluated to 8 mm.

The square external yoke, which provided the return path for magnetic flux, was made of the 0.75 in thick steel plate. The magnet cores were bolted to the yoke plates, which were in turn bolted to 1.00 in square steel supports at the corners. The coils of #18 AWG coated copper were wound by CWS Coil Winding Specialist (Santa Ana, CA). A cross sectional schematic and the assembly of the electromagnet are shown in Figures 4.8 and 4.9. The coils were wired in parallel and the current was provided by a Xantrex HPD60-5 Series Programmable Power Supply (Xantrex Technology Inc., Burnaby, British Columbia, Canada). This power supply was capable of supplying up to 5 A at up to 60 V, and was controlled by a computer using a GPIB interface (also from Xantrex Technology Inc.), and this allowed for the programmed decay of current (and hence field strength) during sample elution. For switching between magnetization and demagnetization current, a 15A rocker switch was used [DPDT (double-pole double-through) with neutral central position]. The three positions were labelled:

- “mag”: current for magnetization
- “off”: no current flows through the coils
- “demag”: inverted connections allow current for demagnetization.

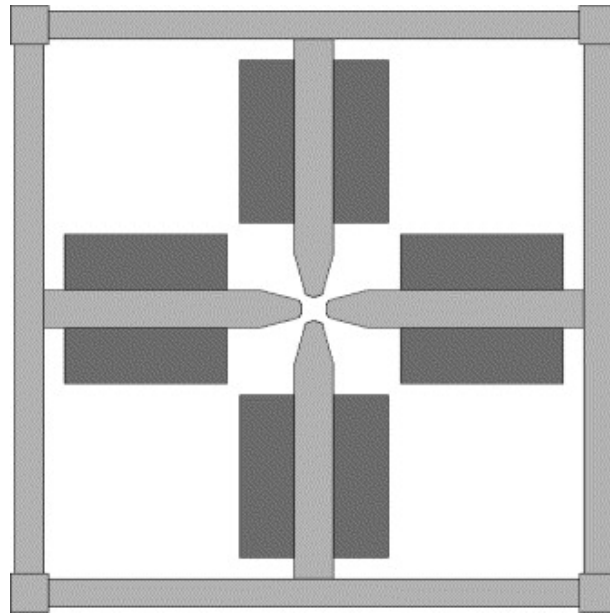


Fig. 4.8. Schematic of the quadrupole electromagnet cross section. The low-carbon steel pole pieces and yoke are shown in pale gray, and the copper coils in darker gray. The stainless steel tube that encloses the MgFFF helical channel fits snugly between the four pole tips at the aperture, with a nominal tolerance of 0.005”.



Fig.4.9. Assembled electromagnet.

4.2.3.1 Coil design

The following relationship was derived to estimate the total coil length with succeeding layers:

$$L = \sum_{i=1}^N L_i = \sum_{i=1}^N \frac{y_0}{d} [2x_0 + 2z_0 + 8d(i-1)] \quad (4.14)$$

N is the total number of layers, i is the layer number, d is the effective wire diameter (copper core with insulation plus a factor to allow for winding imperfection), x_0 is the core width (25.4 mm), y_0 is the axial length of the coil (114.3 mm), and z_0 is the core depth (152.4 mm). This length, when used with equation 4.8, allows estimation of the room temperature resistance as a function of layer number. Bare 18 gauge wire has a diameter of 1.024 mm, so the value chosen for d was 1.30 mm. The desired coil room temperature DC resistance was 34 ohms, or 8.5 ohms for the circuit (four coils in parallel). For a power supply of maximum voltage 60V providing a current of 5A, would allow the circuit coil resistance to rise to 12 ohm, or 48 ohm/coil, due to Joule heating. With equation 4.10, we see that sufficient voltage headroom exists to allow a temperature rise of up to 105 °C.

After assembly, the 4 coils create a quadrupole field with a maximum flux density of 0.71 T at the maximum circuit current of 5A. The resistances of the coils at room temperature were found to lie between 35.6Ω and 35.8Ω, and the coils connected in parallel to the power supply give a net resistance of 8.535Ω. A simulation of the magnetic field using Magneto 5.1 (Integrated Engineering Software, Winnipeg, Canada), shown in Figure 4.10, predicted a maximum field strength at the pole tips of 0.818 T at a current of 1.25 A through each coil.

A maximum field strength of 0.71 T was measured at this current using a Model 6010 Gauss/Tesla Meter (SYPRIS, Test & Measurement, F.W. Bell, Orlando, FL).

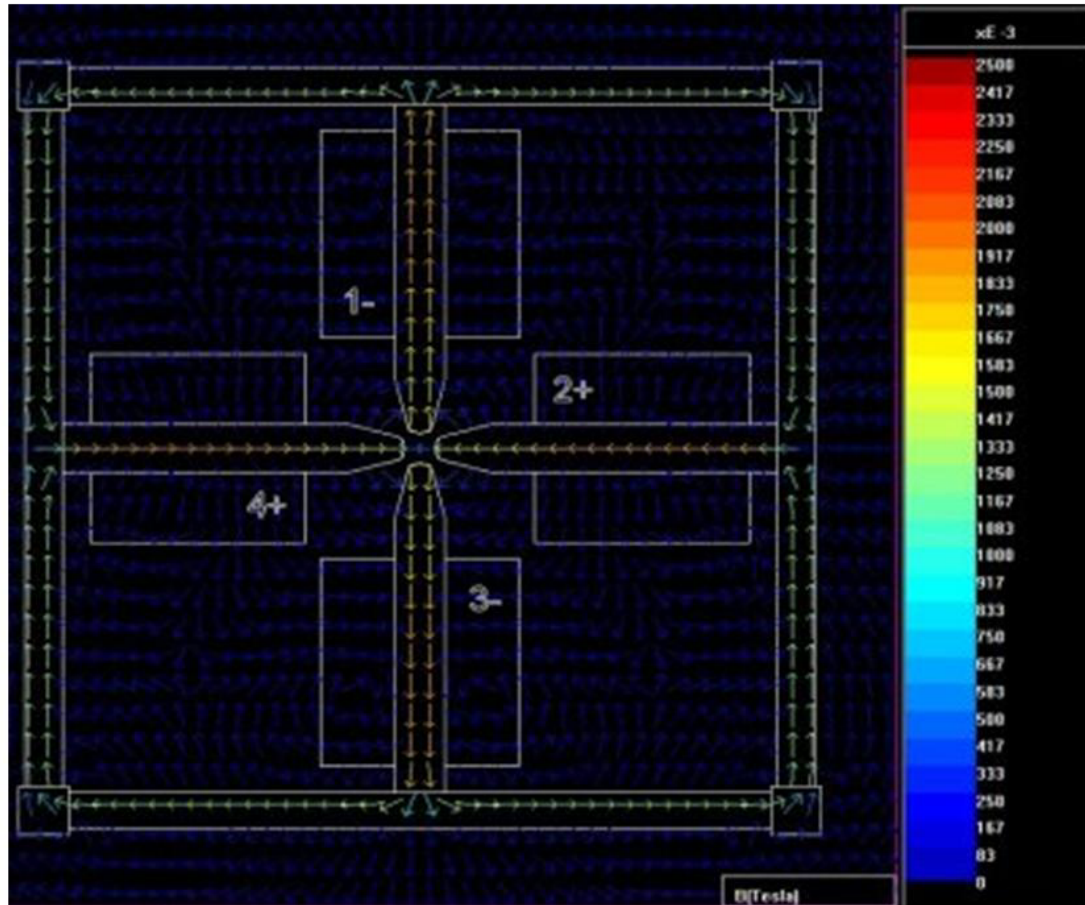


Fig.4.10. Simulated magnetic field density vectors of the quadrupole electromagnet and polarization of the coils (provided by Lee R. Moore).

4.2.3.2 Hall-effect probe principle of operation

A Hall-effect probe was used for measurements of the magnetic field. The probe is placed in the magnetic field and the transverse voltage is measured. A current flowing through the conductor and the external field creates a transverse force on the moving electrons that pushes the charges to one side of the conductor. The buildup of charge separation balances the magnetic influence and produces a measurable voltage. The voltage is measured using a Gaussmeter (Gaussmeter F.W. Bell Model 9200, Orlando, FL), which displays the corresponding magnetic field using the following equation

$$B = \frac{V_{Hall} n e c}{I} \quad (4.15)$$

where V_{Hall} is the transverse voltage, n the charge carrier density of the carrier electrons, e the electron charge, c the thickness of the Hall probe and I is the internally used current across the Hall probe. The polarity of the field determines the lateral direction of motion of the electrons.

The measured flux densities are extrapolated to the surface of the pole tips, r_0 , under the assumption that the probe evaluates B at the center of its thickness. The correction makes use of the fact that B is linear in r in a quadrupole field:

$$\frac{r}{r_0} = \frac{B}{B_0} \rightarrow B_0 = \frac{r_0}{r} B \quad (4.16)$$

By substitution of the measured values:

$$c = 1.016 \text{ mm}$$

$$r_0 = 8 \text{ mm}$$

$$r = r_0 - c/2 = 8 \text{ mm} - 0.508 \text{ mm} = 7.492 \text{ mm}$$

we obtain equation

$$B_0 = 1.068 B \quad (4.17)$$

Where c is the Hall probe thickness, r_0 the quadrupole magnet aperture radius, B the measured field and B_0 is the corrected field strength at the surface of the pole pieces.

Figure 4.11 shows a schematic of the position of the probe at the pole tip.

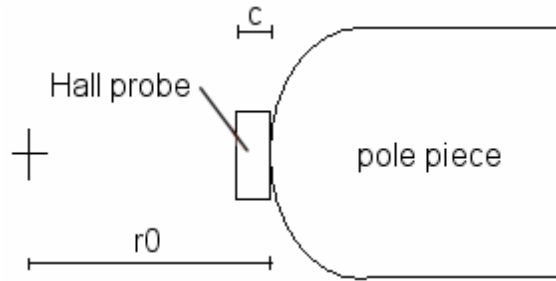


Figure 4.11. Schematic of Hall effect probe at the surface of a pole tip.

4.2.4 Results

1. Demagnetization of a single coil

The first step was to find the demagnetization current I_{demag} for each coil in order to negate the remnant field caused by the maximum current of $I = 5A$, as explained earlier.

The procedure is as follows:

- calibrate the Hall probe of the Gaussmeter
- position the probe inside the magnet aperture using a 2D micrometer stage (x-y translation stage, Newport, CA) underneath the magnet so that the sensing area is located at the middle of the axial pole piece length, flat against the pole tip, as shown in figure 4.8.
- magnetize the coil with 5A in “mag” position
- set the DPDT switch to “off” position
- decrease the current to zero
- bring the DPDT switch to “demag”
- choose the value for I_{demag}
- switch to “off”
- check the magnetic field value displayed on the Gaussmeter

- iterate the process to find the best I_{demag} value so that after the last round of the demagnetization cycle the remnant magnetic field is zero to within $\pm 1\text{mT}$.

The (nonlinear) dependency of the de-magnetization current, I_{demag} , on the maximum initial magnetization current is shown in Figure 4.12. The results are for one coil.

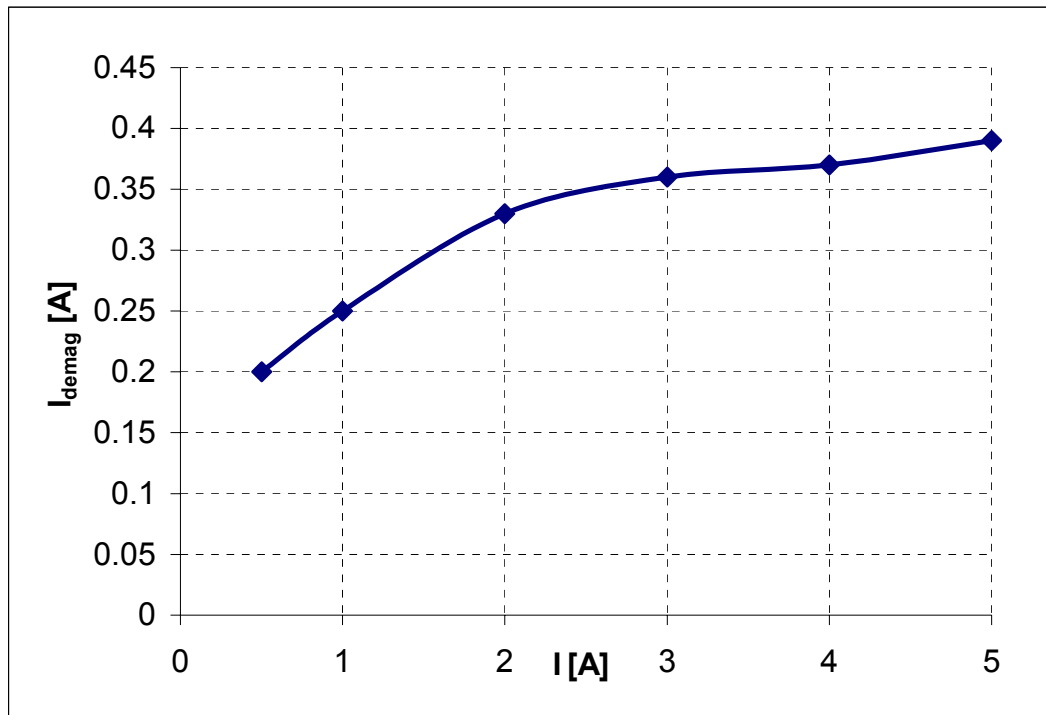


Figure 4.12. Required demagnetization currents for different maximum magnetization currents in one coil.

4.2.5 Adjustment of electrical coil resistance

The magnetization curve was recorded for each coil using the appropriate I_{demag} current. The values are shown in Figure 4.13.

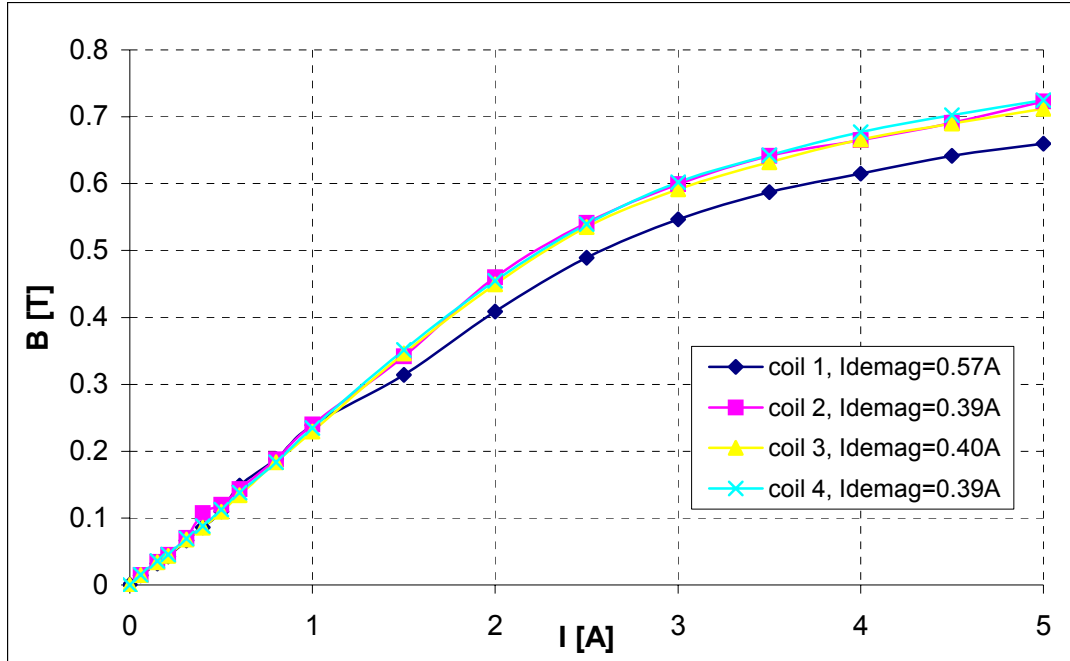


Figure 4.13. Magnetization of coils with 4 individual demagnetisation currents

As shown in Figure 4.13, coil 1 gave a lower magnetic flux density than the other three, which were similar to each other. The shift was caused by a higher resistance of coil 1, leading to a lower current (equation 4.5, 4.6, 4.7). This is an undesirable effect that had to be corrected in order to maintain proper, axi-symmetric field geometry inside the aperture. The high coil resistance was corrected by partially unwinding the coil and cutting the excess wire length. Knowing the average resistance of the other 3 coils and the specific resistance of copper it was possible to calculate the length of wire that had to be cut as shown in the following equations:

$$R_1=35.9\Omega \quad (4.18)$$

$$R_2=35.8\Omega \quad (4.19)$$

$$R_3=35.6\Omega \quad (4.20)$$

$$R_4=35.7\Omega \quad (4.21)$$

where R_1 , R_2 , R_3 , and R_4 are the resistances of coil 1, 2, 3, and 4, respectively.

$$\Delta R=R_1 - \frac{R_2 + R_3 + R_4}{3} = 0.2\Omega \quad (4.22)$$

$$L = \frac{A \Delta R}{\rho} = \frac{\pi 1.024^2 mm^2 0.2\Omega}{4 0.017\Omega mm^2/m} = 10.2 m \quad (4.23)$$

After removing the appropriate length of wire from coil 1 the values of B vs I for the four coils were measured again. The curves are shown in Figure 4.14. It should be noted that the curve for coil 1 is significantly closer to the curves of other coils, resulting in an improved symmetry of the quadrupole field.

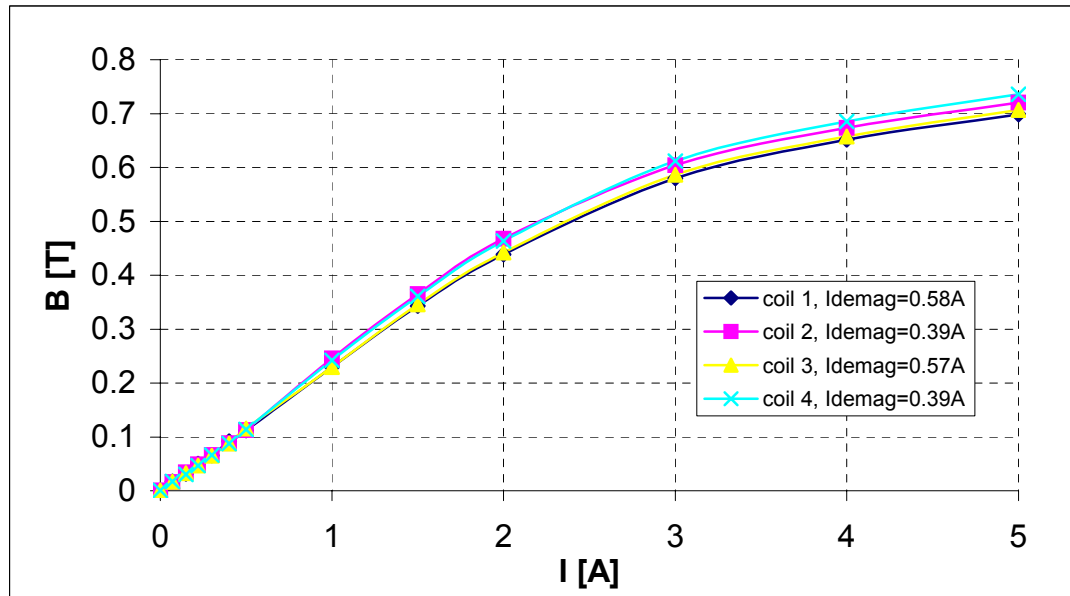


Figure 4.14. Magnetization curves with individual I_{demag} after correcting resistance of coil 1.

4.2.6 Simultaneous demagnetization of the four coils

In order to demagnetize the quadrupole electromagnet – not just single coils - independent of its magnetization history, a magnetization current of 5A and an average demagnetization current for the four coils, calculated to be equal to $I_{demag} = 0.48A$, was

used. When the current was reset to $I = 0$ the system was demagnetized, measuring a negligibly low B . As previously explained, the reason for applying a magnetization current of 5A is to eradicate the effect of previous magnetization history by driving the assembly to near saturation. This procedure was found to be reproducible and independent of the magnetization history.

4.2.7 Determination of the working reference curve for a single coil

The next step was to characterize again each coil using the new average demagnetization current $I_{demag} = 0.48A$ in order to determine the reference curve and examine its accuracy. The following procedure was applied to the four coils separately, one at the time.

First magnetization step:

- position the switch to “mag”
- demagnetize one coil using the demagnetization procedure, as shown before
- increase I from 0A to 5A in small increments and record the magnetic field intensity for each discrete current.
- decrease I from 5A to 0A
- switch to “demag”
- increase the current magnitude until magnetic field density falls to zero

Second magnetization step:

- decrease the current back to 0A
- switch to “mag”
- increase I to 5A
- decrease back to zero

- switch to “demag”

- increase the demagnetization current again until the magnetic field is zero

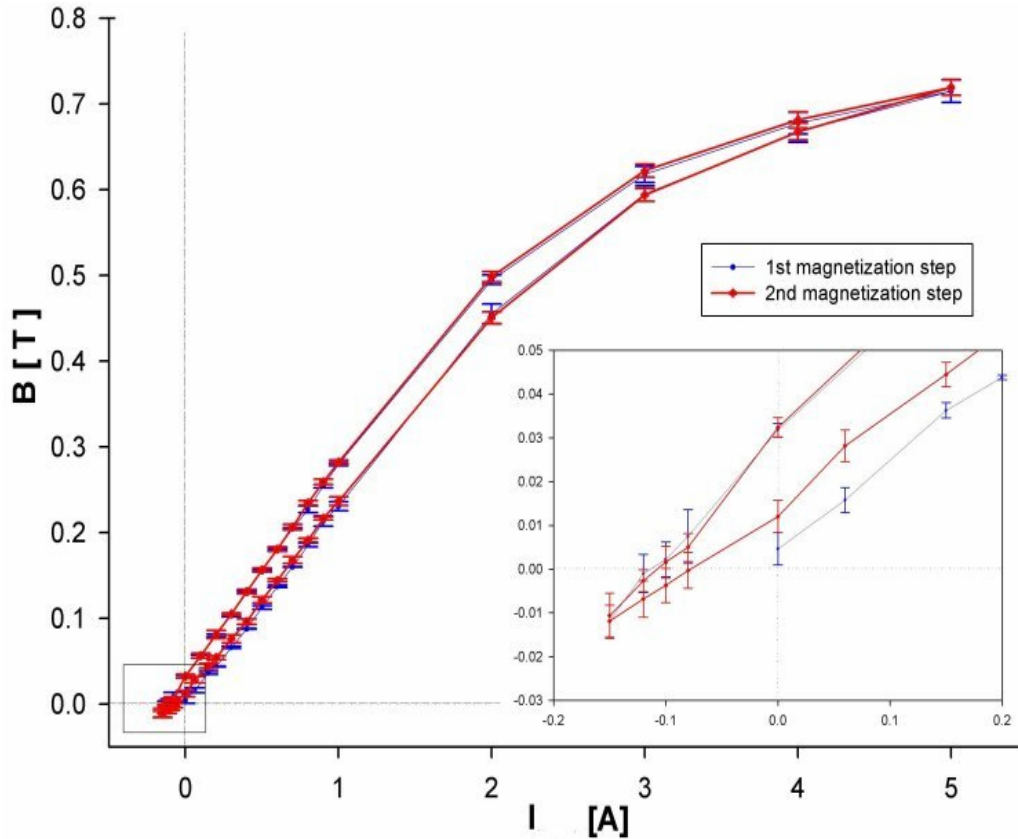


Figure 4.15. Mean field intensity for the four pole pieces and standard deviation for the 2 magnetization steps.

The reorientation of the magnetic moments due to the change of the current towards a positive magnetization, after the first magnetization step ($B = 0$ T), requires an activation energy to initiate the inter-domain wall motion. This leads to a shift in the magnetization during the second step, as shown in Figure 4.15.

4.2.8 Coil heating

During the experiments the voltage was increased from 46.0 V to 49.2 V in the period of 1 hour operating the electromagnet with constant 5.16 A, resulting in a calculated mean coil temperature (equation 4.12):

$$T = \frac{49.2V - 46.0V}{0.0038K^{-1} \cdot 46.0V} + 25^{\circ}C = 43.3^{\circ}C \quad (4.24)$$

This mean temperature of 43.3-degree is well within the 105-degree limit corresponding to the power supply's maximum voltage. The temperature of the pole pieces and the yoke can not exceed the coil temperature due to imperfect heat conduction and loss of heat to the surroundings from the surface.

4.2.9 Error analysis

The reasons for the deviations from the mean of the measured flux density can be:

- limited accuracy of the Gaussmeter
- incorrect positioning of the Hall probe relative to the pole piece
- short overshoots of required current related to regulation by the power supply (resulting in change of B value, because of the polepiece hysteresis)
- deviation from the axial symmetry of the field
- changes of the relative permeability of the yoke due to heating of the coils and the yoke during the experiments can cause changes in the flux densities
- small differences in the material properties of the pole pieces related to cold working

For some of the MgFFF experiments a very low field is required in order to elute particles that are highly magnetic. In Figure 4.15 it is shown that the standard deviation between the four pole pieces decreases with lower current; the relative error is shown in the next diagram.

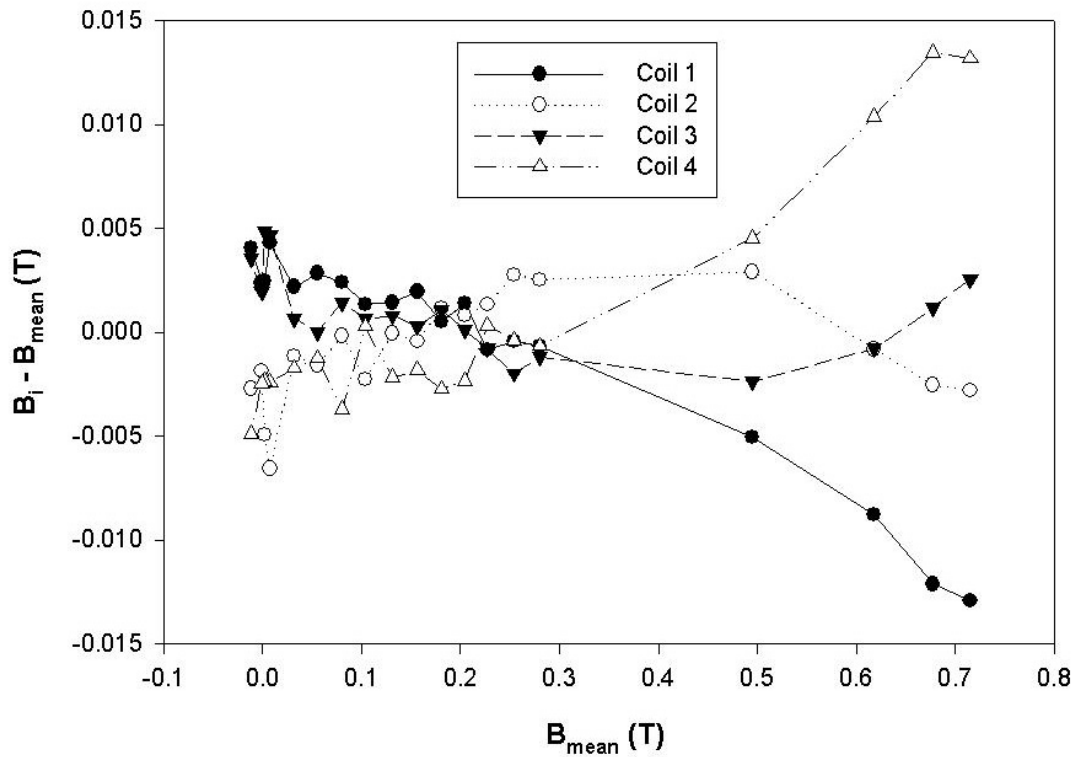


Figure 4.16. Deviation from the mean B for 4 coils for decreasing B from 0.71T to 0T.

The relative error is in the range of $\pm 2\%$ for $B > 0.1\text{T}$. The variation of the magnetic field between the 4 coils is compensated for by the helical structure of the MgFFF channel. The particles move in the helical path and are forced to interact with 360° of the magnetic field.

Conclusion

The quadrupole electromagnet was assembled to provide an accurate symmetric magnetic field for MgFFF. The results of this investigation agree quite closely with the theory. A reliable procedure to demagnetize the system was established. The next step was to connect the power supply to a PC to provide a means for programmed field decay for the elution of polydisperse samples.

4.3 New method for the determination of minor hysteresis curves

In the previous section a method was described which gave predictable and reproducible B versus I relationships. To recapitulate, the method was to 1) raise the magnetization current to +5A, 2) bring the current to 0, then reverse the polarity switch and proceed to I_{demag} , 3) bring the current back to 0 at which point the flux circuit would be demagnetized, then 4) reverse the polarity switch and raise the current to give the desired initial B required for the FFF experiment, in which case, 5) the current would be slowly lowered to 0, as the fractionation took place, resulting in one of the remnant fields I – IV shown in Figure 4.7. The above method was rather complex and required the I_{demag} value to be precisely reached. Further, it had the undesirable feature of resulting in high B_r values. The reduction in remnant field is important when working with samples with high iron content that might be permanently entrained in the column due to their interaction with the field. A new procedure giving reproducible B versus I relationships was devised that differs from the previous one, in that it doesn't require reaching the demagnetization current. Instead the method is 1) set the polarity switch is set to negative or "demag" and bring the current to -5A (point f in Figure 4.17) to reverse the polarity of the flux material's domains, as much as possible, short of saturation, then 2) bring the current back to 0 at which point the flux circuit still has a net negative magnetization, 3) reverse the polarity switch to positive "mag" orientation and raise the current only as far as needed to yield the initial B required for the experiment. 4) During the program field decay, the current is gradually lowered to 0 resulting in a remnant field, for example, I, II, III or IV, shown in Fig. 4.17. The remnant fields are lower than in the previous method for the same initial currents. The reader will notice that it is possible to achieve 0 flux

density from any initial field, as in the case of point d, corresponding to the coercivity. However, with the apparatus in its present form this would require manually switching the current polarity, as it is not possible to switch the current polarity with PC control of the power supply, which lacks a polarity switch.

Figure 4.15 shows how the functional relationship between B and I is derived using this new method. In this case, the positive or “mag” current is taken to 5A, as described in step 3 above, and lowered in small increments down to 0 as B is measured at one of the pole tips. The process is repeated for all of the pole tips and the B data are averaged for each I .

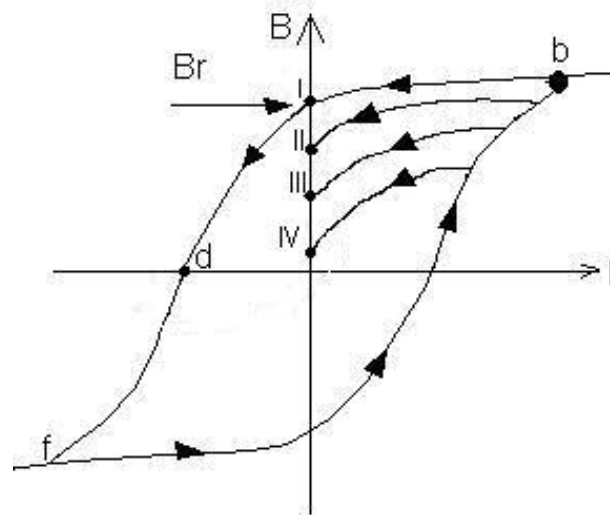


Figure 4.17. Improved method for producing predictable B versus I profile.

Four Pole Average
I = range (5.0 - 0.0) A

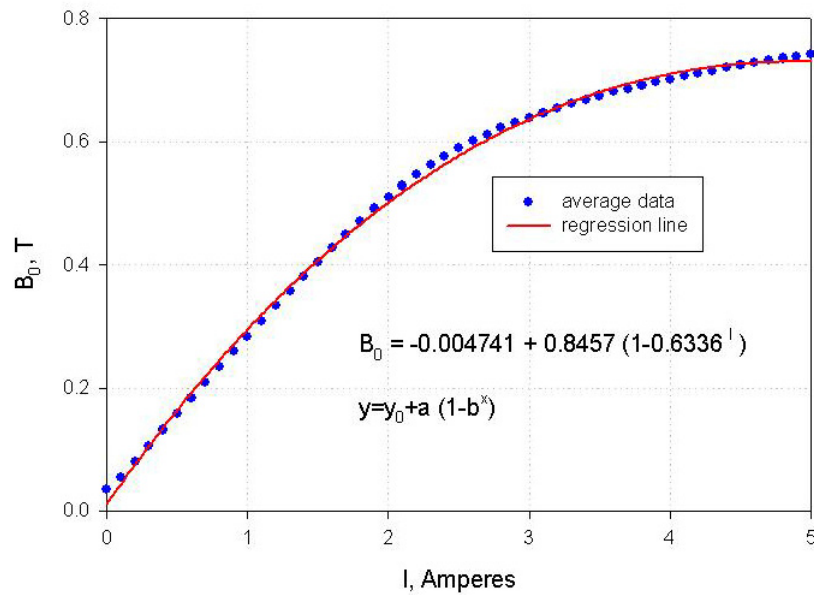


Figure 4.18. Average values for the four coils of B versus I for the range of current (5.0-0.0) A. The points were interpolated using equation (4.25).

The points obtained from the measurements, shown in Figure 4.18, were interpolated using the exponential equation

$$y = y_0 + a(1 - b^x) \tag{4.25}$$

where y corresponds to the B_0 value and x is the value of current I . By substituting the values for the parameters, a , b , and y_0 we obtain

$$B_0 = -0.004741 + 0.8457(1 - 0.6336^I) \tag{4.26}$$

Rearranging equation (4.26) we obtain an equation for I in terms of B_0

$$I = 2.1914 \ln \left(\frac{0.8457}{0.8409 - B_0} \right) \tag{4.27}$$

As already mentioned, for each value of initial current from which the decay starts we obtain a different minor hysteresis curve. An example is shown in Figure 4.19 where the red curve represents the curve used for the decay starting at 0.25 A.

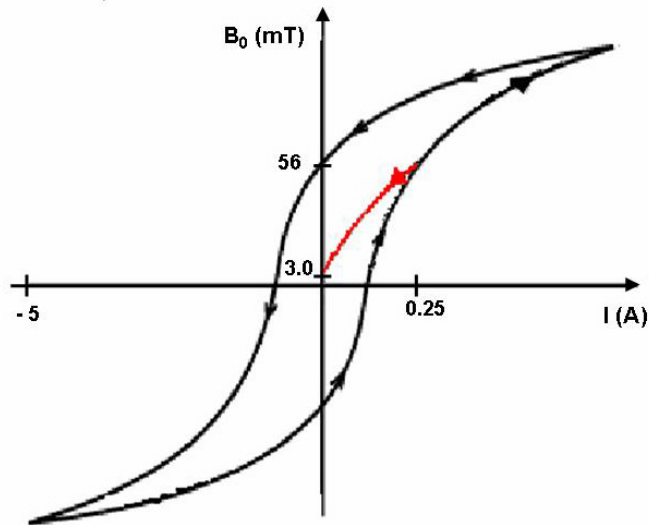


Figure 4.19. Hysteresis loop. The minor hysteresis curve used for the experiments starting at 0.25 A is shown in red color. The corresponding value of magnetic field is ~ 56 mT and the remnant field value is ~ 3.0 mT.

The curve was obtained by plotting small decrements of current I , provided by the power supply, versus the corresponding magnetic field measured inside the quadrupole with the Gaussmeter. A software program, developed by Dr. Yang Zhao from the Chemical Engineering Department at Ohio State University, was used for the computer control of the power supply.

Table IV shows the values of the equation parameters for the different ranges of current used for the MgFFF experiments.

Table IV. Equation parameters for different ranges of current.

Range of current I	Equation parameter (a)	Equation parameter (b)	Equation parameter (y_0)
5.0-0.0	0.8457	0.6336	$- 4.741 \cdot 10^{-3}$
1.0-0.0	0.5076	0.5820	$2.175 \cdot 10^{-2}$
0.5-0.0	0.2312	0.3388	$1.028 \cdot 10^{-2}$
0.35-0.0	0.1520	0.2144	$5.370 \cdot 10^{-3}$
0.3-0.0	0.1150	0.1527	$5.725 \cdot 10^{-3}$
0.25-0.0	0.1632	0.2988	$2.761 \cdot 10^{-3}$
0.2-0.0	0.2417	0.4381	$-1.727 \cdot 10^{-3}$
0.15-0.0	0.2093	0.4359	$- 8.0 \cdot 10^{-4}$
0.1-0.0	1.0310	0.8362	$-5.157 \cdot 10^{-3}$

During an MgFFF analysis the Gaussmeter probe is placed in between two pole pieces because of the channel occupying the annular space within the quadrupole. A further correction was required to obtain the field strength at the pole tips. Figure 4.20 shows the relationship between the field measured at pole tip 2 and the field measured between poles 2-3.

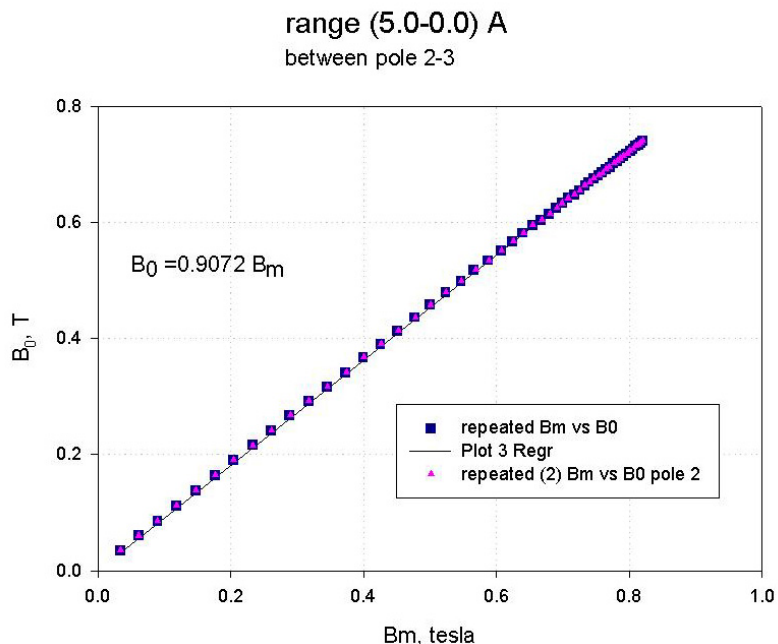


Figure 4.20. Relationship between the field measured at pole tip 2 and the field measured between poles 2-3

4.4 MgFFF Instrumentation set-up

Instrumentation set-up

HPLC pump: Dionex GP40 Gradient Pump (Dionex Corporation, Sunnyvale, CA).

Injection valve: 7725i Rheodyne injection valve (Rheodyne, Cotati, CA) with a 20 μ l injection loop.

Separation device: Helical channel of 500 μ m thickness (machined by the Cleveland Clinic Prototype Laboratory). The 250 μ m thick channel was machined by Criterion Tool & Dye, Inc., Cleveland, OH.

Quadrupole electromagnet: made of four copper coils (wound by CWS Coil Winding Specialist, Santa Ana, CA), and four pole pieces (machined by the Cleveland Clinic Prototype Laboratory).

Teslameter: (Model 6010 Gauss/Tesla Meter, SYPRIS, Test and Measurements, F.W. Bell, Orlando, FL).

Power supply: Xantrex HPD60-5 Series Programmable Power Supply, Xantrex Technology Inc., Burnaby, British Columbia, Canada.

Permanent quadrupole magnets generating fields of 0.071 T and 1.42 T (description in figures 4.2 and 4.3)

Syringe: 100 μ l, Series A-2 Pressure-Lok^R, VICI Precision Sampling Inc.

4-way diagonal flow switching valve (for elution and stop-flow mode of operation):

Model V101D, Upchurch Scientific, Inc.

Backpressure regulator: 75psi cartridge, model P786, Upchurch Scientific, Inc.

UV-detector: Model VUV-12 UV-detector, HyperQuan Inc., Colorado Springs, CO.

Computer: PC Pentium V, Dell Inc.

Acquisition software: Windaq Lite software, Dataq Instruments.

Interface: 12-bit analog-to-digital converter, DI-154RS, Dataq Instruments, Akron, OH.

Connection tubing: yellow PEEK Tubing, 1/16" OD, 0.007" ID and orange PEEK

Tubing, 1/16" OD, 0.020" ID, Upchurch Scientific, Inc.; natural FEP Tubing, 1/16" OD, 1/32" ID, Zeus Inc., Orangeburg, SC.

The general steps for the analysis of a sample using the magnetic FFF system are described below.

4.5 Mobile phase properties and preparation

The viscosity of the carrier liquid (mobile phase) should be low enough that particles can be relaxed at the channel inlet in a reasonable length of time. The particles should not degrade in the carrier liquid; water containing a small amount of appropriate

surfactant is usually employed for most particles. In the case of analysis of biological samples it is important to use a biocompatible mobile phase to maintain sample integrity.

Distilled and deionized water is recommended for the preparation of aqueous carrier liquids. They are usually filtered through a 0.22 μm filter. Degassing the carrier is recommended, particularly for normal-mode experiments where flow rates are <2.0 ml/min. Vacuum system was used to perform the carrier liquid degassing.

4.6 Sample preparation

Critical to a meaningful magnetic FFF analysis is access to single particle suspensions. The particulate samples must be well dispersed and it is essential that the particles do not undergo aggregation. If possible, samples should be prepared in the same liquid as the carrier liquid. Solid particles (such as powders) should be deagglomerated to achieve an evenly dispersed suspension. Surfactants in aqueous media facilitate wetting the surface of the particles and also stabilize the dispersions. Mechanical means, such as vortexing and sonication, are employed to disperse agglomerated particles. Particles such as biological cells require buffered media of relatively high ionic strength. Only carrier liquids with appropriate pH, ionic strength and osmolality maintain the structural integrity, activity and function of these samples during and after the separation. The analyzed samples are usually stored in the refrigerator at 4 $^{\circ}\text{C}$ to avoid degradation over time.

4.7 Experimental procedure

1. Set the pump at the preferred flow rate (e.g. 0.5 ml/min, 1.0 ml/min).
2. Set the detector range (e.g. 0.05)

3. Create and name the data acquisition file that monitors the output of the detector and teslameter.
4. Sample preparation (see paragraph 4.6). The sample might be diluted if necessary using the carrier solution to a volume of 20 μl .
5. Introduce the sample into the sample loop of the injection valve (through a 100 μl syringe) keeping the valve in “load” position.
6. Transfer the sample from the injection valve to the head of the channel by turning the valve into the “inject” position. The time necessary to transfer the whole sample into the channel is called the injection time (t_{inj}). During this step it is preferred to operate at lower flow rates (0.1 ml/min) than those used for the elution of the sample so to have longer t_{inj} easier to measure (e.g. 2 minutes at 0.1 ml/min). Schematic shown in Figure 4.21
7. Stop flow procedure. The flow is stopped inside the channel and redirected to the waste using the 4-way diagonal flow switching valve. Schematic shown in Figure 4.22. During this so-called stop flow relaxation the particles, under the influence of the magnetic field, approach their steady state distributions close to the accumulation wall prior to elution. The stop flow time can be calculated for the steric/hyperlayer mode of elution following equation

$$t_{relax} = \frac{w}{u_m} \quad (4.28)$$

where w is the channel thickness and u_m is the magnetophoretic velocity of the particle. For normal mode analyses, this calculated time is doubled in order to allow for the establishment of the steady state distribution.

8. Elution. A few minutes before the end of the stop-flow time, the flow rate is increased to the value chosen for the elution of the sample. Schematic shown in Figure 4.21. At the end of the stop-flow time switch the 4-way valve so as to restore the flow through the channel. At the same time start the data recording in the acquisition file. Keep recording the data until the sample is eluted and the signal decreases to a stable value that approaches the baseline. Then take the channel out from the quadrupole magnet (to obtain zero field) and mark the baseline at this time point. Continue to record data for any material released from the channel at zero field.
9. Cleaning procedure. Clean the sample loop by injection of distilled water, then ethanol and distilled water again in order to completely remove any remaining impurities or particles. Clean the channel and the whole system by flowing distilled water at high flow rates (e.g. 4.0 ml/min). When using biological samples, clean the sample loop with a solution of water and bleach and then wash with distilled water.
10. When operating with a variable magnetic field (e.g. quadrupole electromagnet): after step 5, set the current of the power supply, using the computer software, at the required initial level. Choose the field decay program from the available program library that is suitable for the elution of the sample. Position the teslameter probe between the pole pieces of the electromagnet in order to monitor the magnetic field strength during the analysis. Start the field control program and then follow the procedure from step 6.

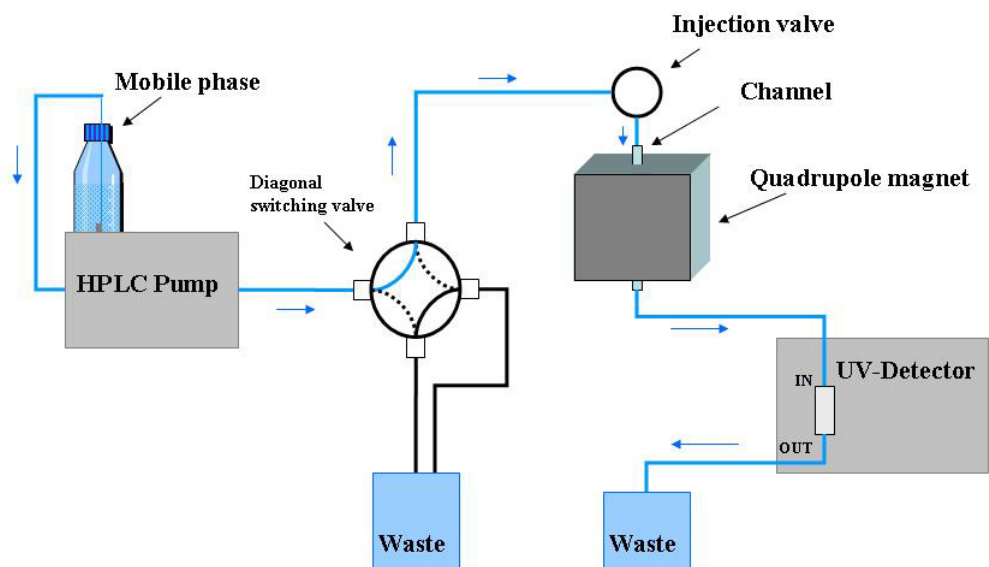


Figure 4.21. Schematic of the MgFFF system during the sample loading and elution operating mode. The carrier fluid goes from the pump through the separation channel and to the detector via the diagonal switching valve.

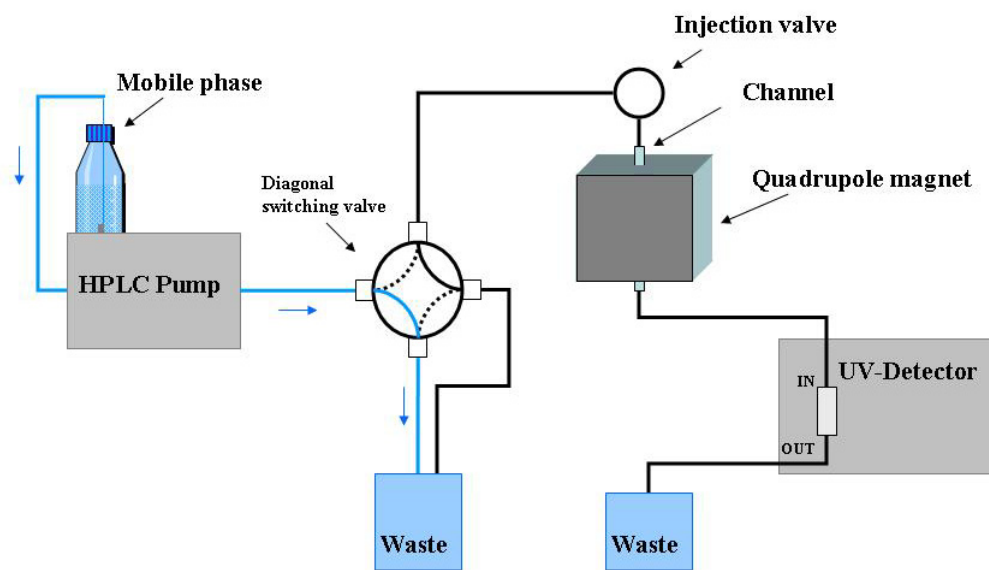


Figure 4.22. Schematic of the MgFFF system during the stop-flow operating mode. The carrier fluid is directed from the pump to the waste via the diagonal switching valve. In this case the flow into the system is stopped and the sample injected into the channel is allowed to relax.

CHAPTER V

PRELIMINARY STUDIES

Preliminary studies were carried out using permanent quadrupole magnets generating constant magnetic fields. The particles tested were magnetic microspheres and red blood cells.

5.1 Steric/hyperlayer fractionation of polystyrene/magnetite microspheres by MgFFF

Magnetic polystyrene microspheres produced in the laboratory of Professor Shlomo Margel (Department of Chemistry, Bar-Ilan University, Ramat Gan, Israel) were used in a proof of principle experiment for our development of Quadrupole Magnetic Field-Flow Fractionation. These organic-inorganic hybrid particles, composed of cores of monodisperse polystyrene microspheres and shells of magnetite (Fe_3O_4) and silica (each 30-40 nm thick), have been synthesized by seeded polymerization of iron salts and $\text{Si}(\text{OEt})_4$ onto the core particles [86]. The outer silica coating stabilizes the magnetite and protects it from oxidation. SEM images of similar but smaller microspheres (2.7 μm diameter) at three stages of their synthesis are shown in figure 5.2. The diameter of the

microspheres was measured by Scanning Electron Microscopy (SEM; model JSM-840, Jeol Ltd., Akashima, Japan). Three particle samples (MMC2, MMC3, and MMC4) having the same nominal diameter of 5.5 μm , but differing in their magnetite content, were used in this study. Their size distribution was calculated using an electrical sensing zone particle analyzer (Coulter Multisizer Z-2, Beckman, Inc., Fullerton, CA), as shown in figure 5.1. Data (not shown) obtained from SEM and Coulter Multisizer analysis demonstrate that the addition of the magnetite and silica coatings have no measurable impact on the microspheres' diameters. The polystyrene/magnetite microspheres were supplied as dry material and were subsequently suspended in 0.1 % FL-70 detergent (from Fisher Scientific) for analysis.

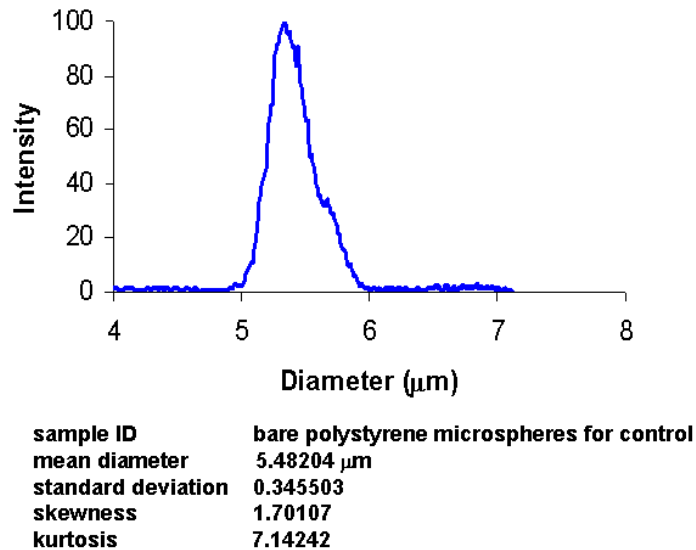


Figure 5.1. Size distribution data of bare polystyrene microspheres obtained using Coulter Multisizer Z-2.

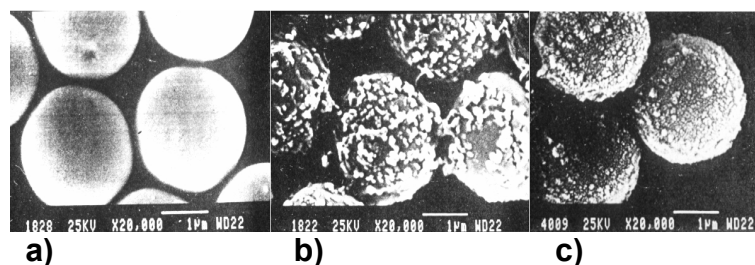


Figure 5.2. SEM images of a) bare monodisperse polystyrene (PS) microspheres; b) PS microspheres with magnetite coating; c) PS microspheres with magnetite and silica coating. The final diameter of the microspheres is $2.7 \pm 0.04 \mu\text{m}$.

As shown in figure 5.3, Cell Tracking Velocimetry (CTV) measurements of sample MMC4, MMC3, and MMC2 indicated mean magnetophoretic mobilities of 3.50×10^{-5} , 8.84×10^{-5} and $4.76 \times 10^{-4} \text{ mm}^3/\text{TAs}$, respectively, at a mean field strength of 1.40 T. These CTV measurements of the samples were carried out by Lee Moore from the Biomedical Engineering Department at the Cleveland Clinic. More details about CTV are reported in section 3.1.5. At this field strength, the magnetite present in the particles is magnetically saturated, since this material approaches magnetic saturation between 0.1 and 0.2 T. A relatively weak quadrupole magnet generating only 0.071 T at the outer channel wall was used for the MgFFF studies. At this field strength, the particles behave as unsaturated magnetic dipoles. The channel employed for these experiments was the $500 \mu\text{m}$ thick. The carrier fluid was made of an aqueous solution of FL-70 0.1%. The field was found to be sufficient to bring about selective elution of the particles. The relative magnitude of the magnetophoretic mobilities at 1.40 T may be expected to correspond to the relative magnitude of the magnetic force on the particles at 0.071 T. It was found that the lower mobility particles eluted as a Gaussian shaped peak at a flow rate of 0.9 ml/min. At this flow rate the higher mobility particles were very strongly retained, however. This, in itself, indicates the selective retention, but the objective is to

elute the particles with elution times being some function of magnetic moment or magnetite content. At the fixed field strength of 0.071 T that was available, the dependence of the hydrodynamic lift force [87], [88], [89], [90] on fluid shear rate could be exploited in order to vary the degree of particle retention. In fact, the more strongly magnetized particles were indeed found to elute at higher retention ratio at elevated flow rates. The speed of elution increased much more rapidly than the flow rate itself, as predicted by the balanced-force elution mechanism [91], [92], [93]. A complete separation of a mixture of the three particle samples was obtained using a stop flow time of 20 minutes and a step-programmed increase of flow rate with time, as shown in figure 5.4. The initial flow rate of 0.9 ml/min was held constant for 20 min to elute the first component. The flow rate was then increased to 2.0 ml/min and held constant for 10 min to elute the second component. The flow rate was then stepped at increments of 1.0 ml/min every 15 seconds up to a maximum of 10 ml/min, and during this period the final peak was eluted. The first peak is a “void peak”, and corresponds to the elution of the medium in which the sample mixture was suspended when introduced. This is almost invariably observed in FFF separations, and it indicates the time for the elution of non-retained materials. The second peak corresponds to the lower mobility sample (MMC4), the third to the intermediate mobility sample (MMC3), and the fourth to the highest mobility sample (MMC2). The resolution may be compared to the distribution in their mobility obtained by CTV. The elution of the more magnetic particles was hastened by increasing flow rate, which has the effect of increasing hydrodynamic lift forces. Elution velocity does not therefore increase in direct proportion to flow velocity. In fact, the more magnetic particles were found not to elute at the lowest flow rate (0.90 ml/min). The

component peaks were confirmed by the injection of the individual particles under the same flow programmed conditions. A programmed reduction in field strength would have been the more desirable option but the use of a permanent magnet quadrupole assembly precluded programming of field decay. A blank run was also carried out to confirm the flat baseline response during the period of programmed flow rate.

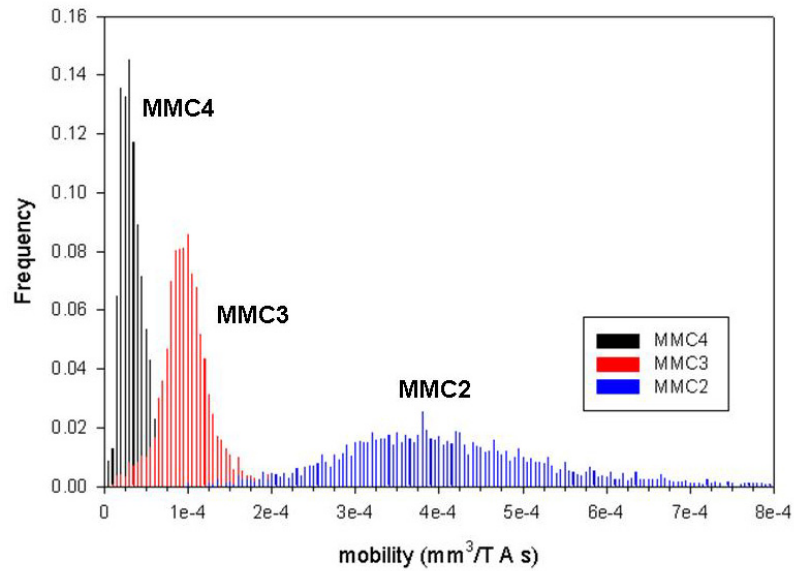


Figure 5.3. Composite magnetophoretic mobility histogram of the three size-monodisperse magnetic microspheres (MMC4, MMC3, MMC2) measured by Cell Tracking Velocimetry (CTV).

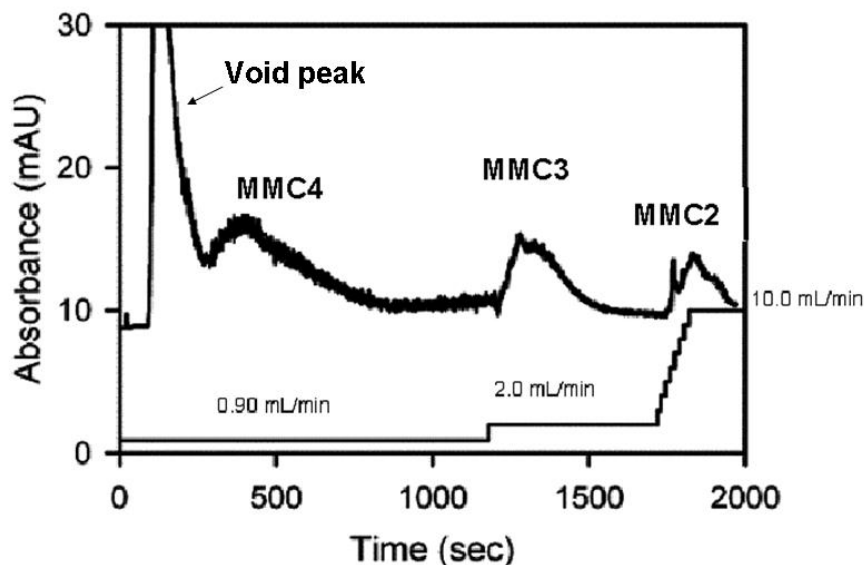


Figure 5.4. MgFFF elution profile of a mixture of three samples of magnetic microspheres (MMC4, MMC3, MMC2) having different magnetophoretic mobility. The fractionation is obtained by applying an increase in carrier flow rate with time (from 0.9 ml/min to 10 ml/min) at a constant magnetic field strength of 0.071 Tesla.

5.2 Magnetic Field-Flow Fractionation of erythrocytes

The literature contains many reports of Gravitational Field-Flow Fractionation (GrFFF) of Red Blood Cells (RBCs) [94], [95]. This is the simplest form of FFF in which the migration of the sample cells to one of the channel walls is due to their sedimentation under the Earth's gravitational field. This suggests that both deoxygenated RBCs and RBCs containing methemoglobin may be fractionated using quadrupole magnetic FFF. Methemoglobin is formed by the oxidation of hemoglobin (Hb) iron from the ferrous (Fe^{2+}) to the ferric (Fe^{3+}) state, thereby rendering the hemic iron unable to bind oxygen [96].

Early studies on the magnetic susceptibility of hemoglobin have helped to elucidate the molecular and electronic structure of the chemical bonds in the heme group, depending on the oxidative state and oxygen binding of the iron atom. Early work by

Pauling, Coryell and others indicated that there is a profound change in the character of chemical bonds between the iron atom and the rest of the heme group and the globin chain as a result of oxygen binding [97]. There are ionic bonds between the Fe^{3+} present in the methemoglobin (the oxidized form of hemoglobin), and the protoporphyrin group and the globin chain [96]. Each time the iron is attached to the surrounding protoporphyrin and histidine side chain by ionic bonds, the presence of unpaired electrons is noted. As a consequence, methemoglobin contains five unpaired electrons per heme group, making this species paramagnetic. Due to its covalent bonds, oxyhemoglobin has no unpaired electrons and is diamagnetic.

The calculations below suggest that MgFFF can indeed be used to separate RBCs based on the magnetic properties of the hemoglobin in the cells. Oxygenated RBCs, being relatively unaffected by the magnetic field, are not driven close to a channel wall, and are flushed very quickly from the channel. Figure 5.5 shows CTV measurements for oxygenated and methemoglobinated RBCs [98].

The forces on a RBC due to gravity and due to the magnetic field may be calculated as follows. The magnetic forces are based on the magnetophoretic mobilities measured by CTV.

Force Due to Gravity.

This is calculated by the equation

$$F_g = V \Delta\rho G \tag{5.1}$$

where V is the RBC volume, $\Delta\rho$ is the density difference between the RBC and the suspending medium, and G is the gravitational acceleration. Substituting in estimates for these quantities:

$$F_g = (88.4 \times 10^{-18} \text{ m}^3)(95 \text{ kg/m}^3)(9.81 \text{ m/s}) = 8.24 \times 10^{-14} \text{ N} \quad (5.2)$$

The migration velocity under gravity, the sedimentation velocity, is given by

$$u_g = \frac{F_g}{f} = \frac{F_g}{6\pi\eta R_h} \quad (5.3)$$

where f is the friction coefficient, η is the fluid viscosity, and R_h is the hydrodynamic radius of the RBC. Substituting in estimated values for aqueous suspension, we obtain

$$u_g = \frac{8.24 \times 10^{-14} \text{ N}}{6\pi(0.00096 \text{ kg/ms})(3.85 \times 10^{-6} \text{ m})} = 1.2 \times 10^{-6} \text{ m/s} = 1.2 \text{ } \mu\text{m/s} \quad (5.4)$$

Magnetic Force on Methemoglobinated RBC. We now make use of the magnetophoretic mobility measurements by CTV to first calculate the magnetophoretic velocity in the field of the larger permanent quadrupole magnet that was available, and hence obtain the force on the cell. The magnetophoretic velocity is given by

$$u_m = mS_m = m\nabla\left(\frac{B^2}{2\mu_0}\right) \quad (5.5)$$

where m is the magnetophoretic mobility, S_m is a measure of the magnetic force field strength (magnetic energy gradient), B is the magnetic induction, and μ_0 is the magnetic permeability of free space. In the quadrupole magnetic field, next to the channel outer wall,

$$S_m = \frac{B_o^2}{\mu_0 r_o} \quad (5.6)$$

where B_o is the magnetic induction at the outer channel wall, and r_o is the radius of the outer channel wall. Mobility data were obtained by [98]. Substituting in values for the current system, we obtain

$$u_m = (3.66 \times 10^{-15} \text{ m}^3/\text{TAs}) \frac{(1.32 \text{ T})^2}{(4\pi \times 10^{-7} \text{ Tm/A})(0.00743 \text{ m})} = 0.68 \mu\text{m/s} \quad (5.7)$$

The force on the RBC is then given by

$$F_m = f u_m = 6\pi(0.00096 \text{ kg/ms})(3.85 \times 10^{-6} \text{ m})(6.8 \times 10^{-7} \text{ m/s}) = 4.8 \times 10^{-14} \text{ N} \quad (5.8)$$

Magnetic Force on Deoxygenated RBC. Carrying out the same calculations for a deoxygenated RBC,

$$u_m = (3.86 \times 10^{-15} \text{ m}^3/\text{TAs}) \frac{(1.32 \text{ T})^2}{(4\pi \times 10^{-7} \text{ Tm/A})(0.00743 \text{ m})} = 0.72 \mu\text{m/s} \quad (5.9)$$

$$F_m = f u_m = 6\pi(0.00096 \text{ kg/ms})(3.85 \times 10^{-6} \text{ m})(7.2 \times 10^{-7} \text{ m/s}) = 5.0 \times 10^{-14} \text{ N} \quad (5.10)$$

Magnetic Force on Oxygenated RBC. The magnetophoretic velocity and force on an oxygenated RBC are very much smaller.

$$u_m = (-0.2 \times 10^{-15} \text{ m}^3/\text{TAs}) \frac{(1.32 \text{ T})^2}{(4\pi \times 10^{-7} \text{ Tm/A})(0.00743 \text{ m})} = -0.037 \mu\text{m/s} \quad (5.11)$$

$$F_m = f u_m = 6\pi(0.00096 \text{ kg/ms})(3.85 \times 10^{-6} \text{ m})(-3.7 \times 10^{-8} \text{ m/s}) = -2.6 \times 10^{-15} \text{ N} \quad (5.12)$$

Note that the oxygenated RBC has a lower magnetic susceptibility than the aqueous suspending medium and the cell moves in the direction of lower magnetic field.

The fact that the magnetic force on an oxidized RBC (containing methemoglobin) was of the same order of magnitude as the buoyant force due to gravity suggested that magnetic FFF should be able to distinguish between oxidized and oxygenated RBCs. This prediction was confirmed by experiment, as shown in figure 5.6.

5.2.1 Method of operation

The blood samples were provided by Dr. Graciela Ostera from the Laboratory of Chemical Biology, National Institute of Diabetes and Digestive and Kidney Diseases, NIH. The blood was collected at the NIH under an Institutional Review Board-approved

protocol for blood collection from normal volunteers for research purposes. The samples were drawn in Ethylenediaminetetraacetic acid (EDTA). The oxidative treatment (for the methemoglobinated RBCs) was performed by mixing whole blood with 5mM sodium nitrite solution. After incubation, oxidant treated erythrocytes were washed with PBS and resuspended in PBS.

For the oxygenated RBC the sample was allowed to fully oxygenate by gentle rocking at room temperature for at least one hour. The samples were stored in the refrigerator at 4 °C. They were gently shaken and then diluted with PBS to the preferred concentration before each analysis.

MgFFF experimental parameters

Elution flow rate: 2.0 ml/min

Injection Time: 2 min

Injection Flow rate: 0.1 ml/min

Stop flow time: 20 min for the methemoglobinated RBCs and 50 min for the oxygenated RBCs.

Magnetic field: 1.42 T

Injected concentration: $<10^6$ cells/20 μ l

Method

A small volume (20 μ l) of cell suspension is introduced to the channel inlet through the injection valve. The fluid flow is interrupted for a period of time to allow the suspended cells to migrate under the influence of the magnetic field to the outer channel wall. This is known as stop-flow relaxation. The fluid flow is then resumed. During elution the cells do not remain in contact with the channel wall but are lifted away from

the wall by hydrodynamic effects. These effects can be described in terms of a hydrodynamic lift force that has been found to be a function of particle size, fluid shear rate near the wall, fluid viscosity, and the deformability of the cell.

We can calculate the theoretical required time for the methemoglobin RBCs to migrate to the channel wall when the flow is interrupted (so-called stop-flow procedure).

$$t_{relax} = \frac{w}{u_m} = \frac{5 \times 10^{-4} \text{ m}}{6.8 \times 10^{-7} \text{ m/s}} = \sim 12 \text{ min} \quad (5.13)$$

where w is the channel thickness and u_m is the magnetophoretic velocity of the RBCs, calculated in equation (5.7).

The methemoglobinated cells would therefore require approximately 12 minutes for the relaxation process. In this period, oxygenated cells would migrate only about 27 μm in the opposite direction, toward the inner channel wall. This means that oxygenated RBCs would not experience significant relaxation. Those that do migrate to the wall would be driven away by hydrodynamic lift on the resumption of flow. These studies showed the feasibility of the analysis of biological samples, such as RBCs, by MgFFF.

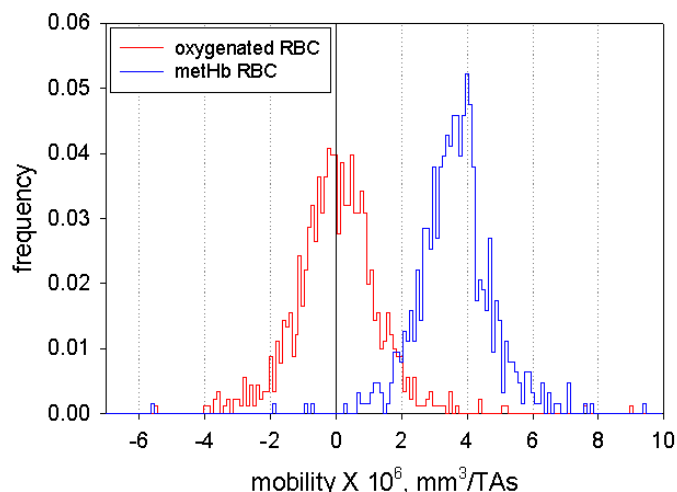


Figure 5.5. Magnetophoretic mobility histograms of oxygenated and methemoglobinated RBCs. Note the higher mobility values for the methemoglobin-rich RBCs compared to the oxygenated RBCs.

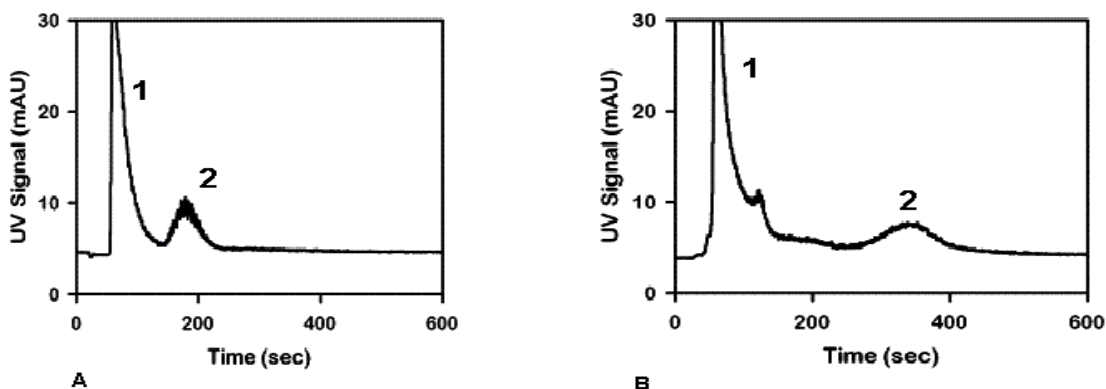


Figure 5.6. Steric/hyperlayer mode of elution of erythrocytes by MgFFF. The first peak in each fractogram corresponds to the void time (defined as the time that non-retained species spend in the system); the second peak corresponds to the eluted cell sample. Sample volume: 20 μl ; sample concentration $<10^6$ cells/20 μl ; elution flow rate 2.0 ml/min; stop flow time: 50 min in A and 20 min in B. A. Oxygenated erythrocytes. B. Methemoglobin-rich erythrocytes. Note the shift to longer retention time of the eluted sample peak 2 in B relative to A, indicating retention of the methemoglobin-rich erythrocytes in the magnetic field.

CHAPTER VI

DEVELOPMENT OF PROGRAMMED FIELD

6.1 Introduction

Programming the intensity of the field in FFF can provide control of resolution, extension of the range of applicability (particularly for samples with broad distribution of size, or molecular weights), and improved detection capability. J. C. Giddings proposed in his first paper on FFF the concept of programming FFF analysis [1]. Subsequently many mathematical forms for the time-based changes in field strength were proposed [99], [100]. Parabolic, step, and exponential mathematical functions for field programming were proposed and further developed [101], [102], [103], [104], [105], [106], [107], [108], [109], [110]. For the normal mode of elution it is possible to obtain size distributions without the use of any calibration standards (and this is important for the case of magnetic nanoparticles as calibration standards are unavailable) because of the theoretical relationship between the retention time t_r and the particle size [111].

6.2 Power programmed field decay

The field decay program used for our experiments corresponds to the power program developed by P. S. Williams [105] and is described by

$$B(t) = B(0) \left(\frac{t_1 - t_a}{t - t_a} \right)^p, \text{ for } t \geq t_1 \quad (6.1)$$

where $B(t)$ is the field strength at time t , $B(0)$ is the initial field strength which is held constant for an initial time t_1 (also called predecay time), t_a is a second time constant that is generally set to $-pt_1$, and p is a positive real number. If we want to over-ride the specific predecay time with some other predecay time t_p which can be less or greater than t_1 , the decay function is given by

$$B = B(0) \left(\frac{t_1 - t_a}{t - t_a + (t_1 - t_p)} \right)^p, \text{ for } t \geq t_p \quad (6.2)$$

This has the result of displacing the field decay curve along the time axis by $t_1 - t_p$ without changing its shape. The field strength B refers to the field strength at the accumulation wall B_0 where the particles are concentrated. The gradient in field strength, equal to B_0/r_0 , decays in parallel with B_0 . The field decay curve corresponding to equation (6.1) is shown by the full line in Figure 6.1.

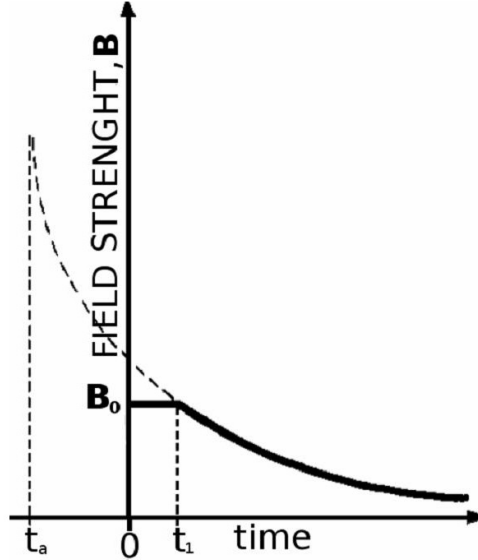


Figure 6.1. Field-decay curve for power programming.

Requirements for equation (6.1) to be meaningful are that $t \geq t_1 > t_a$ and $p > 0$. $B(t)$ approaches infinity as time t is extrapolated back to t_a . As shown in figure 6.1, t_a corresponds to the position on the time axis of the asymptote of $B(t)$ as it approaches infinite values. The field strength decays inversely with time, measured from t_a , raised to the power of p . The parameter t_a may be positive, negative, or zero, but it is necessary that $t_1 > t_a$ for the program to be meaningful.

Retention time t_r in programmed FFF is given as the upper limit of the integral in the general equation

$$L = \int_0^{t_r} R \langle v \rangle dt \quad (6.3)$$

where L is the channel length, R is the retention ratio, and $\langle v \rangle$ is the mean fluid velocity.

In general, in field programmed FFF, R varies with the field strength B but $\langle v \rangle$ is held constant. R depends also on particle diameter, leading to different t_r values for different particles. We obtain

$$\frac{L}{\langle v \rangle} = t^0 = \int_0^{t_r} R dt \quad (6.4)$$

where t^0 is the elution time of a nonretained peak.

6.3 Data analysis for the determination of size distributions

As the field and the field gradient decay, the force on the eluting particles F_m falls and the retention parameter λ and, therefore, the retention ratio R increase (see equations 1.8 and 1.15). Any arbitrary field gradient decay may be accounted for in relating a retention time to the volume of magnetic material per particle by numerically solving the integral equation 6.4. The solution of equation 6.4 is obtained by writing it as

$$\int_0^{t_r} R(B(t), d) dt - t^0 = F(t_r, d) = 0 \quad (6.5)$$

where $R(B(t), d)$ shows the dependence of R on field strength B , and particle diameter d .

A data analysis algorithm [112] was used for the solution of equation (6.5). The algorithm works over any interval of d for which $F(t_r, d) = 0$ describes a one-to-one relationship between d and t_r . This excludes samples which elute in both normal and steric modes (i.e. samples which are extend beyond the steric inversion point) [113]. The approach considers a set of discrete values of d (in our case, equivalent spherical diameters for particle magnetic core) and numerically calculates the expected retention times using the monitored field strength during the analysis (field and detector response are recorded at discrete times during the analysis). Particle diameters are then associated with discrete retention times by interpolation.

6.4 Required settings for the field-decay during MgFFF experiments

As already mentioned in Chapter IV, field decays starting at a different value of initial current follow different minor hysteresis curves. Thus for each range of current a different equation is defined. Equation (6.1) and equation (4.25) were combined in an ExcelTM worksheet (Microsoft Corp., Redwood, CA) that was created in order to calculate the values of the required magnetic field B as function of time and then the values of required current I as function of time. The parameters for equation (6.1) were chosen in order to have the desired field decay. The table of required current for discrete time intervals was used in the software for the control of the power supply. Figure 6.2 shows the current decays over time relative to different program parameters. The corresponding field decays are shown in Figure 6.3. Note how choosing a certain value of p and t_1 changes the shape of the field decay. The values of the power program parameters were chosen in order to have the field decaying over a broad range of time. This allowed for the elution of particles broadly polydisperse in their magnetite content.

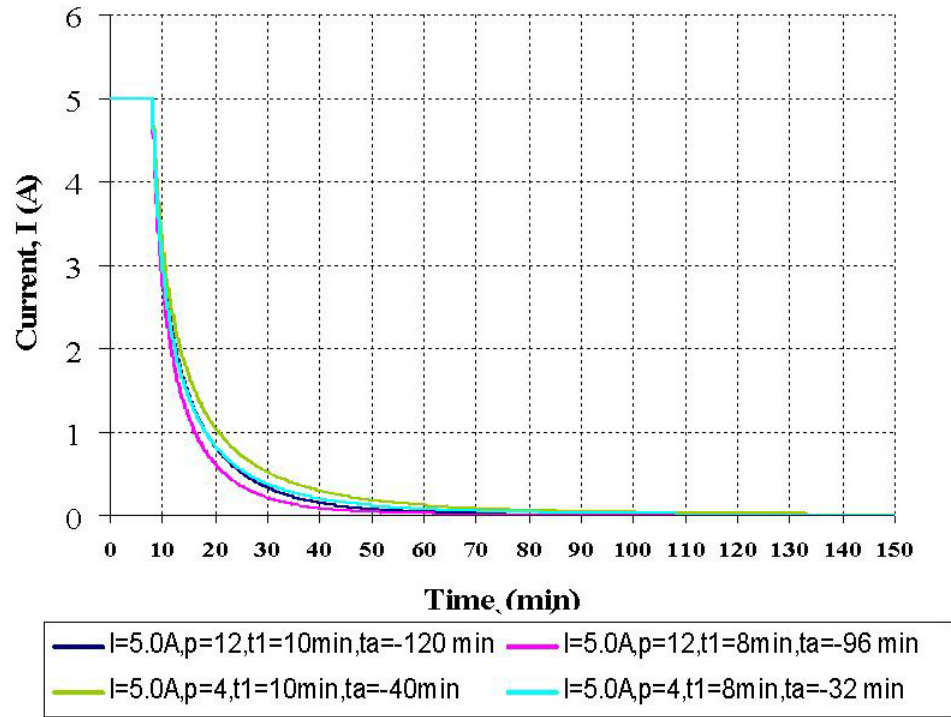


Figure 6.2. Calculated current decays over time relative to different program parameters.

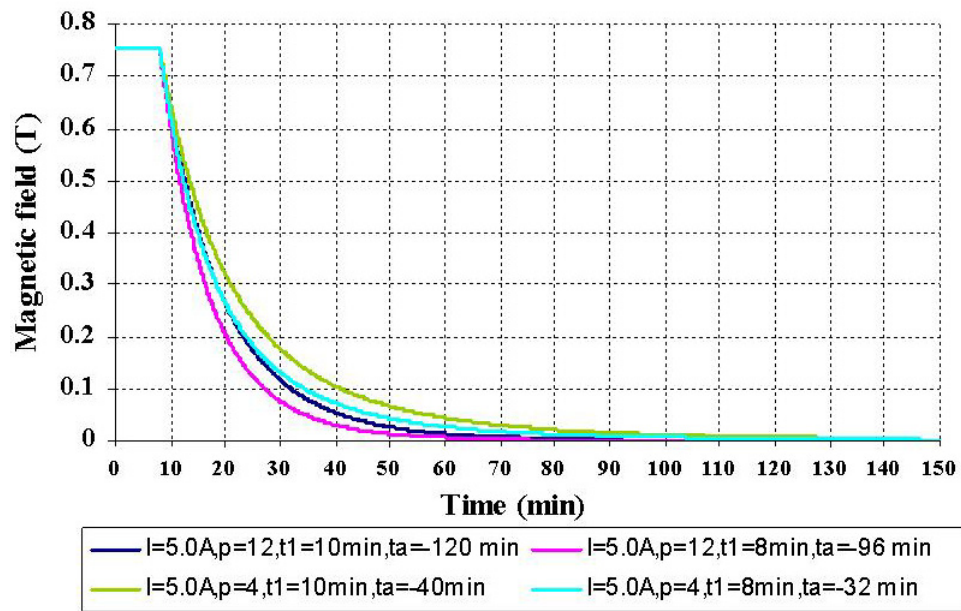


Figure 6.3. Theoretical values of field decays obtained using the same initial current of 5 A held constant for 8 minutes. Note how the shape of the decays over time changes with the changing of the program parameters t_1 , t_a , and p .

CHAPTER VII

RESULTS AND CONCLUSIONS

In this last Chapter we are going to discuss the latest achievements of MgFFF for the analysis of magnetic nanoparticles. In these studies a programmed magnetic field decay was used for the elution of broadly polydispersed samples. The data obtained from the elution profiles were used for the calculations of the distribution in particle magnetic core diameter. The samples of magnetic nanoparticles that were tested were provided by three different suppliers.

7.1 Magnetic Field-Flow Fractionation of dextran coated magnetite nanoparticles

Samples of magnetic nanoparticles (lot 5, 40-43, 50-56, 78, 80, and 83) were supplied by BD Biosciences Pharmingen. They had been procured from Skold Technology for preparation of their commercial line of Imag products [114]. The particles are composed of dextran-coated magnetite and have nominal size range of $230\text{nm} \pm 150\text{ nm}$ (information provided by the company). They were supplied in suspension in 10 mM MES (2-(N-morpholino)ethanesulphonic acid) buffer at pH 6.1,

and were not conjugated with any antibodies or any other surface functional groups. SEM and quasi-elastic light scattering (QELS) measurements were carried out on sample 80. SEM images are shown in figure 7.1. QELS measurements were obtained using a Brookhaven Instruments system (Model BI-200SM, Brookhaven Instruments Corp., Holtsville, NY, USA). This yielded a mean diameter of 178 nm and relative variance of 0.198 (corresponding to a relative standard deviation of 44.5%), assuming a log normal distribution. The data are shown in Figure 7.2.

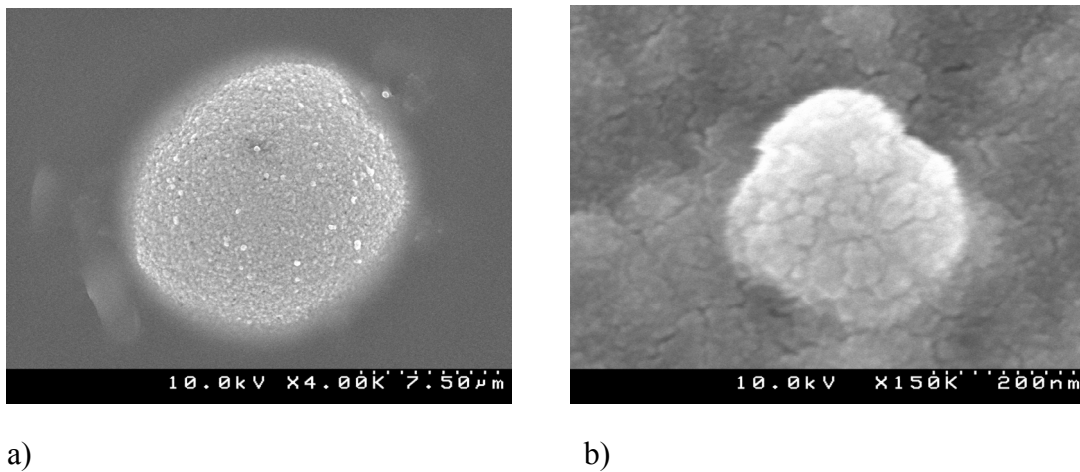
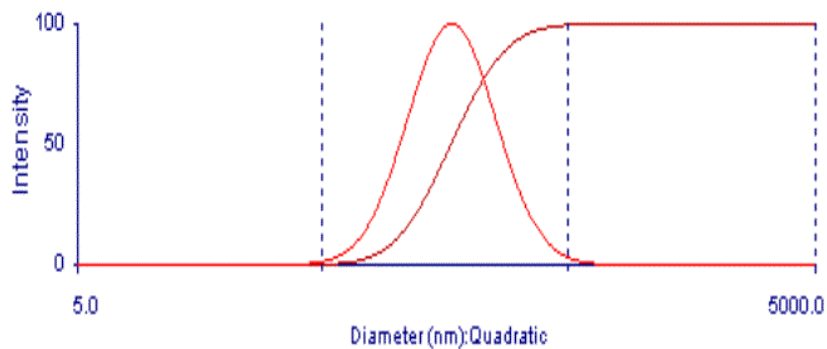


Figure 7.1. SEM images of nanoparticles from lot 80. a) Image of a cluster of nanoparticles. They probably aggregated during drying for SEM sample preparation. b) Image of a single nanoparticle of about 200 nm diameter. Courtesy of Anna Dubnisheva, Dept. of Biomedical Engineering, Cleveland Clinic.



Sample ID	lot 80 of dextran coated magnetic nanoparticles
Elapsed time	00:02:00
Mean diameter	178.1 (nm)
Relative variance	0.198
Skweness	0.867
Rms. Error	1.0552e-03

Figure 7.2. Size distribution data of dextran coated magnetite nanoparticles (lot80) obtained by quasi-elastic light scattering analysis. Measurements carried out by Weiwei Hu of the Department of Chemical and Biomolecular Engineering at Ohio State University.

MgFFF elution profiles of sample 80 were obtained by employing the 250 μm thick channel and by applying different, constant magnetic field strengths. The elution profiles are shown in Figure 7.3. No satisfactory particle elution was obtained for any of the four different field strengths tested. At the highest field (53 mT, Figure 7.3a) the entire sample was retained in the column and the sample was eluting only when the column was removed from the electromagnet. At the low field limit (7 mT, Figure 7.3d) almost the entire sample was eluted in the void peak. For the intermediate field values (40 mT, Figure 7.3b, and 20 mT, Figure 7.3c) the sample was divided between the void peak and the no-field fractions, without noticeable fractionation in-between. In comparison, use of the programmed field decay led to quite satisfactory fractionation results. The

programmed field approach in FFF was developed to fractionate broadly polydisperse samples [10], as described in Chapter VI.

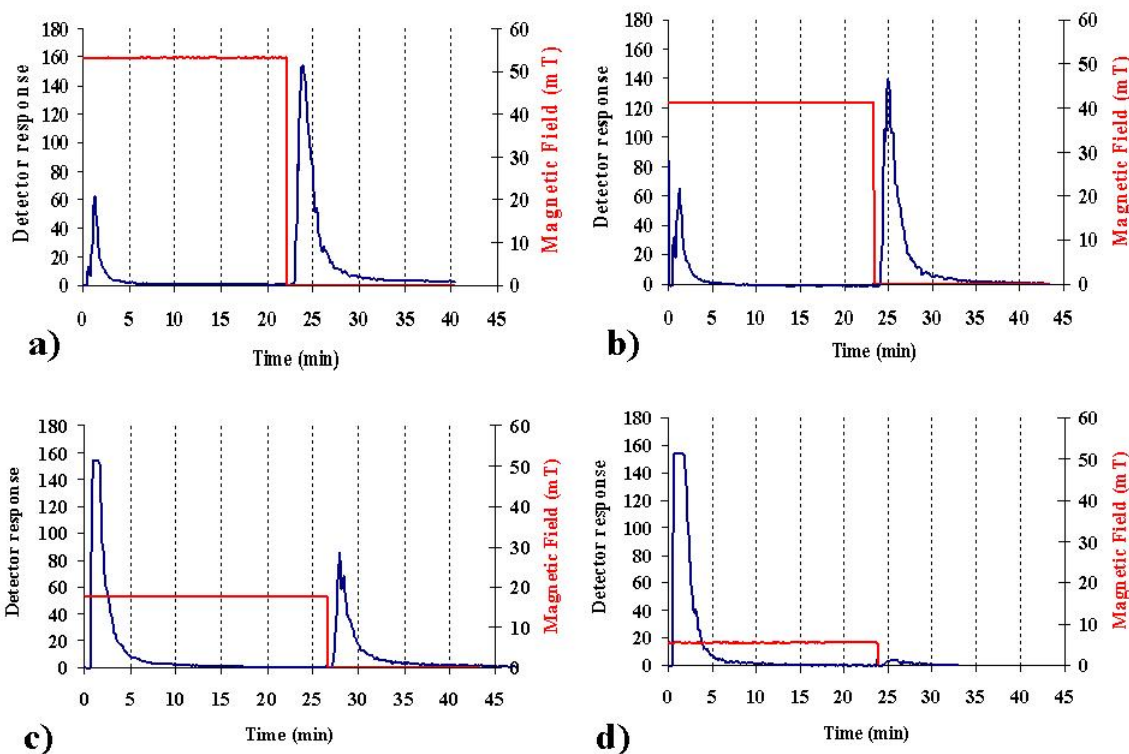


Figure 7.3. MgFFF elution profiles of sample 80 obtained at constant field strengths: a) 53 mT, b) 40 mT, c) 20 mT, d) 7 mT. In each case, the field strength falls to zero when the channel is removed from the magnet.

The first two samples analyzed by applying a field decay program were sample lot 40-43 and lot 80. They were supplied at nominal concentrations of 4.49 mg/ml (lot 40-43) and 4.72 mg/ml (lot 80). Phosphate buffered saline (PBS) at pH of 7.4 was used as the carrier fluid. The samples were diluted with PBS carrier to 1/7 of the supplied concentration. Sample volumes of 20 μ l were introduced to the FFF channel at a sample loading flow rate of 0.10 ml/min for 2 min with an applied magnetic field of 56.5 mT at the accumulation wall, obtained with a total current of 0.25 A. (Magnetic field was

measured at a point adjacent to the channel and a correction applied to obtain the field strength inside the channel, as explained in section 4.2.3.2 and in Figure 4.17.) Stop flow relaxation was allowed to take place for 30 min. (This was to allow the particles to approach their steady state distributions close to the accumulation wall prior to elution.) The samples were eluted at a flow rate of 2.0 ml/min with the field strength held constant at 56.5 mT for 2.0 min, then decaying to 3.3 mT over a period of 7.0 min, after which it was held constant at 3.3 mT. The elution curves for the two samples are shown in Figure 7.4. The field decay program used for the elutions is also included in the figure. This is shown by the dashed curve, which relates to the right hand scale. The two lots of nanoparticles are seen to be quite different. The elution times of the samples are expected to be functions of the magnetic content of the particles and to be independent of the quantity of dextran. It appears that since lot 80 elutes well before lot 40–43, it must contain significantly less magnetite than lot 40–43. The spike on the elution curve for lot 80, just beyond 20 min, indicates the time at which the channel was removed from the quadrupole magnet. The elution of the small amount of material following this shows that a small fraction of the sample does not elute at 3.3 mT, and this could indicate the presence of a small number of particles containing much more magnetite than others or some particle aggregates. The spike on the elution curve for lot 40–43 just beyond 25 min also indicates the point of removal of the channel from the magnet. In this case, very little material is seen to elute after this.

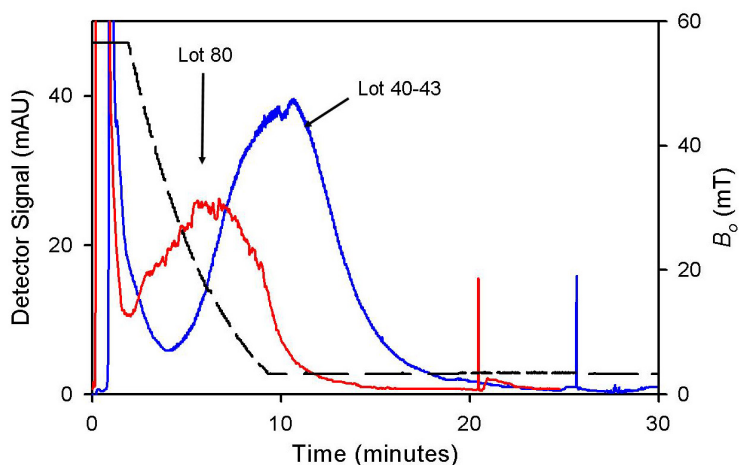


Figure 7.4. Superimposed fractograms (detector response as a function of elution time) obtained for lots 40–43 and 80 of Skold magnetic nanoparticles. Lot 80 is less retained than lot 40–43 and the particles therefore contain less magnetite. The dashed curve shows the programmed field decay at the channel accumulation wall (right hand axis). The field strength is held constant at 56.5 mT for 2 min, and decays to 3.3 mT over a period of 7 min. Fluid flow rate was 2.0 ml/min for both samples.

These results show that MgFFF is capable of distinguishing between two different samples of magnetic nanoparticles. The work described here was preliminary. There was no effort to optimize the flow rate and the field decay program. Subsequently, the other lots of magnetic nanoparticles were analyzed. Their elution was obtained by applying a decay of the field in a wide range of time. Several elution curves for various lots of Skold Technologies nanoparticles are shown in Figure 7.5. All fractograms were obtained under identical conditions of carrier flow rate of 1.0 ml/min, initial field strength of 51 mT at the outer channel wall, held constant for 2 minutes and then decaying to 2.7 mT over a period of 30 minutes. A stop flow time of 30 minutes was used before elution. The elution curves in Figure 7.5 a, obtained more than two weeks apart, demonstrate the reproducibility of the analysis. The narrow pulse toward the end of each fractogram indicates the time when the channel was removed from the magnetic field. The material

elution after this point may have aggregated and/or reversibly adsorbed to the channel wall. The elution curves shown in Figure 7.5b indicate that lots 78 and 80 have very similar magnetic properties. The curves shown in Figure 7.5c suggest that lot 50-56 might have a slightly higher magnetite content than lot 80. The difference in the curves shown in Figure 7.5d give a strong indication that lot 83 has a higher magnetite content than lot 80.

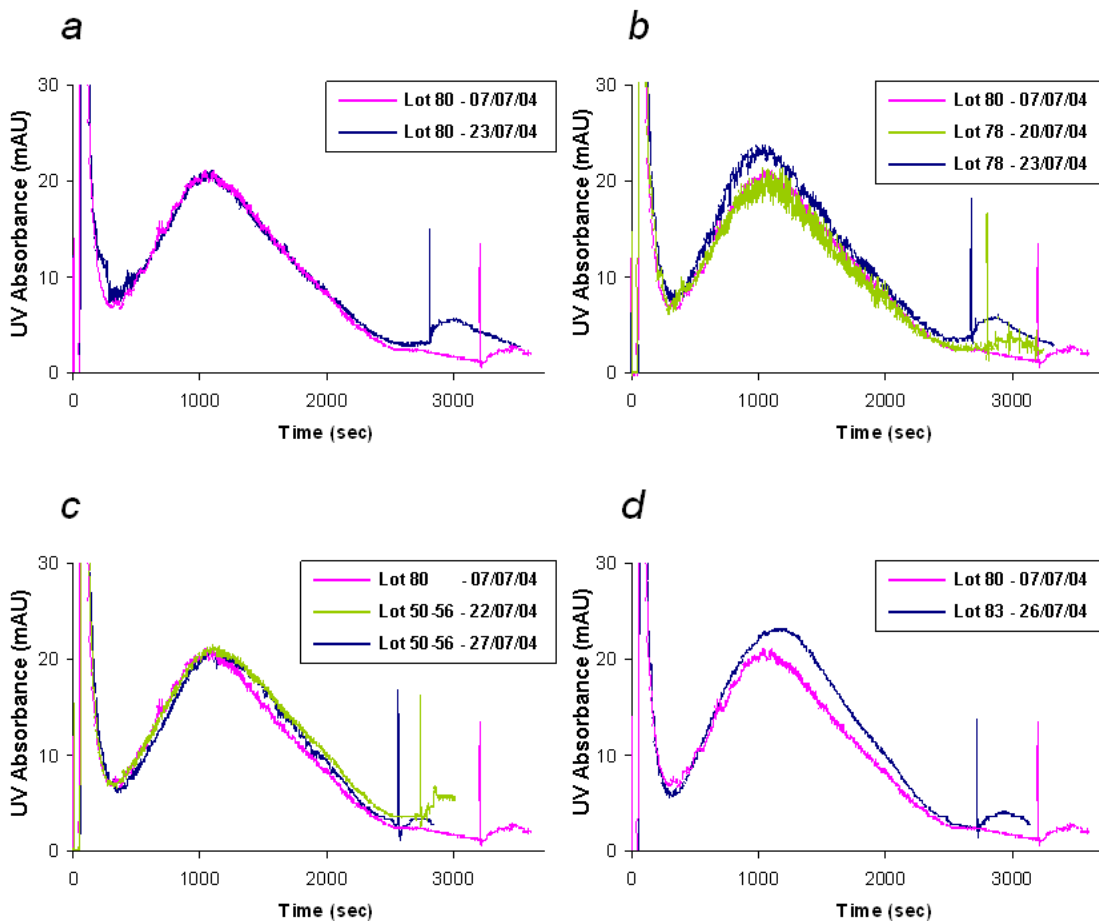


Figure 7.5 MgFFF elution curves for various lots of Skold Technology magnetic nanoparticles obtained under identical conditions. a) two elution curves for lot 80, b) elution curves for lots 80 and 78, c) elution curves for lots 80 and 50-56, d) elution curves for lots 80 and 83.

A typical elution curve for sample lot 80 is shown in Figure 7.6. The elution curve (blue line) shows a sharp void peak at 2 min, followed by the broad peak corresponding to the elution of the particles. The other curve (red line) in the figure shows the field decay as a function of elution time (see the right hand axis). The field at the accumulation wall is held constant for 2 min. It then decays smoothly to 3.7 mT during the sample elution.

Experimental conditions:

Elution flow rate: 0.5 ml/min

Initial magnetic field: 55 mT

Field decay program parameters: $p=12$, $t_1= 8$ min, $t_p= 2$ min, $t_a= -96$ min.

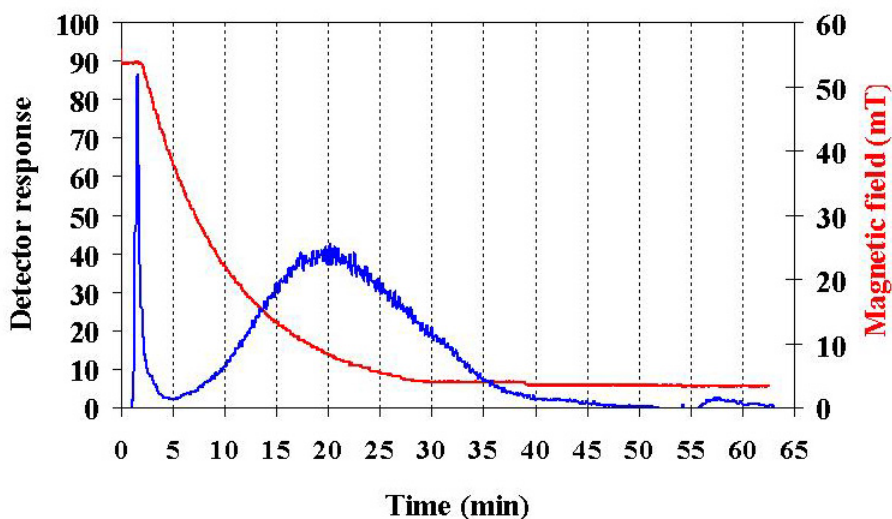


Figure 7.6. Elution profile for sample of Skold nanoparticles (lot 80) and the field decay curve (referring to the right hand axis).

The data reduction procedure requires a magnetization curve for the magnetic nanoparticle core material. Because such curve was unavailable for the particular sample

in hand, a magnetization curve for uncoated magnetite nanoparticles was taken from Ref. [115]. A curve fitting to these data, shown in Figure 7.7, resulted in the following relationship between M and B :

$$M = \frac{9.152 \times 10^6 B}{1 + 27.30B - 0.9229B^2}, \quad (7.1)$$

where M has units of A/m and B units of T.

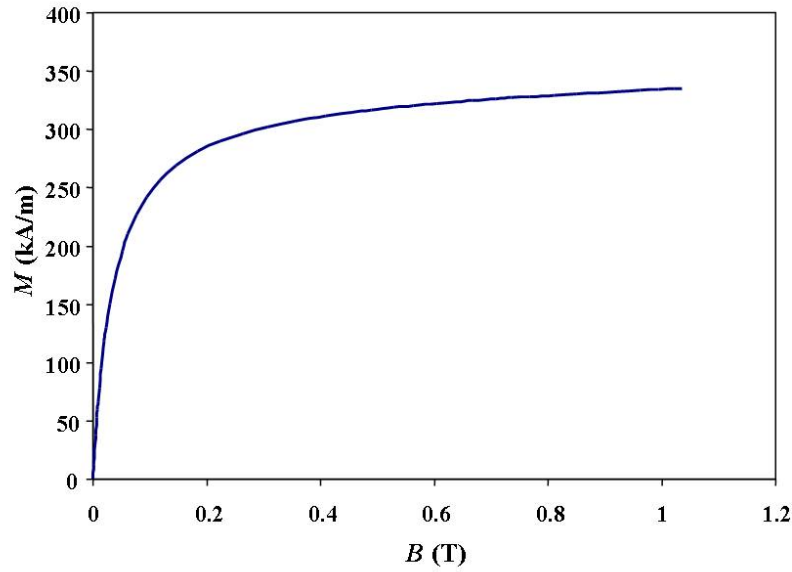


Figure 7.7. Magnetization curve showing the data for superparamagnetic magnetite nanoparticles. The points were digitized from a published plot [115], and fitted to the empirical equation 7.1.

Data reduction requires the determination of the relationship between V_m (and hence core diameter d_m) and the elution time t_r . As mentioned earlier in Chapter VI, numerical solution of equation 6.4 (with successive substitutions for R , λ , and F_m using equations 1.13, 1.8 and 3.5, respectively) yields the required relationship. Note that this takes into account the dependence of F_m on both M (using equation 7.1) and ∇B as field strength B_0 decays. For the purposes of data reduction it was also assumed that there was

no correlation between overall particle size and magnetite core size. This is a reasonable assumption given that there was no evidence to the contrary. Having made this assumption, no light scattering corrections would be required for the detector response. It was therefore assumed that the detector response was directly proportional to particle number concentration in the outlet stream. The result of transformation of the elution curve in Figure 7.6 to a number distribution of equivalent spherical core diameters of magnetite is shown in Figure 7.8. This shows a broad distribution from about 0.1-0.6 μm , with a peak maximum at about 0.2 μm . The calculated core diameters are larger than expected, given that 95% of the particles were determined by QELS to have an overall size between 0.075 μm and 0.39 μm . This may indicate some particle aggregation in the channel due to dipole-dipole interaction or some other physical attraction. The fact that a magnetization curve was assumed for the particles would not account for the extent of the apparent overestimation of the core sizes.

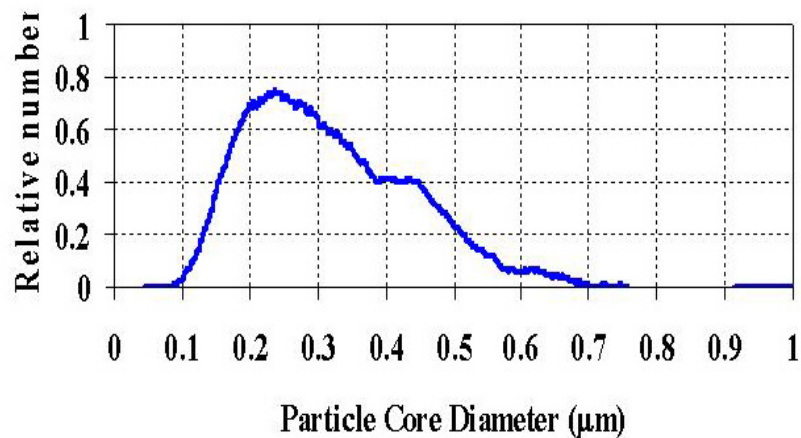


Figure 7.8. Number distribution for calculated equivalent spherical core diameters. A number of different decay programs were evaluated for best sample fractionation.

Figure 7.9a shows elution profiles, of sample 80, obtained under different experimental conditions.

MgFFF experimental parameters:

Red curve:

elution flow rate=1.0 ml/min;

field decay parameters: $p= 4$ min, $t_a= -16$ min, $t_p= 2$ min, $t_l= 4$ min.

Green curve:

elution flow rate=0.5 ml/min;

field decay parameters: $p= 4$ min, $t_a= -16$ min, $t_p= 2$ min, $t_l= 4$ min.

Blue curve:

elution flow rate=0.5 ml/min;

field decay parameters: $p= 12$ min, $t_a= -96$ min, $t_p= 2$ min, $t_l= 8$ min.

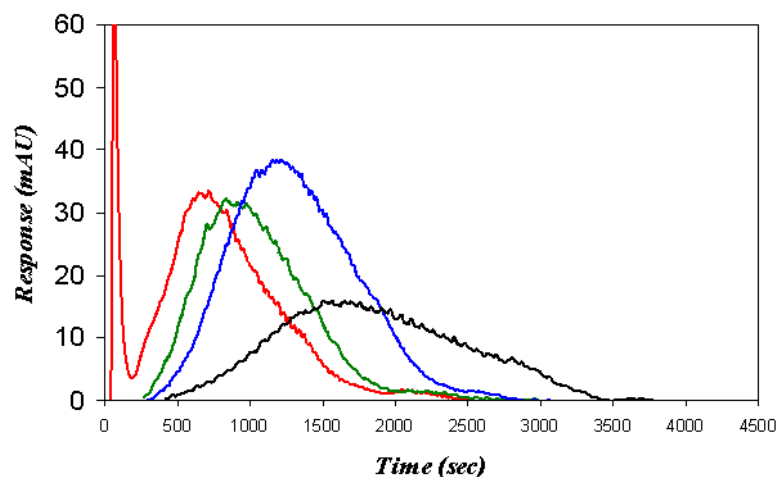
Black curve:

elution flow rate=0.5 ml/min;

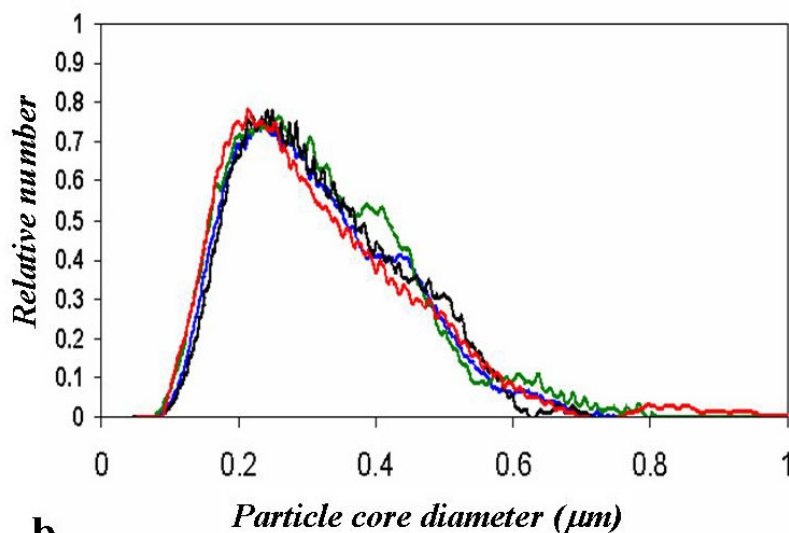
field decay parameters: $p= 8$ min, $t_a= -96$ min, $t_p= 2$ min, $t_l= 12$ min.

Stop flow time and initial field strength were the same for all four analyses.

Once a suitable decay program was selected for the sample, the elution results were reproducible and amenable to quantitative analysis. The calculated, most probable equivalent magnetic mass diameter of the particle lay in the range of 0.20 μm to 0.23 μm , as shown in Figure 7.9b. For data reduction, it is assumed that the sample elutes without any significant particle-wall or particle-particle interaction.



a



b

Figure 7.9. a) Elution profiles of dextran coated magnetite nanoparticles, lot 80, under different experimental conditions. b) Reproducible determination of distribution in particle magnetite content (equivalent spherical diameter of magnetite core) for elution under the different experimental conditions. Note that although the shape of the elution profile depends on the experimental conditions (such as initial field strength, field decay rate, elution flow rate) the calculate size of the magnetic cores is quite consistent. The differences in the region over 0.5 μm are attributable to baseline drift (no corrections were applied).

7.2 MgFFF analysis of maghemite nanoparticles

A sample of dextran-coated maghemite nanoparticles was produced in the laboratory of Professor Shlomo Margel (Department of Chemistry, Bar-Ilan University, Ramat Gan, Israel). The nanoparticles were supplied dispersed in PBS (1 mg/ml Fe concentration). No SEM and DLS measurements were available for this sample. Upon arrival, the sample was stored in the refrigerator. Prior to experiment, the sample was sonicated for about 1 minute. It was then diluted 1:2 with the suspending buffer and sonicated for another minute before its analysis with MgFFF. MgFFF experimental conditions:

Elution flow rate: 0.5 ml/min

Initial magnetic field: 17 mT

Field decay program parameters: $p=12$, $t_1=10$ min, $t_p=4$ min, $t_a=-120$ min.

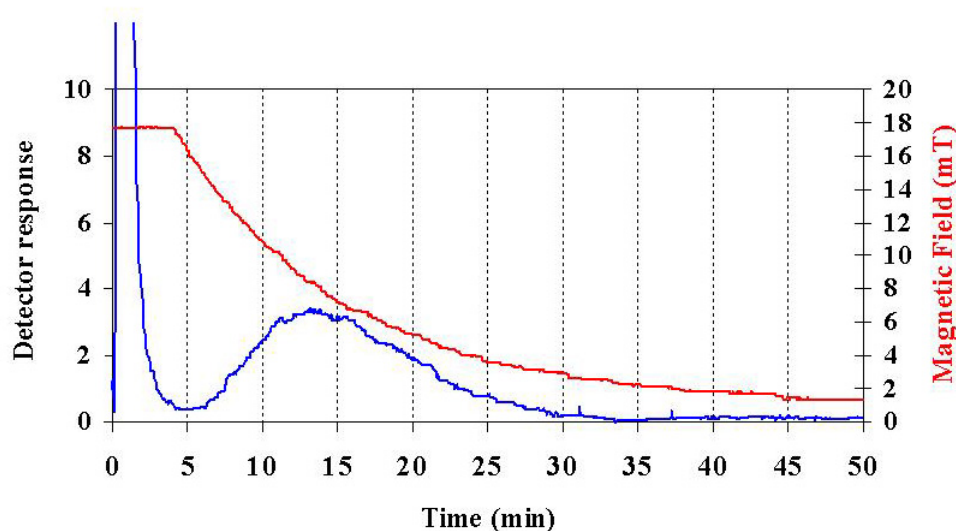


Figure. 7.10. Elution profile for sample of maghemite nanoparticles and the field decay curve (referring to the right hand axis).

The curve in Figure 7.11 represents the calculated distribution in equivalent spherical diameter for the particle maghemite cores. The data reduction is based on an

assumed magnetization curve for maghemite nanoparticles, and the calculated results account for the changing magnetization with the decaying field strength as the particles elute through the system. If particles aggregate by magnetic dipole-dipole interactions or by any other attraction, then the calculated diameters reflect those of the aggregates. The highest frequency of the magnetic core diameter, d_m , is in the range 0.20 μm to 0.30 μm .

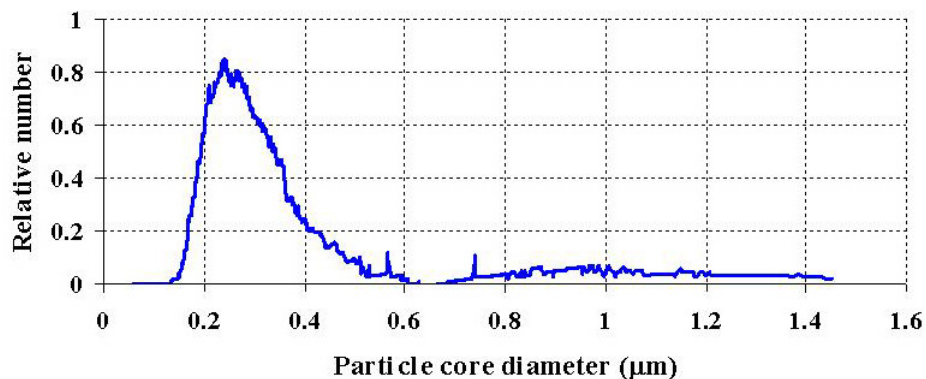


Figure. 7.11. Number distribution for calculated equivalent spherical core diameter of the maghemite nanoparticles.

7.3 MgFFF analysis of CNW nanoparticles

MgFFF analyses were performed on magnetic nanoparticles produced by Columbus NanoWorks, Inc. The sample, labeled CNW, consisted of Fe-hexanoic acid nanoparticles coated with dextran in the suspending buffer of TRIS 50mM+EDTA 0.5mM at pH=8. The particles were diluted to a suitable concentration adding the same buffer and were sonicated 1 minute before each analysis. DLS measurements were performed by Malvern Instruments and shown in Figure 7.12. The DLS results indicate an average diameter of 162 nm.

Results

Z-Average (d.nm): 162
PdI: 0.163
Intercept: 0.982

Diam. (nm)	% Intensity	Width (nm)
194	100.0	76.0

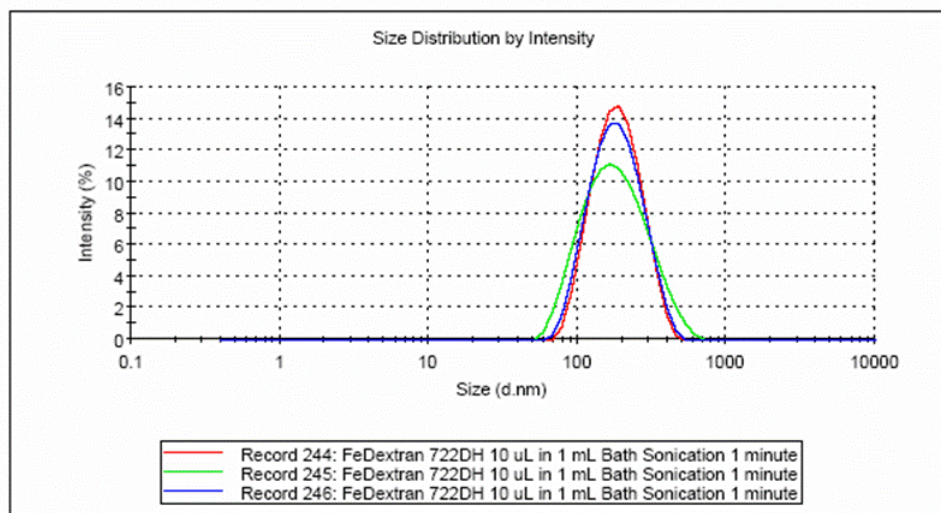


Figure. 7.12. Size distribution data of dextran coated magnetite nanoparticles (provided by CNW) obtained by dynamic light scattering analysis. Measurements carried out by Malvern Instruments.

MgFFF experimental parameters:

Elution flow rate: 0.5 ml/min

Initial magnetic field: 40 mT

Field decay program parameters: $p=12$, $t_1= 10$ min, $t_p= 4$ min, $t_a= -120$ min.

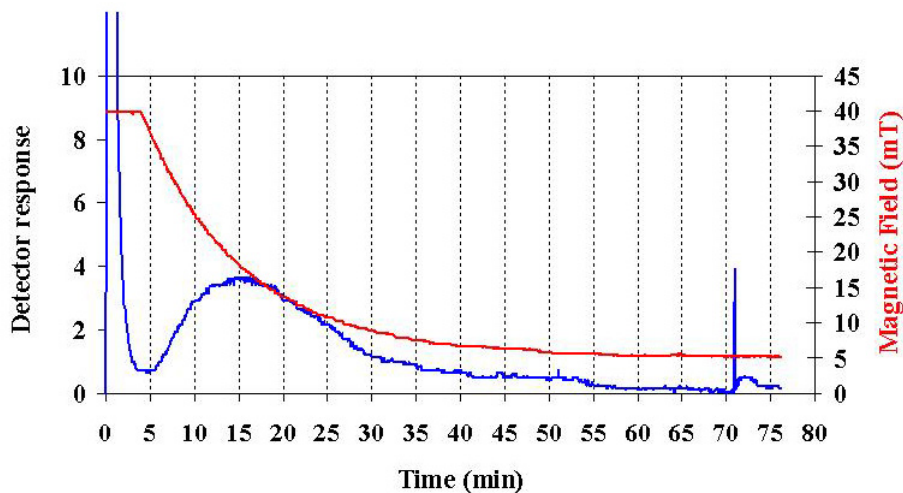


Figure 7.13. Elution profile of sample 628DH_Aq (Fe-hexanoic acid nanoparticles coated with dextran). The magnetic field decay profile is shown by the red line.

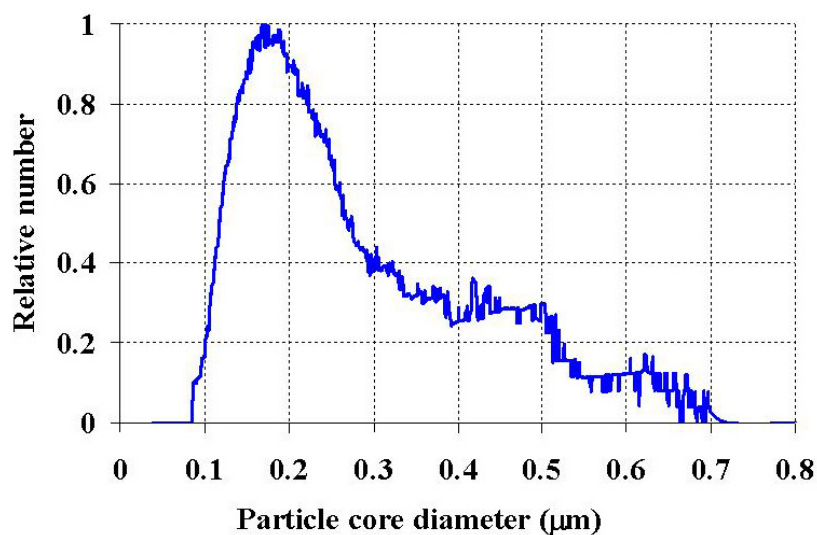


Figure 7.14. Size distribution profile of sample 628DH_Aq (Fe-hexanoic acid nanoparticles coated with dextran).

7.4 Comparison of the three samples

In Figure 7.15 is shown a comparison of the size distribution profiles of the magnetic nanoparticles produced by BD Biosciences, Columbus NanoWorks, and Dr.

Margel. The particles distributions seem to be not much different from one another. These are particles produced mainly for cell labeling and sorting. It seems that the path used for their synthesis leads to the same results in terms of particles size. They evidently work reasonably well for the applications they are used for.

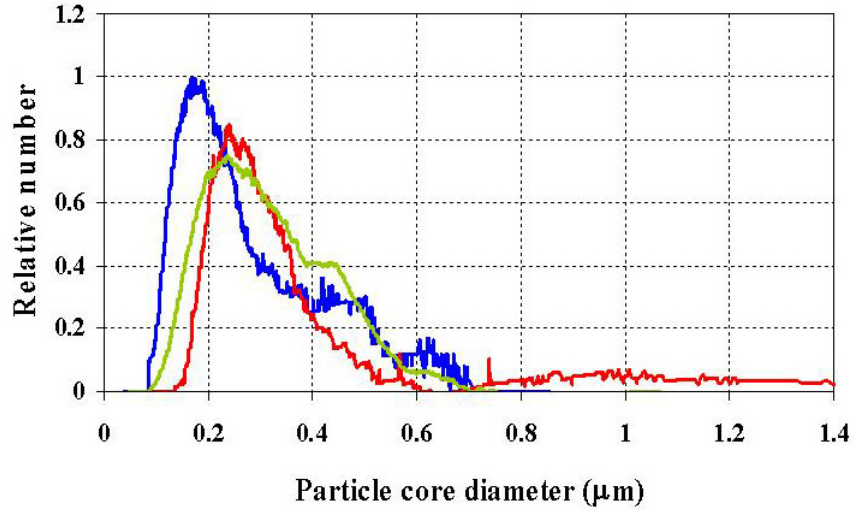


Figure 7.15. Size distribution profiles of sample CNW (Fe-hexanoic acid nanoparticles coated with dextran), blue line; sample MM (dextran coated maghemite nanoparticles), red line; and iron oxide dextran-coated nanoparticles from Skold technologies (BD Biosciences, Pharmingen), green line.

7.5 Importance of the coating in the magnetic nanoparticles

The magnetic dipole-dipole interaction energy for two coated magnetic spheres in contact is described by equation [116]

$$E_{dd} = \frac{\pi \mu_0 M^2 d_m^6}{72 (d_m + 2\delta)^3} \quad (7.2)$$

where μ_0 is the permeability of free space, d_m is the particle core diameter, δ is the thickness of the coating on the cores, and M is the core magnetization.

If we consider 100 nm magnetite cores in 300 nm diameter particles and we assume $M = 50$ kA/m, corresponding to about 6 mT, then:

$$E_{dd} = \frac{\pi}{72} \frac{4\pi \times 10^{-7} (50000)^2 (10^{-7})^6}{(3.0 \times 10^{-7})^3} = 5.1 \times 10^{-21} J \quad (7.3)$$

The thermal energy is equal to

$$kT = 4.1 \times 10^{-21} J \quad (7.4)$$

We would expect aggregation at the initial field strength, but the thermal energy would be sufficient to disrupt the aggregates as the field decays. The critical particle coating is given when the following equation holds:

$$E_{dd} = \frac{\pi}{72} \frac{\mu_0 M^2 d_m^6}{(d_m + 2\delta)^3} = \frac{\pi}{72} \frac{\mu_0 M^2 d_m^6}{d_p^3} = kT \quad (7.5)$$

in which $d_p = d_m + 2\delta$, is the overall particle diameter.

This may be rearranged to the following form

$$\frac{d_p}{d_m} = \left(\frac{\pi \mu_0 M^2}{72 kT} \right)^{1/3} d_m \quad (7.6)$$

The critical ratio of overall particle diameter (d_p) to core diameter (d_m) varies with $M^{2/3}$ and increases linearly with core diameter.

As mentioned earlier in Chapter II, magnetic nanoparticles are often coated with a material that prevents the formation of agglomerates. A sample of uncoated nanoparticles, BD-CCF-9, suspended in MES buffer was also provided by BD Biosciences. The particles were made of bare magnetite and they were analyzed by MgFFF. Prior the analysis the sample was sonicated for about 1 minute and diluted by adding PBS. The elution profile obtained was compared to that obtained for the coated

particles (sample BD-CCF-8); the results are shown in Figure 7.16. The experiments were performed under the same experimental conditions.

Experimental conditions:

Elution flow rate: 0.5 ml/min

Initial magnetic field: 56 mT

Field decay program parameters: $p=8$, $t_1=12$ min, $t_p=2$ min, $t_a=-96$ min.

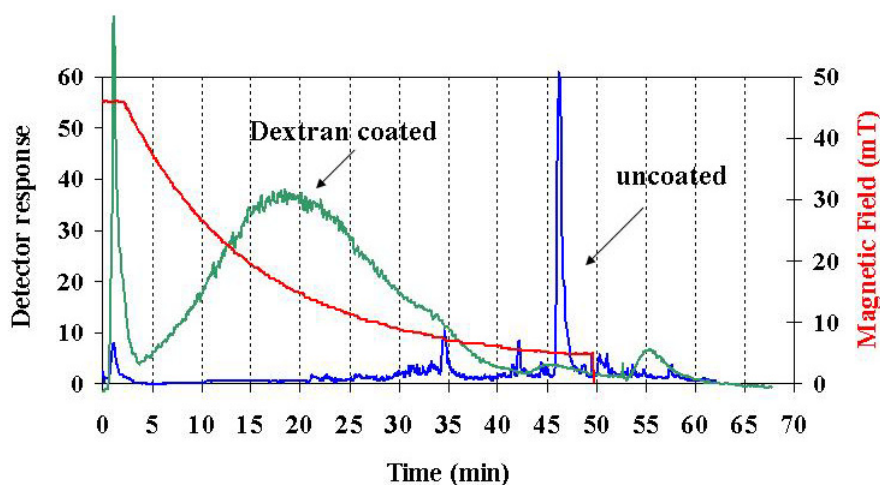


Figure 7.16. Elution profiles for sample BD-CCF-8 (dextran coated magnetic nanoparticles) and sample BD-CCF-9 (bare core material). The experimental conditions (elution flow rate and field decay program) are the same for both analyses. The magnetic field decay profile is shown by the red line.

Note strong retention of the uncoated sample and a narrow distribution of its elution peak, suggesting particle aggregation inside the column, presumably as a result of strong dipole-dipole interactions. The dextran coating prevents particle aggregation by keeping the magnetic material apart and therefore reducing the force of the dipole-dipole interactions. The coated particles elute reproducibly on a smooth, broad peak.

7.6 Conclusions

In conclusion, we have successfully demonstrated a novel approach to magnetic FFF that differs radically from earlier approaches. We have described the advantages that our approach has over earlier attempts. In short, our system possesses all of the qualities required for successful operation: the channel is thin and of uniform thickness across its breadth; the field strength and field gradient are relatively constant throughout the channel; the field is sufficiently strong to retain many of the magnetic nanoparticles of interest; the field strength may be adjusted to suit the magnetic properties of the sample, and may be programmed for the elution of broadly dispersed samples. The MgFFF elution curves are found to be highly reproducible, and MgFFF has been shown to be capable of distinguishing between different lots of magnetic nanoparticles from the same source, as shown in Figure 7.5.

REFERENCES

1. Giddings, J.C., *A new separation concept based on a coupling of concentration and flow nonuniformities*. Separation Science, 1966. **1**(1): p. 123-125.
2. Giddings, J.C., *The field-flow fractionation family: Underlying principles*, in *Field-Flow Fractionation Handbook*, M.E. Schimpf, K. Caldwell, and J.C. Giddings, Editors. 2000, John Wiley & Sons: New York, NY. p. 3-30.
3. *Applications: Industrial, Biomedical and Environmental*, in *Field-Flow Fractionation Handbook*, M.E. Schimpf, K. Caldwell, and J.C. Giddings, Editors. 2000, John Wiley & Sons: New York, NY. p. 345-558.
4. Giddings, J.C., *Unified Separation Science* (Wiley, New York), 1991.
5. Giddings, J.C., *Continuous particle separation in split-flow thin (SPLITT) cells using hydrodynamic lift forces*. Separation Science and Technology, 1988. **23**(1-3): p. 119-131.
6. Oersted, H.C., *Experiment on the effects of a current on the magnetic field needle*. Annals of Philosophy, 1819. **16**.
7. Curie, P., Ann. Chim. Phys., 1895. **5**(7): p. 289-405.
8. Néel, L., Ann. Physique, 1948. **3**(12): p. 137.
9. Weiss, P., J. of Physics, 1907. **6**: p. 661-690.
10. Landau, I.D., and Lifschitz, E. M., Physik Z. Sowjetunion, 1935. **8**: p. 153.
11. Moghimi, S.M., et al., *Long-circulating and target-specific nanoparticles: theory to practice*. Pharma. Rev., 2001. **53**: p. 283-318.
12. Panyam, J., et al., *Biodegradable nanoparticles for drug and gene delivery to cells and tissue*. Adv. Drug. Del. Rev., 2003. **55**: p. 329-47.
13. Shinkai, M., *Functional magnetic particles for medical application*. J. of Bioscience and Bioengineering, 2002. **94**(6): p. 603-613.
14. Chatterjee, J., et al., *Size dependent magnetic properties of iron-oxide nanoparticles*. J. Magn. Magn. Mater., 2003. **257**(1): p. 113-8.
15. Bean, C.P., et al., *Superparamagnetism*. J. Appl. Phys., 1959. **30**: p. 120S-9S.
16. Tartaj, P., et al., *The preparation of magnetic nanoparticles for applications in biomedicine*. J. Phys. D: Appl. Phys., 2003(36): p. R182-97.
17. Wormuth, K.e.a., J. Colloid Interface Sci., 2001. **241**: p. 366.
18. Schwertmann, U., Cornell, R. M., *Iron oxides in the laboratory: preparation and characterization*. Weinheim, Cambridge:VCH, 1991.
19. Cornelis, K., Hurlburt C. S., *Manual of Mineralogy*. New York: Wiley, 1977.
20. Wang, Y.X., et al., *Superparamagnetic iron oxide contrast agents: physicochemical characteristics and applications in MR imaging*. Eur. Radiol., 2001. **11**: p. 2319-31.
21. Hamley, I.W., *Nanotechnology with soft materials*. Angew Chem. Int. Ed., 2003. **42**: p. 1692-712.
22. Mendenhall, G.D., et al., *Optimization of long-term stability of magnetic fluids from magnetite and synthetic polyelectrolytes*. J. Colloid Interface Sci., 1996. **184**(2): p. 519-26.

23. Dresco, P.A., et al., *Preparation and properties of magnetite and polymer magnetite nanoparticles*. Langmuir, 1999. **15**: p. 1945.
24. Vladimir, S., et al., *Physical and chemical properties of magnetite and magnetite-polymer nanoparticles and their colloidal dispersions*. J. Colloid Interface Sci., 1999. **212**: p. 49.
25. Chantrell, R.W., et al., *Dilution induced instability in ferrofluids*. J. Appl. Phys., 1982. **53**(11): p. 8341-8343.
26. Bonder, M.J., et al., *Magnetic nanoparticles*, in *Advanced Magnetic Nanostructures*, a.S.R. Sellymer D., Editor. 2006, Springer US: Boston, MA. p. 183.
27. Frenkel, J.a.D., J., Nature, 1930. **126**: p. 274.
28. Elliott, S.R., *The physics and chemistry of solids*. 1998, New York: Wiley.
29. Vassiliou, J.K., et al., *Magnetic and optical properties of γ -Fe₂O₃ nanocrystals*. J. Appl. Phys., 1993. **73**(10): p. 5109-5116.
30. Néel, L., Compt. Rend. Acad. Sci., 1949. **228**: p. 664.
31. Néel, L., Annal. Geophys., 1949. **5**: p. 99.
32. Néel, L., Adv. Phys., 1955. **4**: p. 191.
33. Brown, J., W. F., J. Appl. Phys., 1963. **30**: p. 130.
34. Brown, J., W. F., in *Fluctuation phenomena in solids*. 1964, Academic: New York. p. 37.
35. Malkin, L.M., et al, Appl. Phys. Lett., 1999. **75**: p. 844.
36. Nielsen, O.S., et al., *A future for hyperthermia in cancer treatment?* Eur. J. Cancer, 2001. **37**: p. 1587-9.
37. Gordon, R.T., et al., *Intracellular hyperthermia. A biophysical approach to cancer treatment via intracellular temperature and biphysical alterations*. Med. Hypothesis, 1979. **5**: p. 83-102.
38. Yeh, T.C., et al., *Intracellular labeling of T-cells with superparamagnetic contrast agents*. Magn. Reson. Med. , 1993. **30**: p. 617-25.
39. Handgretinger, R., et al., *Isolation and transplantation of autologous peripheral CD34+ progenitor cells highly purified by magnetic-activated cell sorting*. Bone Marrow Transplant, 1998. **21**: p. 987-93.
40. Schoepf, U., et al., *Intracellular magnetic labelling of lymphocytes for in vivo trafficking studies*. BioTechniques, 1998. **24**: p. 642-51.
41. Guesdon, J.L., et al., *Magnetic enzyme immunoassay for measuring human IgE*. J. Allergy Clin. Immunol., 1978. **6**: p. 23-27.
42. Druet, E., et al., *Magnetic solid-phase enzyme immunoassay for the detection of anti-glomerular basement membrane antibodies*. J. Immunol. Methods, 1982. **48**: p. 149-157.
43. Tartaj, P., et al., *Advances in magnetic nanoparticles for biotechnology applications*. J. Magn. Magn. Mater., 2005. **290-291**: p. 28-34.
44. Wust, P., et al., Lancet Oncol., 2002. **3**: p. 487.
45. Jordan, A., et al., J. Magn. Magn. Mater., 1999. **201**: p. 413.
46. Chan, D.C.F., et al., J. Magn. Magn. Mater., 1993. **122**: p. 374.
47. Rosensweig, R.E., J. Magn. Magn. Mater., 2002. **252**: p. 370.
48. Freeman, M.W., et al., J. Appl. Phys., 1960. **31**: p. 404.
49. Coroiu, I., J. Magn. Magn. Mater., 1999. **201**: p. 449.

50. Kim, D.K., et al., *J. Magn. Magn. Mater.*, 2001. **225**: p. 256.
51. Jordan, A., et al., *J. Magn. Magn. Mater.*, 2001. **225**: p. 118.
52. Bradbury, A., et al., *IEEE Trans. Mag.*, 1984. **20**(5): p. 1846-8.
53. Foner, S., *Rev. Sci. Inst.*, 1959. **30**: p. 548.
54. Webb, W., *IEEE Trans. Mag.*, 1972. **8**: p. 66.
55. Mykhaylyk, O.M., et al., *Use of ESR, Mössbauer spectroscopy, and SQUID-magnetometry for the characterization of magnetic nanoparticles on the base of metal iron and its implications in vivo.*, in *Scientific and Clinical Applications of Magnetic Carriers*, U. Häfeli, et al, Editor. 1997, Plenum Press: New York. p. 177-204.
56. Johnson, C.E., *Characterization of magnetic material by Mössbauer spectroscopy*. *J. Phys. D: Appl. Phys.*, 1996. **29**: p. 2266-2273.
57. Da Silva, M.F., et al., *Phys. Revs. E.*, 1993. **48**: p. 4483-4491.
58. Carpino, F., et al., *Analysis of magnetic nanoparticles using quadrupole magnetic field-flow fractionation*. *Journal of Magnetism and Magnetic Materials*, 2005. **293**(1): p. 546-552
59. Giddings, J.C., P.S. Williams, and R. Beckett, *Fractionating power in programmed field-flow fractionation: Exponential sedimentation field decay*. *Analytical Chemistry*, 1987. **59**(1): p. 28-37.
60. Giddings, J.C., et al., *Fast particle separation by flow/steric field-flow fractionation*. *Analytical Chemistry*, 1987. **59**(15): p. 1957-1962.
61. Williams, P.S., M.C. Giddings, and J.C. Giddings, *A data analysis algorithm for programmed field-flow fractionation*. *Analytical Chemistry*, 2001. **73**(17): p. 4202-4211.
62. McCloskey, K.E., J.J. Chalmers, and M. Zborowski, *Magnetophoretic mobilities correlate to antibody binding capacities*. *Cytometry*, 2000. **40**(4): p. 307-315.
63. Nakamura, M., et al., *Theoretical and experimental analysis of the accuracy and reproducibility of cell tracking velocimetry*. *Experiments in Fluids*, 2001. **30**(4): p. 371-380.
64. Chalmers, J.J., et al., *An instrument to determine the magnetophoretic mobility of labeled, biological cells and paramagnetic particles*. *Journal of Magnetism and Magnetic Materials*, 1999. **194**(1-3): p. 231-241.
65. Vickrey, T.M. and J.A. Garcia-Ramirez, *Magnetic field-flow fractionation: theoretical basis*. *Separation Science and Technology*, 1980. **15**(6): p. 1297-1304.
66. Schunk, T.C., J. Gorse, and M.F. Burke, *Parameters affecting magnetic field-flow fractionation of metal oxide particles*. *Separation Science and Technology*, 1984. **19**(10): p. 653-666.
67. Gorse, J., T.C. Schunk, and M.F. Burke, *The study of liquid suspensions of iron oxide particles with a magnetic field-flow fractionation device*. *Separation Science and Technology*, 1984-85. **19**(13-15): p. 1073-1085.
68. Semenov, S.N. and A.A. Kuznetsov, *Flow fractionation in a transverse high-gradient magnetic field*. *Russian Journal of Physical Chemistry*, 1986. **60**(2): p. 247-250.
69. Semenov, S.N., *Flow fractionation in a strong transverse magnetic field*. *Russian Journal of Physical Chemistry*, 1986. **60**(5): p. 729-731.

70. Mori, S., *Magnetic field-flow fractionation using capillary tubing*. Chromatographia, 1986. **21**(11): p. 642-644.
71. Ohara, T., et al., *FFF using high gradient and high intensity magnetic field: process analysis*, in *Fourth International Symposium on Field-Flow Fractionation (FFF94)*. 1994: Lund, Sweden.
72. Tsukamoto, O., et al., *Feasibility study on separation of several tens nanometer scale particles by magnetic field-flow-fractionation technique using superconducting magnet*. IEEE Transactions on Applied Superconductivity, 1995. **5**(2 Part 1): p. 311-314.
73. Ohara, T., et al., *Feasibility of using magnetic chromatography for ultra-fine particle separation*. Proceedings of the IEE Japan-Power & Energy '95, 1995: p. 161-166.
74. Ohara, T., et al., *Feasibility of magnetic chromatography for ultra-fine particle separation*. Transactions of the IEE Japan, 1996. **116-B**(8): p. 979-986.
75. Wang, X., et al., *Computer simulation of magnetic chromatography system for ultra-fine particle separation*. Transactions of the IEE Japan, 1997. **117-B**(11): p. 1466-1474.
76. Ohara, T., *Feasibility of using magnetic chromatography for ultra-fine particle separation*, in *High Magnetic Fields: Applications, Generations, Materials*, H.J. Schneider-Muntau, Editor. 1997, World Scientific: New Jersey. p. 43-55.
77. Ohara, T., et al., *Magnetic chromatography: Numerical analysis in the case of particle size distribution*. Transactions of the IEE Japan, 2000. **120-A**(1): p. 62-67.
78. Karki, K.C., et al., *A numerical model for magnetic chromatography*. Applied Mathematical Modelling, 2001. **25**(5): p. 355-373.
79. Mitsuhashi, K., et al., *Retention of ions in a magnetic chromatograph using high-intensity and high-gradient magnetic fields*. Separation Science and Technology, 2002. **37**(16): p. 3635-3645.
80. Nomizu, T., et al., *Magnetic chromatography of magnetic fine particles suspended in a liquid with a steel-bead column under a periodically intermittent magnetic field*. Analytical Sciences, 1996. **12**(6): p. 829-834.
81. Giddings, J.C., *Cyclical field field-flow fractionation: A new method based on transport rates*. Analytical Chemistry, 1986. **58**(9): p. 2052-2056.
82. Lee, S., et al., *Particle separation and characterization by sedimentation/cyclical-field field-flow fractionation*. Analytical Chemistry, 1988. **60**(11): p. 1129-1135.
83. Nomizu, T., K.-i. Yamamoto, and M. Watanabe, *Magnetic chromatography for magnetic fine particles using a periodically intermittent magnetic field*. Analytical Sciences, 2001. **17**(Supplement): p. i177-i180.
84. Zborowski, M., et al., *Continuous cell separation using novel magnetic quadrupole flow sorter*. Journal of Magnetism and Magnetic Materials, 1999. **194**: p. 224-230.
85. Wahlund, K.-G. and J.C. Giddings, *Properties of an asymmetrical flow field-flow fractionation channel having one permeable wall*. Analytical Chemistry, 1987. **59**(9): p. 1332-1339.
86. Margel, S., et al., *Synthesis, characterization, and use of new solid and hollow, magnetic and non-magnetic, organic-inorganic monodispersed hybrid*

- microspheres*, in *Scientific and Clinical Applications of Magnetic Carriers*, U. Häfeli, et al., Editors. 1997, Plenum Press: New York, NY. p. 37-52.
87. Williams, P.S., T. Koch, and J.C. Giddings, *Characterization of near-wall hydrodynamic lift forces using sedimentation field-flow fractionation*. Chemical Engineering Communications, 1992. **111**: p. 121-147.
 88. Ho, B.P. and L.G. Leal, *Inertial migration of rigid spheres in two-dimensional unidirectional flows*. Journal of Fluid Mechanics, 1974. **65**: p. 365-400.
 89. Vasseur, P. and R.G. Cox, *The lateral migration of a spherical particle in two-dimensional shear flows*. Journal of Fluid Mechanics, 1976. **78**(2): p. 385-413.
 90. Segré, G. and A. Silberberg, *Behaviour of macroscopic rigid spheres in Poiseuille flow. Part 2. Experimental results and interpretation*. Journal of Fluid Mechanics, 1962. **14**: p. 136-157.
 91. Williams, P.S., S. Lee, and J.C. Giddings, *Characterization of hydrodynamic lift forces by field-flow fractionation. Inertial and near-wall lift forces*. Chemical Engineering Communications, 1994. **130**: p. 143-166.
 92. Williams, P.S., et al., *Effect of viscosity on retention time and hydrodynamic lift forces in sedimentation/steric field-flow fractionation*. Chemical Engineering Science, 1996. **51**(19): p. 4477-4488.
 93. Cox, R.G. and H. Brenner, *The lateral migration of solid particles in Poiseuille flow — I. Theory*. Chemical Engineering Science, 1968. **23**(2): p. 147-173.
 94. Bernard, A., et al., *Red blood cell separations by gravitational field-flow fractionation: instrumentation and applications*. Trends in Analytical Chemistry, 1995. **14**(6): p. 266-273.
 95. Cardot, P.J.P., J.-M. Launay, and M. Martin, *Age-dependent elution of human red blood cells in gravitational field-flow fractionation*. Journal of Liquid Chromatography & Related Technologies, 1997. **20**(16-17): p. 2543-2553.
 96. Coryell, C.D., F. Stitt, and L. Pauling, *The magnetic properties and structure of ferrihemoglobin (methemoglobin) and some of its compounds*. Journal of the American Chemical Society, 1937. **59**(4): p. 633-642.
 97. Pauling, L. and C.D. Coryell, *The magnetic properties and structure of hemoglobin, oxyhemoglobin and carbonmonoxyhemoglobin*. Proceedings of the National Academy of Sciences, 1936. **22**(4): p. 210-216.
 98. Zborowski, M., et al., *Red Blood Cell Magnetophoresis*. Biophys. J., 2003. **84**: p. 2368-2645.
 99. Giddings, J.C., L.K. Smith, and M.N. Myers, *Programmed thermal field-flow fractionation*. Analytical Chemistry, 1976. **48**(11): p. 1587-1592.
 100. Yang, F.J.F., M.N. Myers, and J.C. Giddings, *Programmed sedimentation field-flow fractionation*. Analytical Chemistry, 1974. **46**(13): p. 1924-1930.
 101. Yang, F.J., M.N. Myers, and J.C. Giddings, *High resolution particle separations by sedimentation field-flow fractionation*. Journal of Colloid and Interface Science, 1977. **60**(3): p. 574-577.
 102. Williams, P.S., J.C. Giddings, and R. Beckett, *Fractionating power in sedimentation field-flow fractionation with linear and parabolic field decay programming*. Journal of Liquid Chromatography, 1987. **10**(8&9): p. 1961-1998.

103. Kirkland, J.J. and W.W. Yau, *Thermal field-flow fractionation of polymers with exponential temperature programming*. *Macromolecules*, 1985. **18**(11): p. 2305-2311.
104. Williams, P.S., et al., *Comparison of experimental and theoretical fractionating power for exponential field decay sedimentation field-flow fractionation*. *The Analyst*, 1988. **113**(8): p. 1253-1259.
105. Williams, P.S. and J.C. Giddings, *Power programmed field-flow fractionation: A new program form for improved uniformity of fractionating power*. *Analytical Chemistry*, 1987. **59**(17): p. 2038-2044.
106. Williams, P.S. and J.C. Giddings, *Comparison of power and exponential field programming in field-flow fractionation*. *Journal of Chromatography*, 1991. **550**: p. 787-797.
107. Williams, P.S. and J.C. Giddings, *Theory of field-programmed field-flow fractionation with corrections for steric effects*. *Analytical Chemistry*, 1994. **66**(23): p. 4215-4228.
108. Yau, W.W., et al., *Sep. Sci. Technol.*, 1981. **16**: p. 577-605.
109. Kirkland, J.J., et al., *Anal. Chem.*, 1981. **53**: p. 1730-1736.
110. Giddings, J.C., et al., *Anal. Chem.*, 1987. **59**: p. 28-37.
111. Yang, F.-S., K.D. Caldwell, and J.C. Giddings, *Colloid characterization by sedimentation field-flow fractionation. II. Particle size distribution*. *Journal of Colloid and Interface Science*, 1983. **92**(1): p. 81-91.
112. Williams, P.S., et al., *A Data Analysis Algorithm for Programmed Field-Flow Fractionation*. *Anal. Chem.*, 2001. **73**(17): p. 4202-4211.
113. Moon, M.H. and J.C. Giddings, *Extension of sedimentation/steric field-flow fractionation into submicron range: Size analysis of 0.2-15 μm metal particles*. *Analytical Chemistry*, 1992. **64**(23): p. 3029-3037.
114. Skold, C.N., *Magnetic particles and methods of producing coated magnetic particles*. US Patent 7169618, (2007).
115. Yamaura, M., et al., *Preparation and characterization of (3-aminopropyl) triethoxysilane-coated magnetite nanoparticles*. *Journal of Magnetism and Magnetic Materials*, 2004. **279**(2-3): p. 210-217.
116. Rosensweig, R.E., in *Ferrohydrodynamics*. 1997, Dover Publications, Inc.: Mineola, NY.